DRA

PLANETARY SCIENCE INSTITUTE

QUARTERLY PROGRESS REPORT

PLANETARY RADAR STUDIES

NASW 3383

SAI 1-142-08-078-00

15 August 1981

T.W. Thompson (Principal Investigator)

J.A. Cutts (Co-Investigator)

Planetary Science Institute
Science Applications, Inc.
283 South Lake Avenue, Suite 218
Pasadena, California 91101
(213)449-4955

INDEX

INTRODUCTION

A proposal entitled "Planetary Radar Studies: Venus Crater Signatures and 70cm Radar Maps of the Moon" was submitted to NASA's Lunar and Planetary Program on 13 August 1980. That proposed research was funded for one year starting in May 1981 and this is the first Quarterly Progress Report on the effort.

This work has the following tasks:

Task I: Crater Studies

1. Obtain refined determination of the IR/radar signatures of crater floors (from existing data and correlate these with photogeologic characteristics including crater age. Refinements over previous work shall include (a) signal processing to permit better estimates of IR/radar signatures of smaller craters to be obtained and (b) use of an improved catalog of relative ages of lunar craters that has finer age resolution than the one previously employed.

2. Investigate how the bright IR/radar haloes surrounding many lunar craters vary with age.

3. Compare radar characteristics of lunar and suspected Venusian craters to cast light on possible contrasting styles of crater formation and surface degradation processes on the two bodies.

Task II: High Resolution Radar Mapping of the Moon

1. Complete limb-to-limb calibration using the beam swing technique.

2. Obtain six high resolution 70cm radar maps of an area from 10° to 40° from the sub-radar point (the so-called inner ring) of the Moon with radar cell sizes of 2 to 4km.

This work is a continuation of NASA Contract NASW 3383, Planetary Radar Studies, which was conducted from May 1980 through April 1981. The basis for this work was provided by other, previous NASA contracts. In particular, NASW 3117 (Lunar Megaregolith Properties from Remote Sensing Data) provided us with a catalog of 1310 infrared and radar lunar craters. Also, NASW 3205 (Lunar Radar Backscatter Studies) supported Arecibo radar observations in December 1978, which provided an invaluable data base for computer software development for our current work.

With this history of these past efforts, we now describe the progress on the two tasks mentioned above. Sections I and II describe Tasks I and II respectively, while all work is summarized in Section III. Figures and Tables follow Section III.

TASK I: CRATER STUDIES

Progress on this task has proceeded in two study areas. The study of the evolution of Venusian craters was the subject of a manuscript (see Appendix A) which has been accepted and revised for publication in Icarus. A second paper on lunar craters with radar bright ejecta was also accepted for publication (Appendix B) in Icarus. This complements a paper on the evolution of the infrared and radar signatures of lunar crater interiors recently published in the Proceedings of the Lunar Highland Crust Conference.

One important aspect of our work is understanding how the radar signatures of craters evolve with geologic time. The evolution of the radar signatures of Venus craters may have analogies to those of lunar craters. The evolution of lunar craters appears to be driven in large part by meteoridic bombardment, which gardens the lunar surface and destroys the rocks which create enhanced radar backscatter. This evolution is size dependent as smaller craters lose their signatures faster than larger craters. This is illustrated in the lunar case where size-frequency distributions of radar-bright craters and visual craters are compared. The distributions of radar-bright craters deviate from production distributions derived from surface photography.

Venus crater populations also deviate from a production distribution, based upon Arecibo earth-based radar data published by Don Campbell and Barbara Burns of Cornell. Gardening by meteoroids is not relevant to the Venus case because of the thick Venus atmosphere. An alternate crater erasure process on Venus may be deposition of a thin mantle of dust which obliterates the surface roughness and rocky deposits responsible for the bright radar signature. A possible source of these dust layers may be the insertion of fine grained debris into the atmosphere by large impact equivalent to those which formed the larger craters on the Moon. To study this, we simulated Venus impacts with a Monte Carlo computer model where the impactors would have a lunar production curve if no atmosphere existed. In addition, we assumed that each impact would inject a small percentage of the ejecta into the atmosphere and subsequently deposit this, a fine-particle layer. A model can be devised to match the observed bright radar crater populations of Venus as described further in Appendix A.

The study of Venus cratering can be accomplished via the interpretation of lunar craters, where the radar signatures are complemented by a host of observables at other wavelengths and a well understood body of photogeological interpretation. Since the interpretation of the lunar radar signatures has a number of elements common with the eventual interpretation of the VOIR images from Venus, the continued refinement of the lunar radar interpretation is needed. We have made progress here.

Recent study of the radar signatures of lunar craters has taken two somewhat different paths -- crater interiors and crater exteriors. The recent study of crater interiors was just published as an article in The Proceedings of the Lunar Highlands Crust Conference. We also conducted a study of crater ejecta with strong 3.8cm radar enhancements. This, as mentioned above, will soon be published in Icarus (see Appendix B).

Continued study of the radar signatures of lunar craters will be enhanced by our computer cataloging effort. In particular, the two catalogs described in Appendix C have been installed on the disk data sets of SAI's DEC-10 computer in La Jolla, California. That computer is accessible via a 1200 baud data link in our Pasadena office.

In summary, we have made progress in study of both Venusian and lunar craters via their radar signatures. These have resulted in the scientific paper given in the Appendices A and B. Much of the scientific data for these papers resides as two infrared/radar catalogs described in detail in Appendix C.

TASK II: HIGH RESOLUTION RADAR MAPPING OF THE MOON

The long range goal of this task is to produce new 70cm radar maps of the Moon with substantial improvement in resolution and radarmetric control over the existing 70cm radar data, obtained originally in the late 1960's. This is a multi-year effort, where the current funding will emphasize a computer processing of five radar observations of the Moon obtained at the Arecibo Observatory, Arecibo, Puerto Rico in May 1981.

Figure 1 provides an overview of the radar system used in May 1981. Radar pulses were transmitted from the main antenna; echoes were received at both the main antenna and a smaller auxiliary antenna located some 11km northeast of the main antenna. Polarized echoes can be received at both antennas while depolarized echoes can be received only at the auxiliary antenna. If both polarized and depolarized echoes are received at the auxiliary antenna, we obtain a good estimate of the ratio of depolarized to polarized echoes. If one receives polarized echoes on the main antenna, one obtains stronger echoes and the best rejection of radar features in the conjugate reflecting areas. Polarized data in our observations was obtained both ways with roughly equal observation times. One of the data processing goals during the summer of 1981 is to establish whether future observations will emphasize the acquisition of polarized data via the main antenna, via the auxiliary antenna or via both antennas.

The observations in May 1981 were very successful. The Arecibo antenna was scheduled for two test runs followed by six consecutive days for routine observations. No useful data was obtained during the test runs. The 430 Mhz transmitter was down for the first test run; very poor data was obtained on the second test run because of an ephemeris program error. Fortunately, very good data was obtained on the six consecutive days of routine observations.

Figure 2 and Table 1 provide an overview of the data acquired during the six consecutive observations from 06 May 1981 through 11 May 1981. We have good data for two inner areas (Montes Apenninus and Ptolemeaus) and three outer areas (Plato, Tyco and the South Pole). Six inner areas and 12 outer areas are needed to map all of the earth-side hemisphere. Our original goal was to observe the six inner areas. This was not possible since the tilt between the true and apparent (Doppler) equator was not great

enough for the days when we were scheduled on the telescope. (The radar mapping geometry for our May observations is given in Figures 3 through 14.) Instead, we devoted some days to the limb areas. The two observations of the inner areas were done with 10 μsec coded pulses while the limb areas were done with 12 and 15 μsec uncoded pulses. In all of these, we have resolutions on the order of 2-4 kilometers. It is important that we have a range of observation conditions that will help us design future observations.

A number of data processing steps will convert the raw radar samples into a completed radar map. Figure 15 provides an overview of our data processing. There are three major steps. The starting data is in the form of quadrature voltages versus delay for many pulses. The first data processing step converts this data to the form of quadrature voltages versus pulse number for many ranges. (This first step has been completed for all of the data using programs provided by Don Campbell of the Arecibo Observatory.) The second data processing step performs a spectral analysis upon these voltages to obtain a measure of backscattered power from the Moon. The third step in the data processing normalizes echo powers accounting for antenna gain, the average scattering law, and small changes in the scattering area. The fourth step in the data processing maps normalized echoes into selenographic coordinates. The second and third steps are underway and using software developed for our processing of the December 1978 observations.

Software developed since our return from Arecibo accomplishes the second and third mapping tasks -- the production of raw spectra followed by a normalization to account for various radar effects. The complete set of software to accomplish this is shown in Figure 16. We have auxiliary programs to check the Input (Sorted) Tape, to produce check displays, to copy disk data to tape for archival purposes, and to printout front cap (leading edge) spectra to provide inputs for the Normalization Program (NORMASP). These programs were developed from programs originally written for our December 1978 observations. An example of the displays of the raw and normalized spectra is shown in Figures 17 and 18.

It will be a busy summer, but we expect to have completed maps by the DPS meeting in October. In addition, we hope to return to Arecibo this fall to continue these observations. (Possible observing times in September, October, November and December 1981 are given in Tables 2 and 3.)

At this point in this discussion, it is appropriate to point out that the success that we had in these May observations was due to several people from other organizations. Jean Dickey of JPL (who works for Jim Williams) provided us with an ephemeris. In addition, the entire staff of the Arecibo Observatory provided us with excellent support in all phases of the observations. Don Campbell of the Arecibo Observatory is singled out for his support. He was responsible for outfitting the auxiliary antenna for operations at 430 Mhz and was responsible for putting together the data acquisition and sorting programs used in our observations. Without the help of these people, we would not have had the success which we had.

In summary, we have had a very successful observing run at the Arecibo Observatory during May 1981. Good data was obtained on five nights when data for a mix of inner and limb areas was acquired. We are currently processing this new data using a PDP-11/70 computer located in the Sorrento Valley, La Jolla area using software which was modified from our December 1978 observations. We expect to complete the bulk of this processing by the end of September 1981. (Much of the routine processing will be done by a summer student.) We expect to present results at this fall's DPS meeting and to continue the acquisition of raw data sometime during the fall of 1981.

SUMMARY

Task I: Crater Studies

Accomplishments:

1) A revised manuscript of a paper entitled Comparison of Radar Images of Craters on Venus and the Moon: Evidence for a Steady-State Venus Crater Population was returned to Academic Press for publication in Icarus (see Appendix A).
2) The galley proofs of an article entitled Lunar Craters with Radar Bright Ejecta was returned to Academic Press; this will soon appear in Icarus (see Appendix B).

Expected Progress Before the Next Quarterly Report:

3) The most recent radar maps of Venus from Arecibo, Goldstone, and the PVO Radar Mapper will be acquired in order to continue our study of Venus crater forms.

Task II: High Resolution Mapping of the Moon

Accomplishments:

4) Highly successful observations in May 1981 acquiring high resolution data for five lunar areas (one-quarter of the total data processing for these data have been completed).
5) A proposal for more observations in the fall of 1981 has been submitted to the Arecibo Observatory.

Expected Progress Before the Next Quarterly Progress Report:

6) Completed processing of the five data sets obtained in May 1981.
7) Prepare for the November 1981 observations.

TABLE I: SUMMARY - ARECIBO LUNAR MAPPING - MAY 1981

DAY	TARGET	PULSE LENGTH	RANGE* RES	FREQ* RES	NUM RANGE BINS	TAPE	NUM CIP	POL RCVR
06 MAY 81	THEOPHILUS	10 μs	3.9km	3.8km	512	AO6335	5	AUX
07 MAY 81	PTOLEMAEUS	10 μs	3.2km	3.7km	512	AO6358	10	AUX
						AO6359	10	AUX
						AO6360	10	MAIN
						AO6361	10	MAIN
08 MAY 81	MONTES APPENINUS	10 μs	3.7km	3.5km	512	TT8106	16	AUX
						TT8107	16	AUX
						TT8108	16	MAIN
						TT8109	16	MAIN
09 MAY 81	PLATO	12 μs	2.5km	3.5km	1024	TT8116	8	AUX
						TT8117	8	AUX
						TT8118	8	MAIN
						TT8119	8	MAIN
10 MAY 81	TYCHO	12 μs	2.5km	3.3km	1024	TT8126	7	AUX
						TT8127	8	AUX
						TT8128	8	MAIN
						TT8129	8	MAIN
	LEADING EDGE	12 μs	--	--	512	AO1529	11	AUX
			--	--		AO6335	11	AUX
11 MAY 81	SOUTH POLE	15 μs	3.0km	3.1km	800	TT8141	10	AUX
						TT8142	10	AUX
						TT8143	10	MAIN
						TT8144	6	MAIN

* RANGE AND FREQ. RESOLUTION = RADAR CELL SIZE AT BEAM CENTER

TABLE 2:

ARECIBO MOON OPPORTUNITIES

16-28 September 1981

DAY	DATE	TRANSIT AST	TRANSIT GMT	DECLINATION (NORTH)
WED	16 SEPT	02:15	06:15	3°52'
THURS	17 SEPT	03:08	07:08	9°05'
FRI	18 SEPT	04:02	08:02	13°45'
SAT	19 SEPT	04:59	08:59	17°30'
SUN	20 SEPT	05:56	09:56	20°00'
MON	21 SEPT	06:54	10:54	21°14'
TUES	22 SEPT	07:51	11:51	21°01'
WED	23 SEPT	08:47	12:47	19°28'
THURS	24 SEPT	09:40	13:40	16°47'
FRI	25 SEPT	10:30	14:30	13°13'
SAT	26 SEPT	11:18	15:18	9°03'
SUN	27 SEPT	12:03	16:03	4°31'
MON	28 SEPT	12:47	16:47	0°09'

THIRD CHOICE

ARECIBO MOON OPPORTUNITIES

13-25 October 1981

DAY	DATE	TRANSIT AST	TRANSIT GMT	DECLINATION (NORTH)
TUES	13 OCT	00:02	04:02	1°16'
WED	14 OCT	00:56	04:56	6°50'
THURS	15 OCT	01:51	05:51	11°59'
FRI	16 OCT	02:48	06:48	16°20'
SAT	17 OCT	03:48	07:48	19°31'
SUN	18 OCT	04:47	08:47	21°15'
MON	19 OCT	05:46	09:46	21°29'
TUES	20 OCT	06:43	10:43	20°18'
WED	21 OCT	07:36	11:36	17°48'
THURS	22 OCT	08:27	12:27	14°34'
FRI	23 OCT	09:15	13:15	10°34'
SAT	24 OCT	10:01	14:01	6°08'
SUN	25 OCT	10:43	14:43	1°30'

SECOND CHOICE

TABLE 3:

ARECIBO MOON OPPORTUNITIES

10-21 November 1981

DAY	DATE	TRANSIT AST	TRANSIT GMT	DECLINATION (NORTH)	
MON	9 NOV	22:38	26:38	3°49'	
TUES	10 NOV	23:32	27:32	9°20'	
THURS	12 NOV	00:30	04:30	14°18'	
FRI	13 NOV	01:30	05:30	18°16'	
SAT	14 NOV	02:31	06:31	20°51'	FIRST CHOICE
SUN	15 NOV	03:35	07:35	21°48'	
MON	16 NOV	04:35	08:35	21°10'	
TUES	17 NOV	05:32	09:32	19°07'	
WED	18 NOV	06:24	10:24	15°58'	
THURS	19 NOV	07:14	11:14	12°05'	
FRI	20 NOV	08:00	12:00	7°43'	
SAT	21 NOV	08:43	12:43	3°06'	

ARECIBO MOON OPPORTUNITIES

07-18 December 1981

DAY	DATE	TRANSIT AST	TRANSIT GMT	DECLINATION (NORTH)	
SUN	06 DEC	20:24	24:24	0°44'	
MON	07 DEC	21:15	25:15	6°22'	
TUES	08 DEC	22:10	26:10	11°37'	
WED	09 DEC	23:08	27:08	16°13'	
FRI	11 DEC	00:10	04:10	19°40'	
SAT	12 DEC	01:13	05:13	21°36'	SECOND CHOICE
SUN	13 DEC	02:16	06:16	21°49'	
MON	14 DEC	03:18	07:18	20°23'	
TUES	15 DEC	04:15	08:15	17°37'	
WED	16 DEC	05:08	09:08	13°52'	
THURS	17 DEC	05:54	09:54	9°32'	
FRI	18 DEC	06:40	10:40	5°52'	
SAT	19 DEC	07:30	11:30	0°06'	

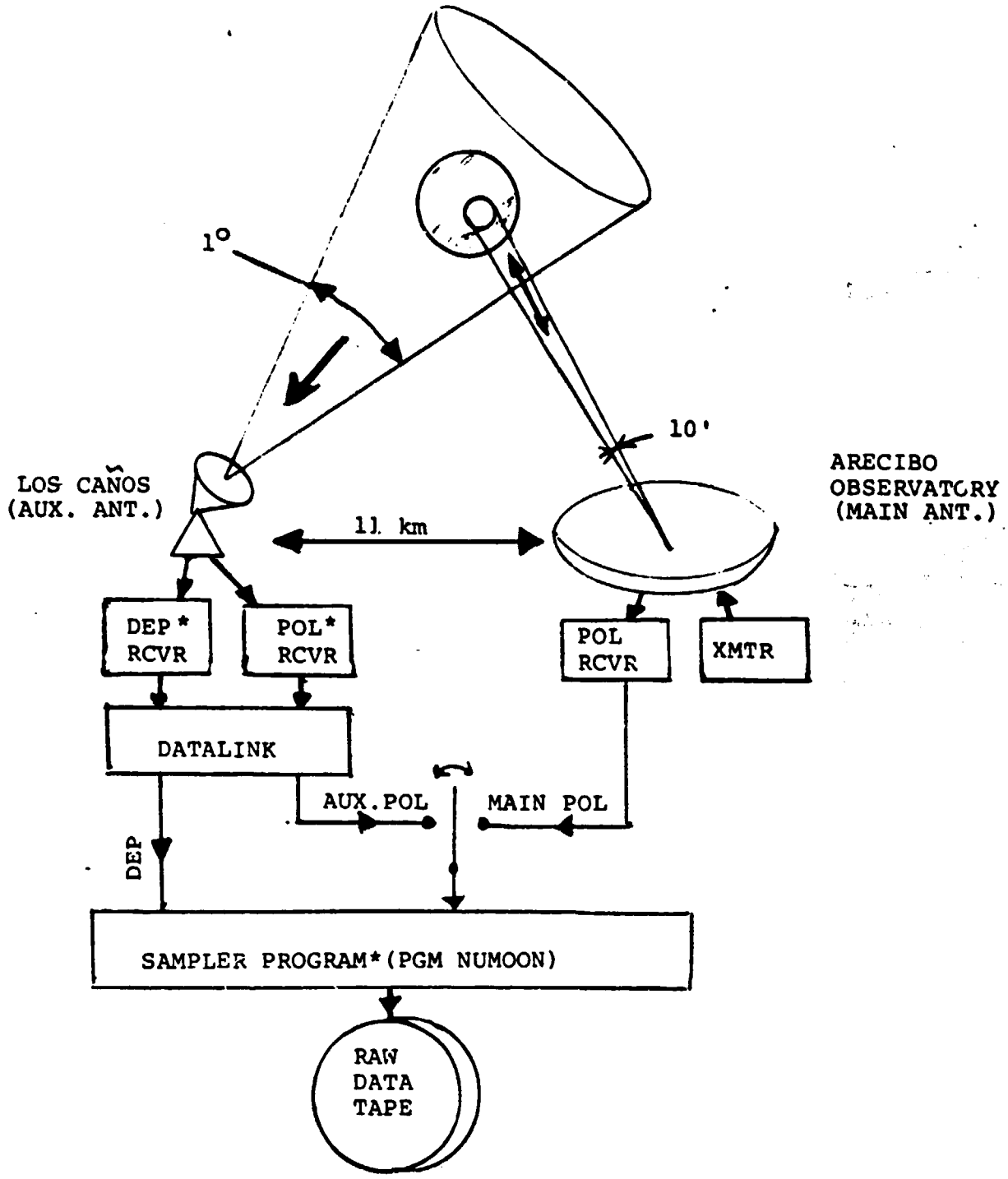

FIG. 1: REAL-TIME RADAR OPERATIONS

ARECIBO LUNAR RADAR MAPPING

This block diagram provides an overview to the Data Acquisition Phase of Lunar Radar Observations. Radar pulses are transmitted toward the moon using the marrow beam (10 arc-min.) of the main antenna of the Arecibo Observatory. Radar echoes from the moon are obtained at the main antenna as well as the smaller, auxillary antenna at Los Caños, located some 11 kilometers northeast of the main antenna. Asterisks (*) denote new radar elements installed specifically for these 430 Mhz radar observations of the moon.

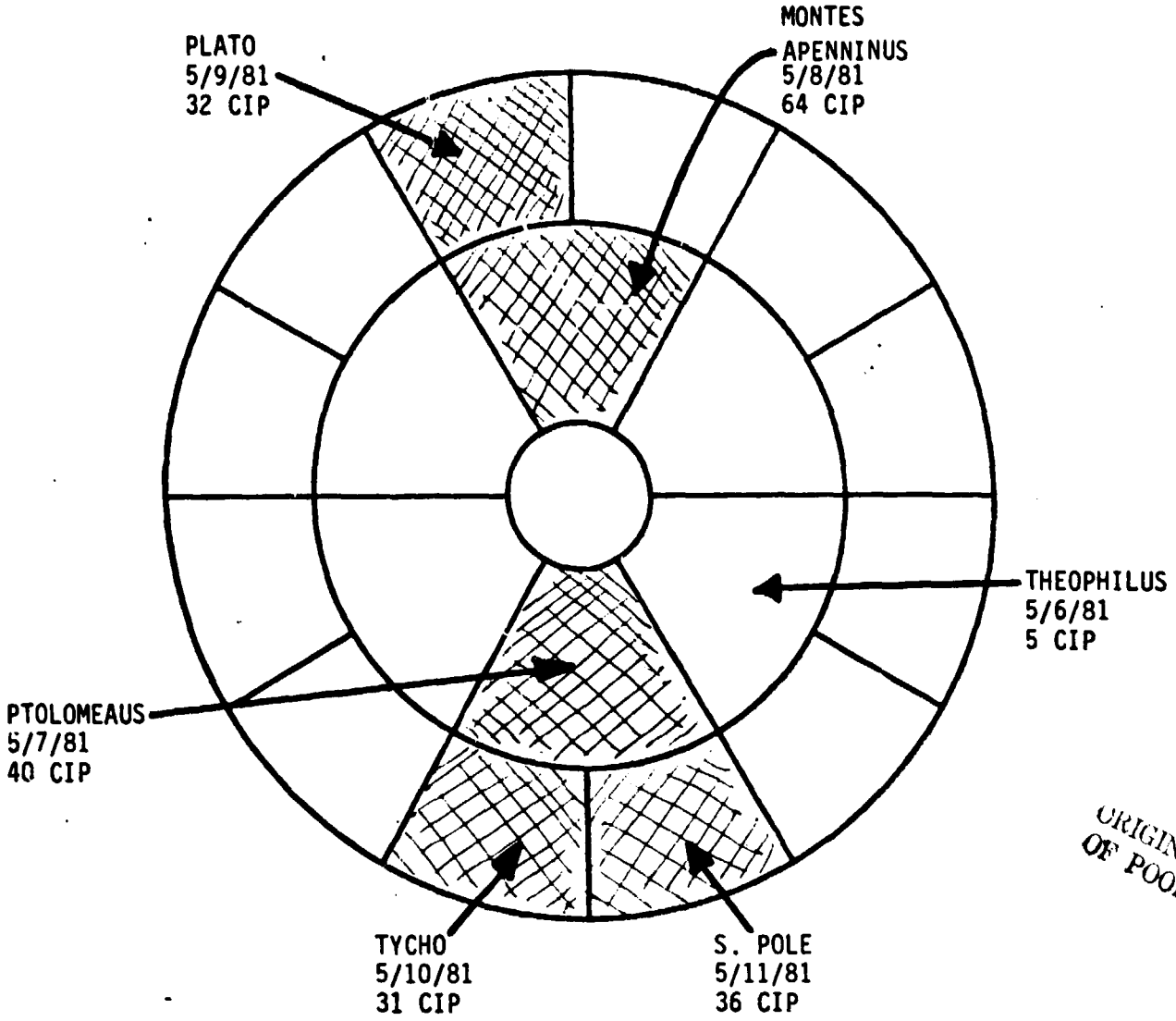

DATE	TARGET	#CIP*	XMTR PULSE** (μs)	RANGE RES.† (km)	Δf hz	FREQ. RES.† (km)
5/6/81	THEOPHILUS	5	10C	3.9	.01	3.8
5/7/81	PTOLEMEAUS	40	10C	3.2	.01	3.7
5/8/81	M.APENNINUS	64	10C	3.7	.01	3.5
5/9/81	PLATO	32	12U	2.5	.01	3.5
5/10/81	TYCHO	31	12U	2.5	.01	3.3
5/11/81	S.POLE	36	15U	3.0	.01	3.1

** C = CODED (13 element Barker Code)
U = UNCODED

† Range and Frequency Resolution at Antenna Beam Center

* CIP = Coherent Integration Period (102.4 sec typically)

FIGURE 2 SUMMARY OF MAY '81 OBSERVATIONS

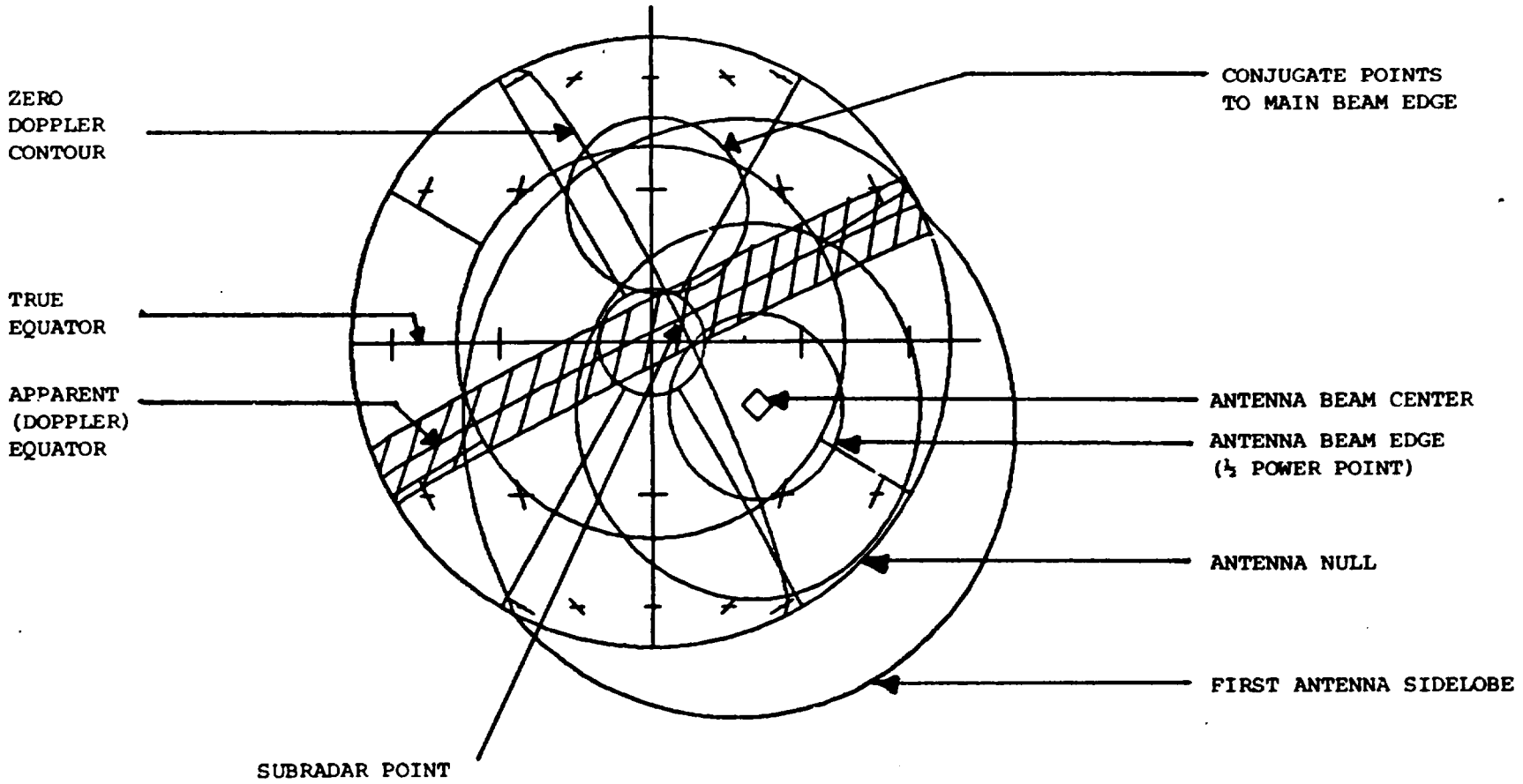

FIGURE 3: EXPLANATION OF MOON RADAR MAPPING OF GEOMETRY FIGURES TO FOLLOW

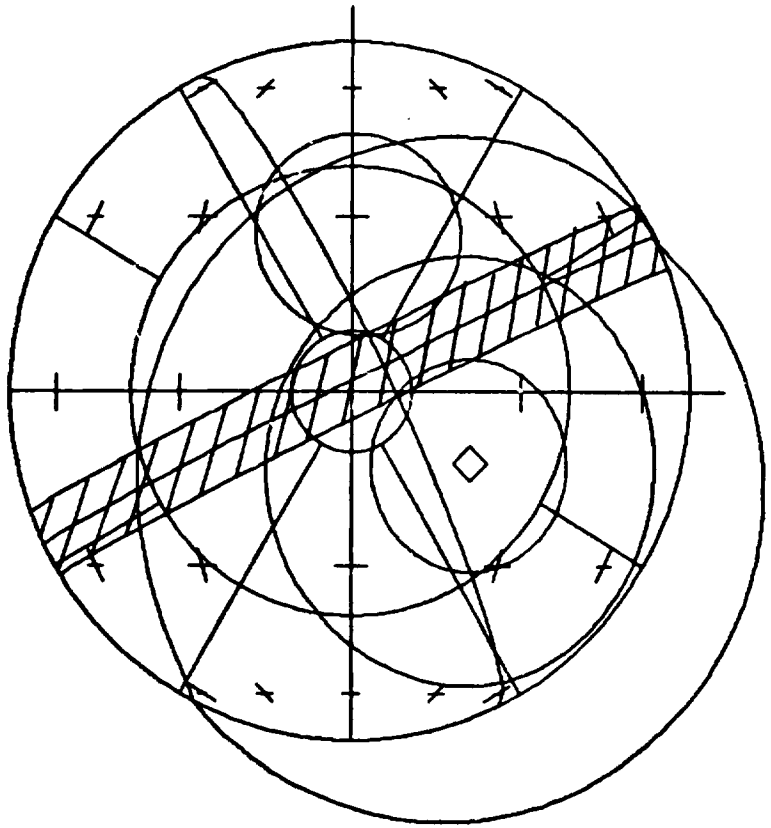

MOON PLOT FOR 14 0 ON 5 6 1981

LONG SUBRADAR POINT(DEG)	5.21
LAT SUBRADAR POINT(DEG)	0.81
DOPPLER ANGLE(DEG)	-25.98
CENTER-LIMB FREQ DIFF(CPS)	4.58
LIMB---LIMB FREQ DIFF(CPS)	9.17
DELAY(SEC)	2.380756
MOON DIAMETER(MIN-ARC)	33.50

BEAM CO-ORDINATES - LONGITUDE(DEG) 21.000 LATITUDE -12.000

RADIUS OF PLOT(IN) 3.00

BEAM CENTER

DELAY RESOLUTION (KM) =	3.885
FREQ. RESOLUTION (KM) =	3.817
DELAY SEPARATION (MICROSEC)	10.000
FREQ. SEPARATION (CPS)	0.010

ACROSS BEAM

MIN. DELAY (MILLISEC) =	0.045
MAX. DELAY (MILLISEC) =	3.143
DELAY SPREAD(MILLISEC)=	3.098
NO. OF DELAY BOXES =	309
FREQ. SPREAD (CPS) =	2.737
NO. OF FREQ. BOXES =	273

AT MAP CENTER

DELAY(MILLISEC) =	0.899
FREQ(CPS) =	-0.538
NUM RANGE BOXES (MIN TO CENTER) =	85
NUM RANGE BOXES (CENTER TO MAX) =	224
NUM FREQ BOXES (MIN TO CENTER) =	136
NUM FREQ BOXES (CENTER TO MAX) =	136

FIGURE 4: MOON RADAR MAPPING GEOMETRY FOR 06 MAY 1981 - THEOPHILUS

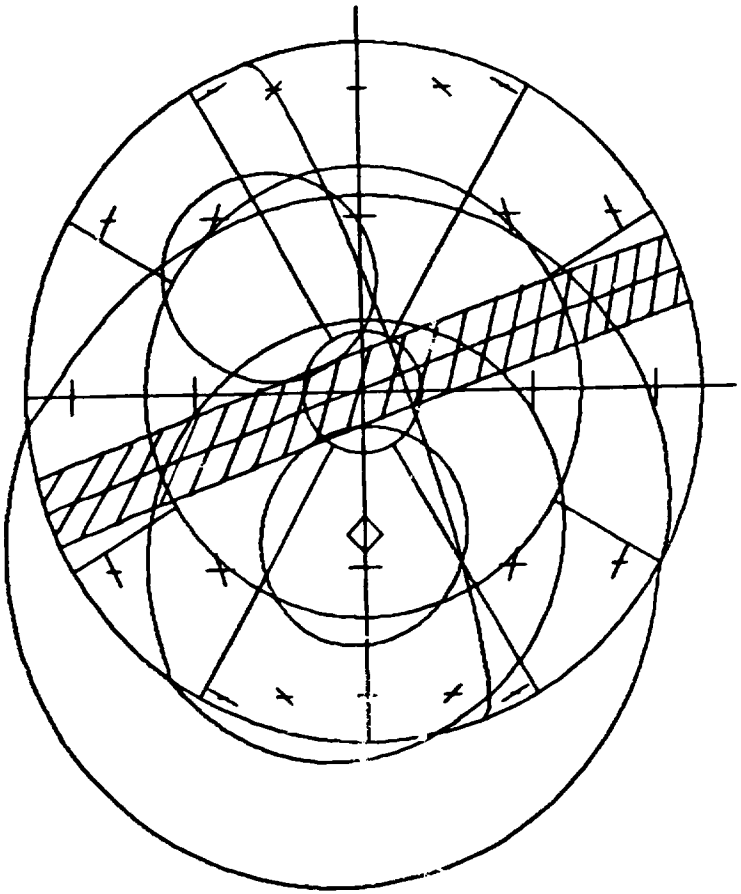

```
MOON PLOT FOR 15  0 ON  5  7 1981

 LONG SUBRADAR POINT(DEG)      6.60
 LAT SUBRADAR POINT(DEG)       2.95

 DOPPLER ANGLE(DEG)          -19.80
 CENTER-LIMB FREQ DIFF(CPS)    4.84
 LIMB---LIMB FREQ DIFF(CPS)    9.68

 DELAY(SEC)                  2.416030
 MOON DIAMETER(MIN-ARC)       33.01

BEAM CO-ORDINATES - LONGITUDE(DEG)     0.000 LATITUDE   -24.000

RADIUS OF PLOT(IN) 3.00

  BEAM CENTER
 DELAY RESOLUTION (KM) =  3.226
 FREQ. RESOLUTION (KM) =  3.708

 DELAY SEPARATION (MICROSEC)    10.000
 FREQ. SEPARATION (CPS)          0.010

ACROSS BEAM
 MIN. DELAY (MILLISEC) =  0.153
 MAX. DELAY (MILLISEC) =  4.167
 DELAY SPREAD(MILLISEC)=  4.014
 NO. OF DELAY BOXES    =  401
 FREQ. SPREAD  (CPS)   =  2.932
 NO. OF FREQ. BOXES    =  293


AT MAP CENTER
DELAY(MILLISEC) =  1.329
FREQ(CPS)       =  1.207
 NUM RANGE BOXES (MIN TO CENTER)  = 117
 NUM RANGE BOXES (CENTER TO MAX)  = 285
 NUM FREQ  BOXES (MIN TO CENTER)  = 146
 NUM FREQ  BOXES (CENTER TO MAX)  = 146
```

FIGURE 5: MOON RADAR MAPPING GEOMETRY FOR FIRST OBSERVATIONS ON 07 MAY 1981 - PTOLOMEAUS

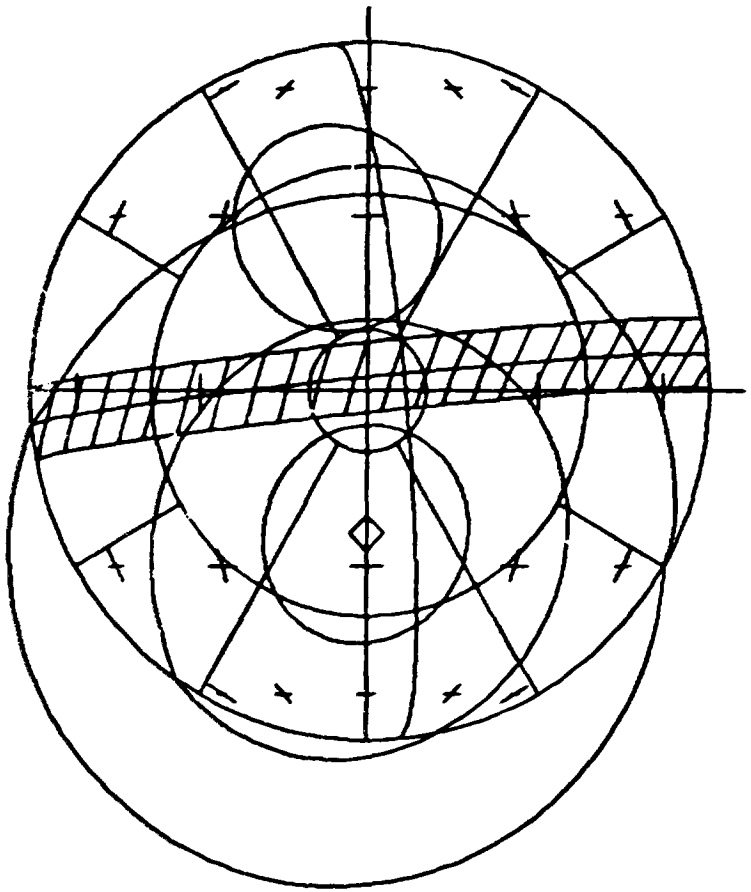

```
MOON PLOT FOR 17  0 ON  5  7 1981

 LONG SUBRADAR POINT(DEG)      6.20
 LAT SUBRADAR POINT(DEG)       2.87

 DOPPLER ANGLE(DEG)           -5.50
 CENTER-LIMB FREQ DIFF(CPS)    5.01
 LIMB---LIMB FREQ DIFF(CPS)   10.02

 DELAY(SEC)                    2.416030
 MOON DIAMETER(MIN-ARC)       33.01

BEAM CO-ORDINATES - LONGITUDE(DEG)      0.000 LATITUDE    -24.000

RADIUS OF PLOT(IN) 3.00

  BEAM CENTER
 DELAY RESOLUTION (KM) =  3.248
 FREQ. RESOLUTION (KM) =  3.500

 DELAY SEPARATION (MICROSEC)     10.000
 FREQ. SEPARATION (CPS)           0.010

ACROSS BEAM
 MIN. DELAY (MILLISEC) =  0.140
 MAX. DELAY (MILLISEC) =  4.131
 DELAY SPREAD(MILLISEC)=  3.983
 NO. OF DELAY BOXES    =  390
 FREQ. SPREAD  (CPS)   =  3.035
 NO. OF FREQ. BOXES    =  303


AT MAP CENTER
DELAY(MILLISEC) =  1.310
FREQ(CPS)       =  0.709
 NUM RANGE BOXES (MIN TO CENTER)  = 116
 NUM RANGE BOXES (CENTER TO MAX)  = 201
 NUM FREQ  BOXES (MIN TO CENTER)  = 151
 NUM FREQ  BOXES (CENTER TO MAX)  = 151
```

FIGURE 6: MOON RADAR MAPPING GEOMETRY FOR LAST OBSERVATIONS ON 07 MAY 1981 - PTOLOMEAUS

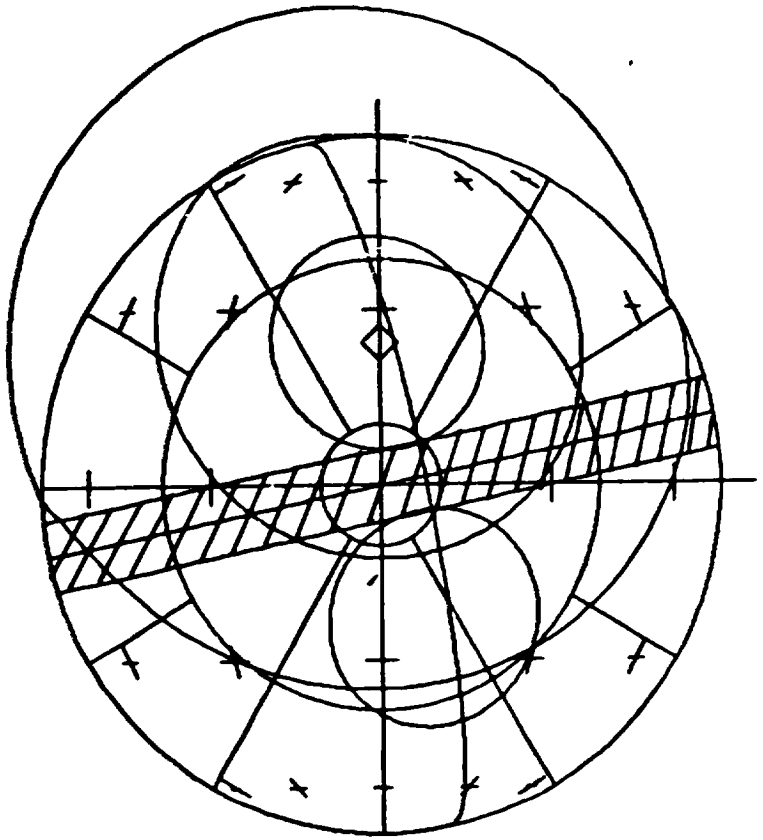

MOON PLOT FOR 16 0 ON 5 8 1981

LONG SUBRADAR POINT(DEG) 7.02
LAT SUBRADAR POINT(DEG) 1.36

DOPPLER ANGLE(DEG) -11.00
CENTER-LIMB FREQ DIFF(CPS) 5.49
LIMB---LIMB FREQ DIFF(CPS) 10.19

DELAY(SEC) 2.456726
MOON DIAMETER(MIN-ARC) 32.46

BEAM CO-ORDINATES - LONGITUDE(DEG) 0.000 LATITUDE 24.000

RADIUS OF PLOT(IN) 3.00

BEAM CENTER
DELAY RESOLUTION (KM) = 3.724
FREQ. RESOLUTION (KM) = 3.014

DELAY SEPARATION (MICROSEC) 10.000
FREQ. SEPARATION (CPS) 0.010

ACROSS BEAM
MIN. DELAY (MILLISEC) = 0.052
MAX. DELAY (MILLISEC) = 3.439
DELAY SPREAD(MILLISEC)= 3.387
NO. OF DELAY BOXES = 338
FREQ. SPREAD (CPS) = 3.139
NO. OF FREQ. BOXES = 313

AT MAP CENTER
DELAY(MILLISEC) = 0.992
FREQ(CPS) = 0.201
NUM RANGE BOXES (MIN TO CENTER) = 92
NUM RANGE BOXES (CENTER TO MAX) = 245
NUM FREQ BOXES (MIN TO CENTER) = 156
NUM FREQ BOXES (CENTER TO MAX) = 156

FIGURE 7: MOON RADAR MAPPING GEOMETRY FOR FIRST OBSERVATIONS ON 08 MAY 1981 - MONTES APENNINUS

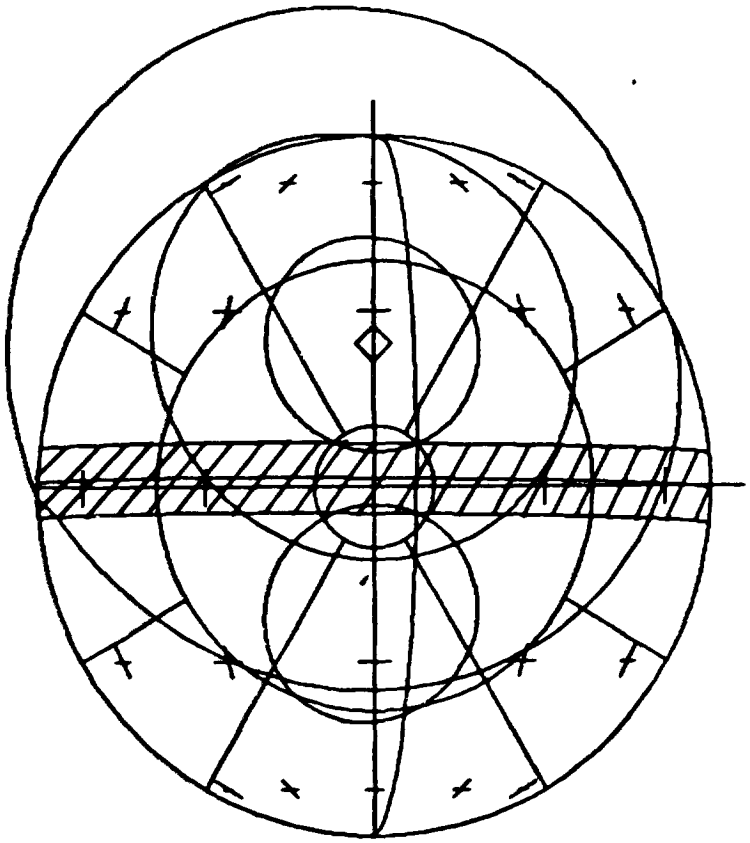

MOON PLOT FOR 18 0 ON 5 8 1981

LONG SUBRADAR POINT(DEG) 7.01
LAT SUBRADAR POINT(DEG) 1.32

DOPPLER ANGLE(DEG) 0.70
CENTER-LIMB FREQ DIFF(CPS) 4.79
LIMB---LIMB FREQ DIFF(CPS) 9.58

DELAY(SEC) 2.456726
MOON DIAMETER(MIN-ARC) 32.46

BEAM CO-ORDINATES - LONGITUDE(DEG) 0.000 LATITUDE 24.000

RADIUS OF PLOT(IN) 3.00

BEAM CENTER
DELAY RESOLUTION (KM) = 3.736
FREQ. RESOLUTION (KM) = 3.653

DELAY SEPARATION (MICROSEC) 10.000
FREQ. SEPARATION (CPS) 0.010

ACROSS BEAM
MIN. DELAY (MILLISEC) = 0.051
MAX. DELAY (MILLISEC) = 3.420
DELAY SPREAD(MILLISEC)= 3.370
NO. OF DELAY BOXES = 337
FREQ. SPREAD (CPS) = 2.951
NO. OF FREQ. BOXES = 295

AT MAP CENTER
DELAY(MILLISEC) = 0.976
FREQ(CPS) = 0.557
NUM RANGE BOXES (MIN TO CENTER) = 92
NUM RANGE BOXES (CENTER TO MAX) = 244
NUM FREQ BOXES (MIN TO CENTER) = 147
NUM FREQ BOXES (CENTER TO MAX) = 147

FIGURE 8: MOON RADAR MAPPING GEOMETRY FOR LAST OBSERVATIONS ON 08 MAY 1981 - MONTES APENNINUS

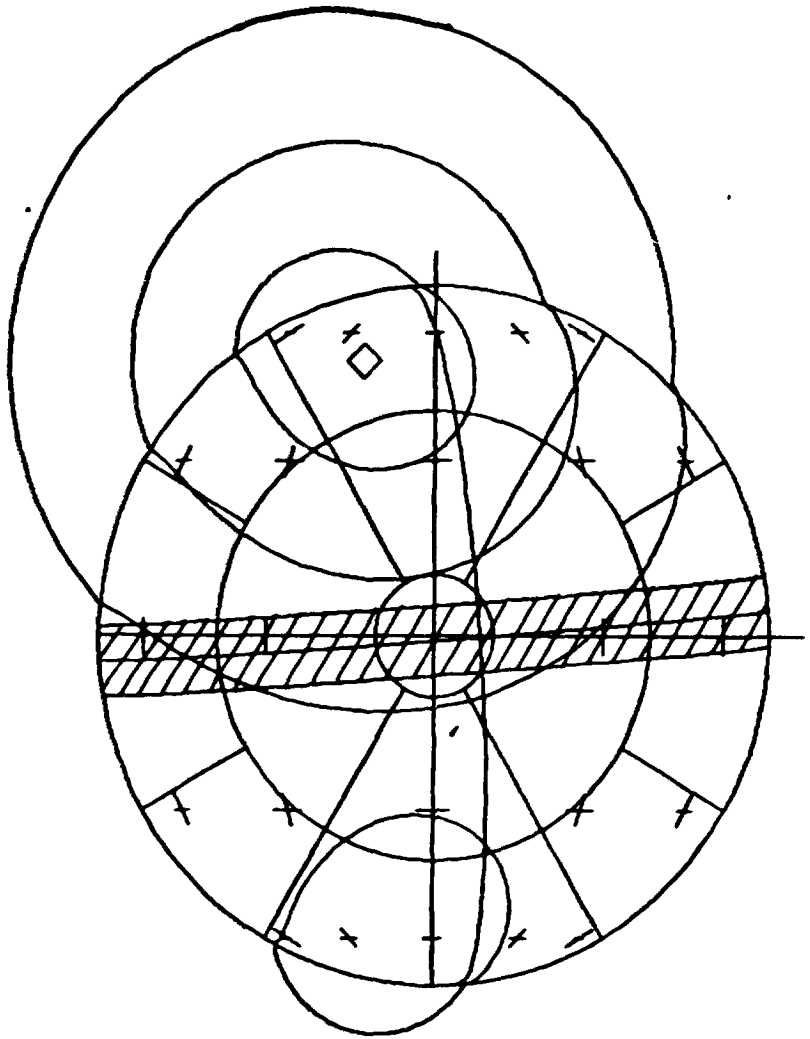

MOON PLOT FOR 17 0 ON 5 9 1981

LONG SUBRADAR POINT(DEG) 7.74
LAT SUBRADAR POINT(DEG) -0.25

DOPPLER ANGLE(DEG) -0.30
CENTER-LIMB FREQ DIFF(CPS) 5.34
LIMB---LIMB FREQ DIFF(CPS) 10.68

DELAY(SEC) 2.49**33
MOON DIAMETER(MIN-ARC) 31.91

BEAM CO-ORDINATES - LONGITUDE(DEG) -20.000 LATITUDE 52.000

RADIUS OF PLOT(IN) 3.00

BEAM CENTER
DELAY RESOLUTION (KM) = 1.784
FREQ. RESOLUTION (KM) = 3.342

DELAY SEPARATION (MICROSEC) 10.000
FREQ. SEPARATION (CPS) 0.010

ACROSS BEAM
MIN. DELAY (MILLISEC) = 1.744
MAX. DELAY (MILLISEC) = 11.595
DELAY SPREAD(MILLISEC)= 9.851
NO. OF DELAY BOXES = 985
FREQ. SPREAD (CPS) = 3.347
NO. OF FREQ. BOXES = 334

AT MAP CENTER
DELAY(MILLISEC) = 5.317
FREQ(CPS) = 1.209
NUM RANGE BOXES (MIN TO CENTER) = 357
NUM RANGE BOXES (CENTER TO MAX) = 627
NUM FREQ BOXES (MIN TO CENTER) = 167
NUM FREQ BOXES (CENTER TO MAX) = 167

FIGURE 9: MOON RADAR MAPPING GEOMETRY FOR FIRST OBSERVATION ON 09 MAY 1981 - PLATO

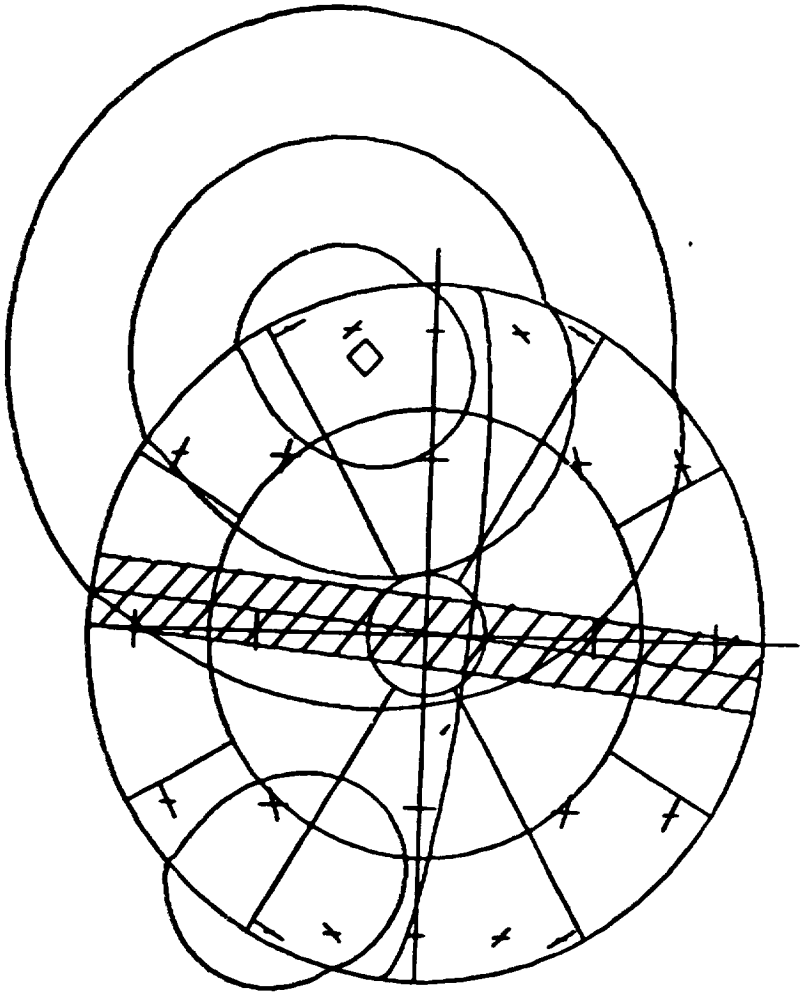

```
MOON PLOT FOR 19  0 ON  5  9 1981

 LONG SUBRADAR POINT(DEG)          7.30
 LAT SUBRADAR POINT(DEG)          -0.25

 DOPPLER ANGLE(DEG)                5.00
 CENTER-LIMB FREQ DIFF(CPS)        5.01
 LIMB---LIMB FREQ DIFF(CPS)       10.03

 DELAY(SEC)                    2.499133
 MOON DIAMETER(MIN-ARC)           31.91

BEAM CO-ORDINATES - LONGITUDE(DEG)   -20.000 LATITUDE    52.00

RADIUS OF PLOT(IN) 3.00

  BEAM CENTER
 DELAY RESOLUTION (KM) =  1.787
 FREQ. RESOLUTION (KM) =  3.718

 DELAY SEPARATION (MICROSEC)      10.000
 FREQ. SEPARATION (CPS)            0.010

ACROSS BEAM
 MIN. DELAY (MILLISEC) =  1.738
 MAX. DELAY (MILLISEC) = 11.595
 DELAY SPREAD(MILLISEC)=  9.861
 NO. OF DELAY BOXES    =  986
 FREQ. SPREAD  (CPS)   =  3.143
 NO. OF FREQ. BOXES    =  314


AT MAP CENTER
DELAY(MILLISEC) =  5.291
FREQ(CPS)       =  1.016
 NUM RANGE BOXES (MIN TO CENTER)  =  355
 NUM RANGE BOXES (CENTER TO MAX)  =  630
 NUM FREQ  BOXES (MIN TO CENTER)  =  157
 NUM FREQ  BOXES (CENTER TO MAX)  =  157
```

FIGURE 10: MOON RADAR MAPPING GEOMETRY FOR LAST OBSERVATIONS ON 09 MAY 1981 - PLATO

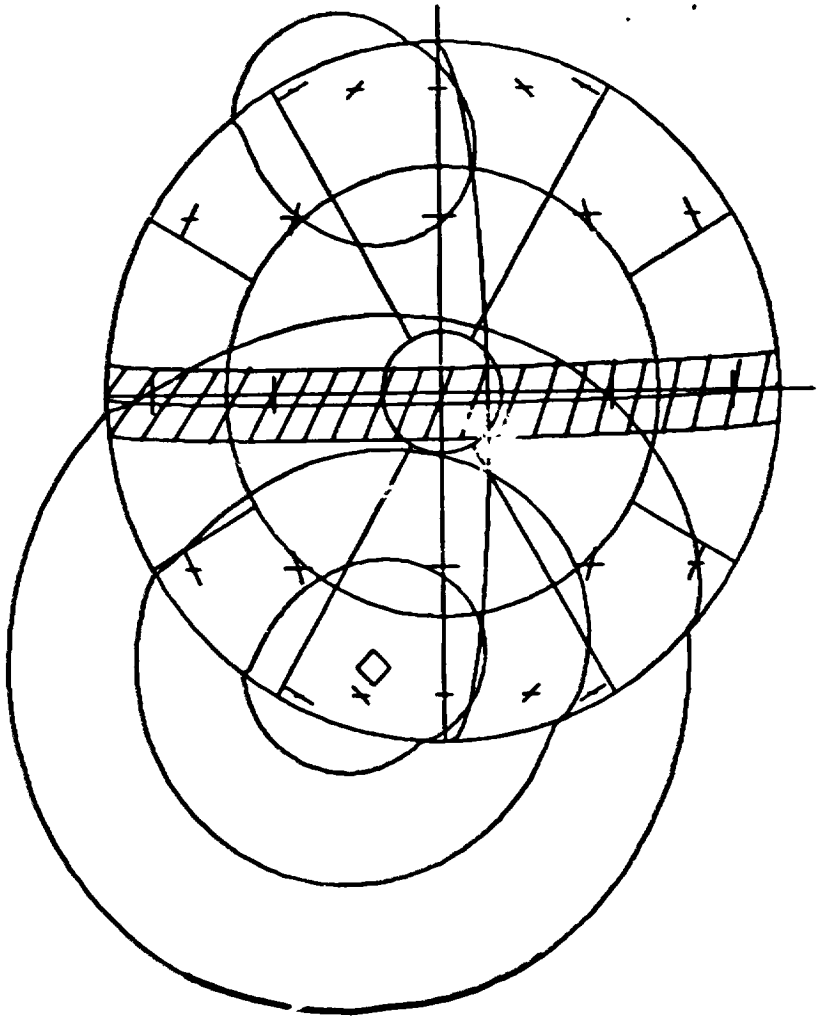

```
MOON PLOT FOR 17 30 ON  5 10 1981

 LONG SUBRADAR POINT(DEG)      7.70
 LAT SUBRADAR POINT(DEG)      -1.77

 DOPPLER ANGLE(DEG)           -0.00
 CENTER-LIMB FREQ DIFF(CPS)    5.45
 LIMB---LIMB FREQ DIFF(CPS)   10.90

 DELAY(SEC)                    2.540110
 MOON DIAMETER(MIN-ARC)       31.00

BEAM CO-ORDINATES - LONGITUDE(DEG)   -20.000 LATITUDE    -52.000

RADIUS OF PLOT(IN) 3.00

  BEAM CENTER
 DELAY RESOLUTION (MU) =  1.024
 FREQ. RESOLUTION (MU) =  3.340

 DELAY SEPARATION (MICROSEC)     10.000
 FREQ. SEPARATION (CPS)           0.010

ACROSS BEAM
 MIN. DELAY (MILLISEC) =  1.579
 MAX. DELAY (MILLISEC) = 11.595
 DELAY SPREAD(MILLISEC)= 10.016
 NO. OF DELAY BOXES    = 1001
 FREQ. SPREAD  (CPS)   =  3.472
 NO. OF FREQ. BOXES    =  347


AT MAP CENTER
DELAY(MILLISEC) =  6.995
FREQ(CPS)       =  1.018
 NUM RANGE BOXES (MIN TO CENTER)  = 341
 NUM RANGE BOXES (CENTER TO MAX)  = 659
 NUM FREQ  BOXES (MIN TO CENTER)  = 173
 NUM FREQ  BOXES (CENTER TO MAX)  = 173
```

FIGURE 11: MOON RADAR MAPPING GEOMETRY FOR FIRST RADAR OBSERVATIONS ON 10 MAY 1981 - TYCHO

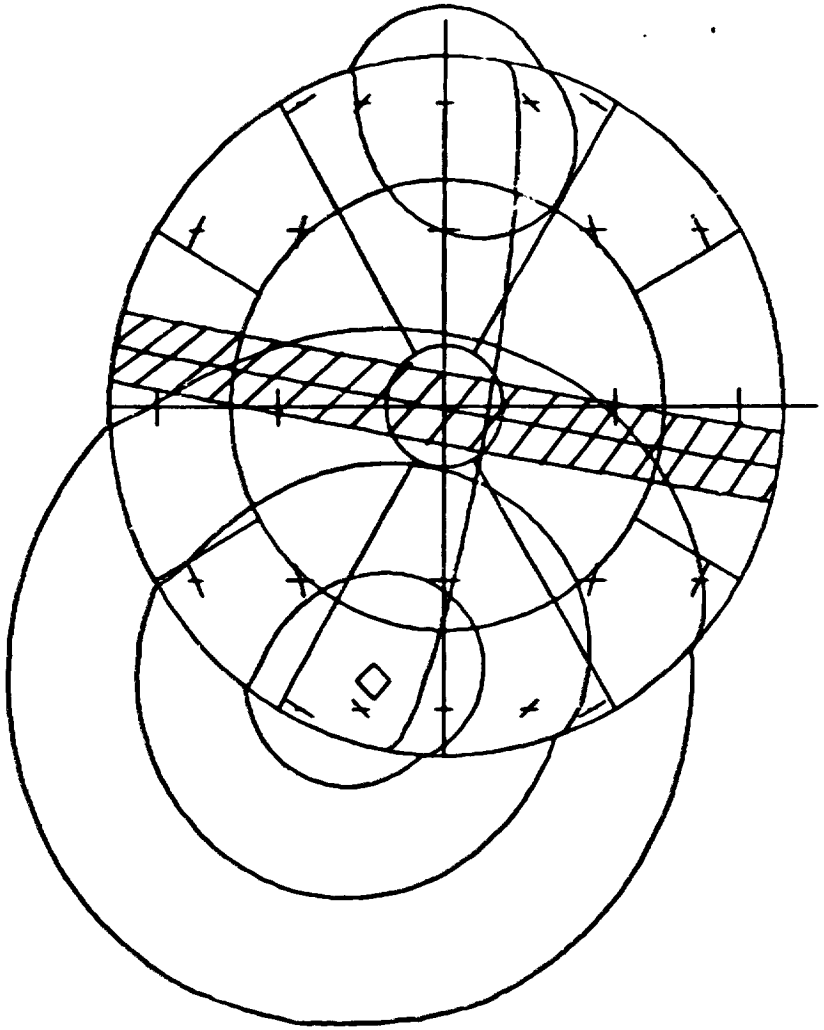

MOON PLOT FOR 20 0 04 5 10 1981

LONG SUBRADAR POINT(DEG) 7.35
LAT SUBRADAR POINT(DEG) -1.72

DOPPLER ANGLE(DEG) 9.98
CENTER-LIMB FREQ DIFF(CPS) 5.20
LIMB---LIMB FREQ DIFF(CPS) 10.40

DELAY(SEC) 2.5e0110
[illegible] DIAMETER(MIN-ARC) 31.40

BEAM CO-ORDINATES - LONGITUDE(DEG) -20.000 LATITUDE -52.000

RADIUS OF PLOT(IN) 3.00

BEAM CENTER
DELAY RESOLUTION (MU) = 1.026
FREQ. RESOLUTION (MU) = 3.379

DELAY SEPARATION (MICROSEC) 10.000
FREQ. SEPARATION (CPS) 0.010

ACROSS BEAM
MIN. DELAY (MILLISEC) = 1.574
MAX. DELAY (MILLISEC) = 11.595
DELAY SPREAD(MILLISEC)= 10.021
NO. OF DELAY BOXES = 1002
FREQ. SPREAD (CPS) = 3.312
NO. OF FREQ. BOXES = 331

AT MAP CENTER
DELAY(MILLISEC) = 6.984
FREQ(CPS) = 0.759
NUM RANGE BOXES (MIN TO CENTER) = 300
NUM RANGE BOXES (CENTER TO MAX) = 701
NUM FREQ BOXES (MIN TO CENTER) = 165
NUM FREQ BOXES (CENTER TO MAX) = 165

FIGURE 12: MOON RADAR MAPPING GEOMETRY FOR LAST OBSERVATIONS ON 10 MAY 1981 - TYCHO

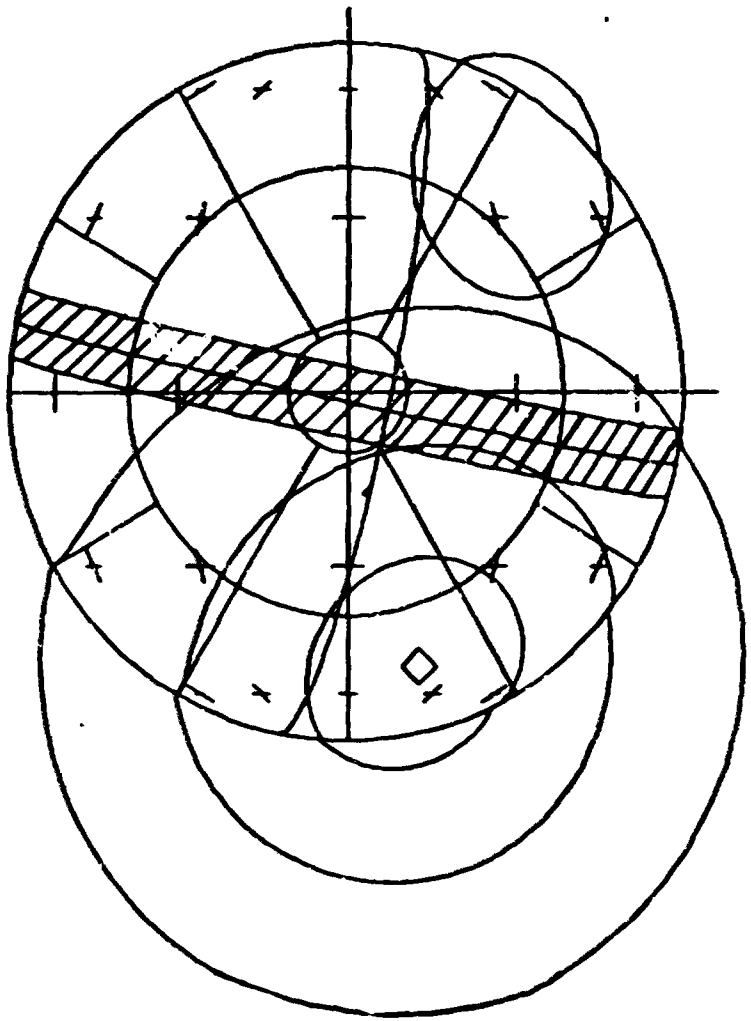

MOON PLOT FOR 20 30 GM 5 11 1981

LONG SUBRADAR POINT(DEG) 0.69
LAT SUBRADAR POINT(DEG) -3.06

DOPPLER ANGLE(DEG) 11.50
CENTER-LIMB FREQ DIFF(CPS) 5.50
LIMB---LIMB FREQ DIFF(CPS) 11.16

DELAY(SEC) 2.007674
MOON DIAMETER(MIN-ARC) 30.50

BEAM CO-ORDINATES - LONGITUDE(DEG) 20.000 LATITUDE -52.000

RADIUS OF PLOT(IN) 5.00

BEAM CENTER
DELAY RESOLUTION (AM) = 1.953
FREQ. RESOLUTION (AM) = 3.250

DELAY SEPARATION (MICROSEC) 10.000
FREQ. SEPARATION (CPS) 0.010

ACROSS BEAM
MIN. DELAY (MILLISEC) = 1.189
MAX. DELAY (MILLISEC) = 11.595
DELAY SPREAD(MILLISEC)= 10.406
NO. OF DELAY BOXES = 1040
FREQ. SPREAD (CPS) = 3.649
NO. OF FREQ. BOXES = 364

AT MAP CENTER
DELAY(MILLISEC) = 6.170
FREQ(CPS) = -1.615
NUM RANGE BOXES (MIN TO CENTER) = 298
NUM RANGE BOXES (CENTER TO MAX) = 742
NUM FREQ BOXES (MIN TO CENTER) = 182
NUM FREQ BOXES (CENTER TO MAX) = 182

FIGURE 13: MOON RADAR MAPPING GEOMETRY FOR FIRST OBSERVATIONS ON 11 MAY 1981 - SOUTH POLE

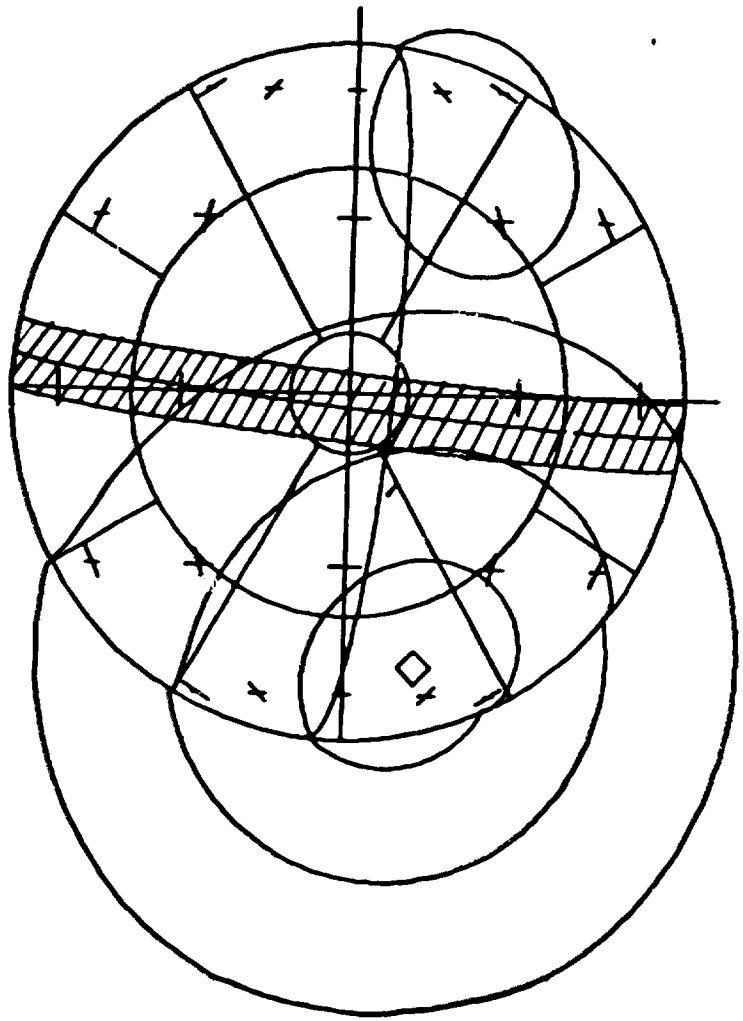

```
MOON PLOT FOR 18 30 0m  5 11 1981

 LONG SUBRADAR POINT(DEG)      7.18
 LAT SUBRADAR POINT(DEG)      -3.13

 DOPPLER ANGLE(DEG)            5.50
 CENTER-LIMB FREQ DIFF(CPS)    5.97
 LIMB---LIMB FREQ DIFF(CPS)   11.94

 DELAY(SEC)                    2.687674
 MOON DIAMETER(MIN-ARC)       30.58

BEAM CO-ORDINATES - LONGITUDE(DEG)    20.000 LATITUDE   -52.000

RADIUS OF PLOT(IN) 3.00

  BEAM CENTER
 DELAY RESOLUTION (AM) =  1.957
 FREQ. RESOLUTION (AM) =  2.076

 DELAY SEPARATION (MICROSEC)     10.000
 FREQ. SEPARATION (CPS)           0.010

ACROSS BEAM
 MIN. DELAY (MILLISEC) =  1.179
 MAX. DELAY (MILLISEC) = 11.595
 DELAY SPREAD(MILLISEC)= 10.416
 NO. OF DELAY BOXES  = 1041
 FREQ. SPREAD  (CPS)  =  3.000
 NO. OF FREQ. BOXES  =  300


AT MAP CENTER
DELAY(MILLISEC) =  6.146
FREQ(CPS)       = -1.203
 NUM RANGE BOXES (MIN TO CENTER)  = 296
 NUM RANGE BOXES (CENTER TO MAX)  = 744
 NUM FREQ  BOXES (MIN TO CENTER)  = 195
 NUM FREQ  BOXES (CENTER TO MAX)  = 195
```

FIGURE 14: MOON RADAR MAPPING GEOMETRY FOR LAST OBSERVATIONS ON 11 MAY 1981 - SOUTH POLE

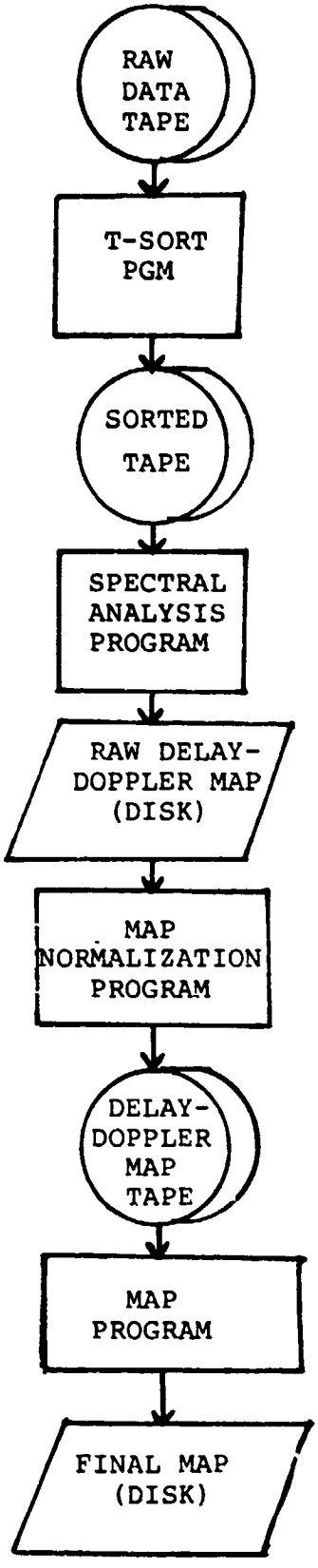

Received Voltages (I and Q) versus delay

For N Pulses

Received Voltages (I and Q) versus consecutive 1024 pulses

For all Delays

Raw Power versus Delay and Doppler Frequency

For Several Coherent Integration Periods (CIP's)

Normalized Power versus Delay and Doppler Frequency

For Many CIP's

Normalized Power versus Selenographic Position

For all CIP's Summed

FIGURE 15: OVERVIEW OF LUNAR RADAR DATA PROCESSING

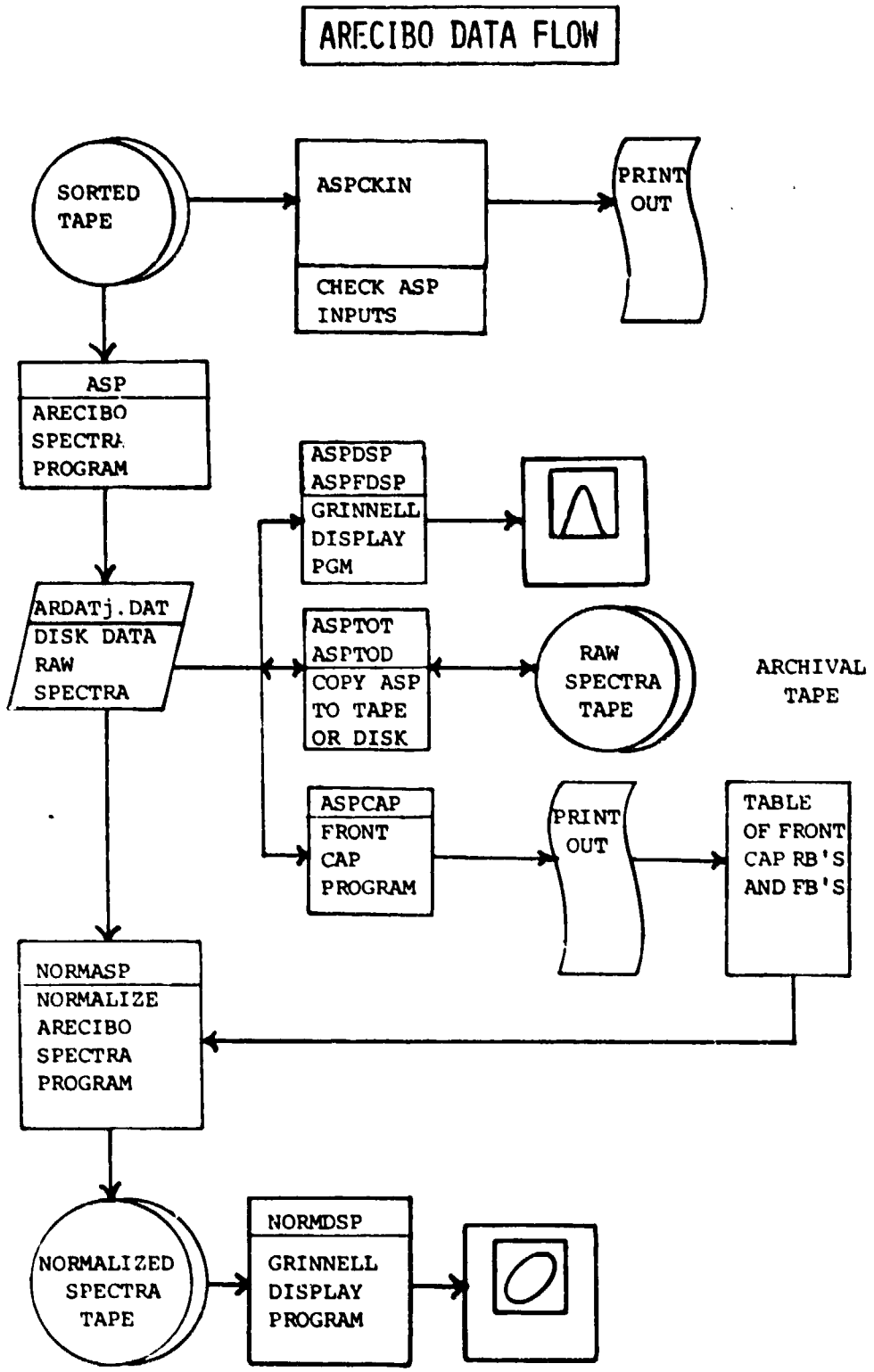

FIGURE 16: COMPUTER PROGRAMS FOR ARECIBO MAP PRODUCTION AS OF 01 AUGUST 1981.

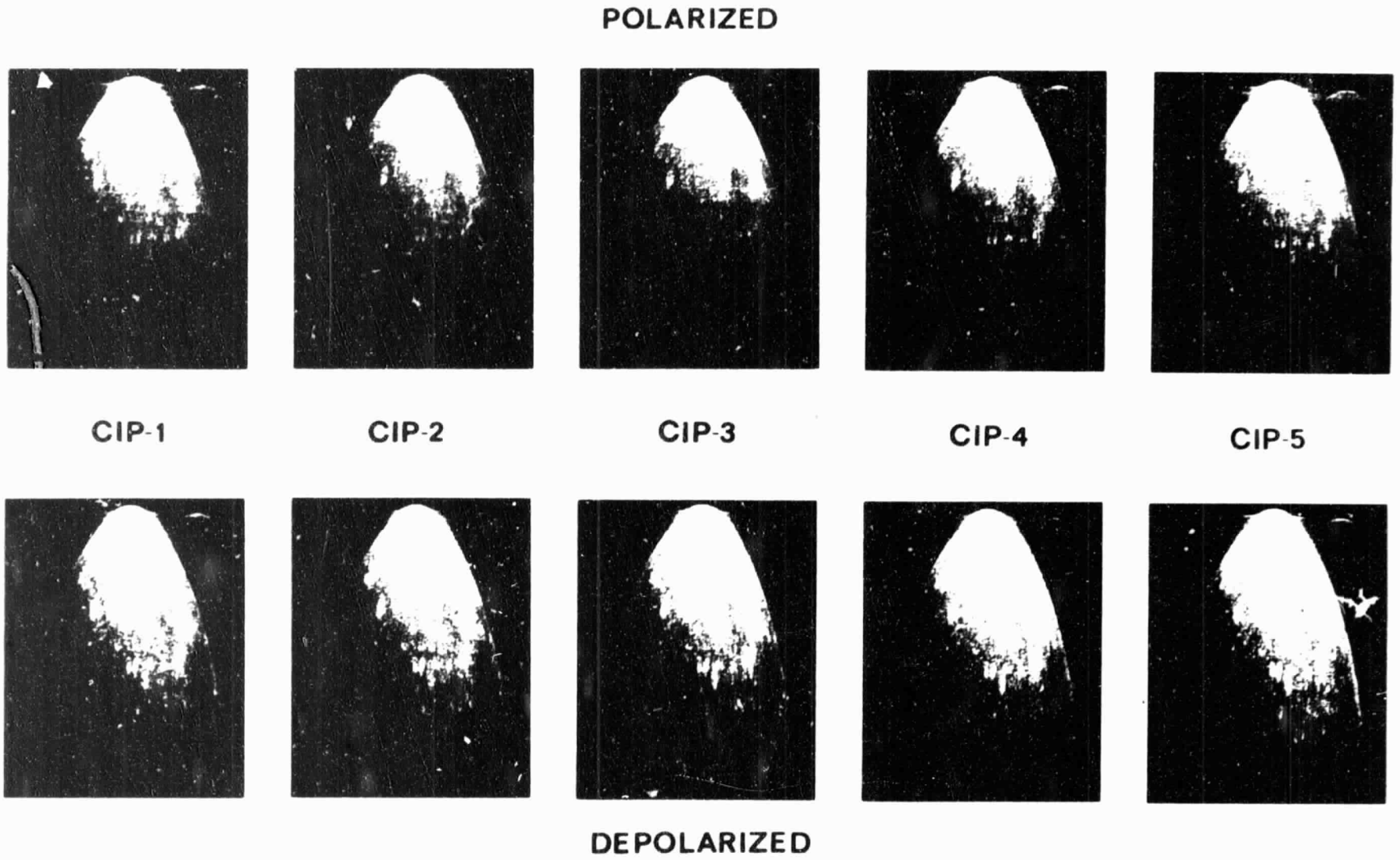

FIGURE 17: Raw Radar Spectra for 05 May 81 - Theophilus.
Five consectutive coherent integration periods (CIP's) are shown.
Doppler frequency run horizontally; Range (delay) runs vertically;
Echo power is indicated by image brightness.

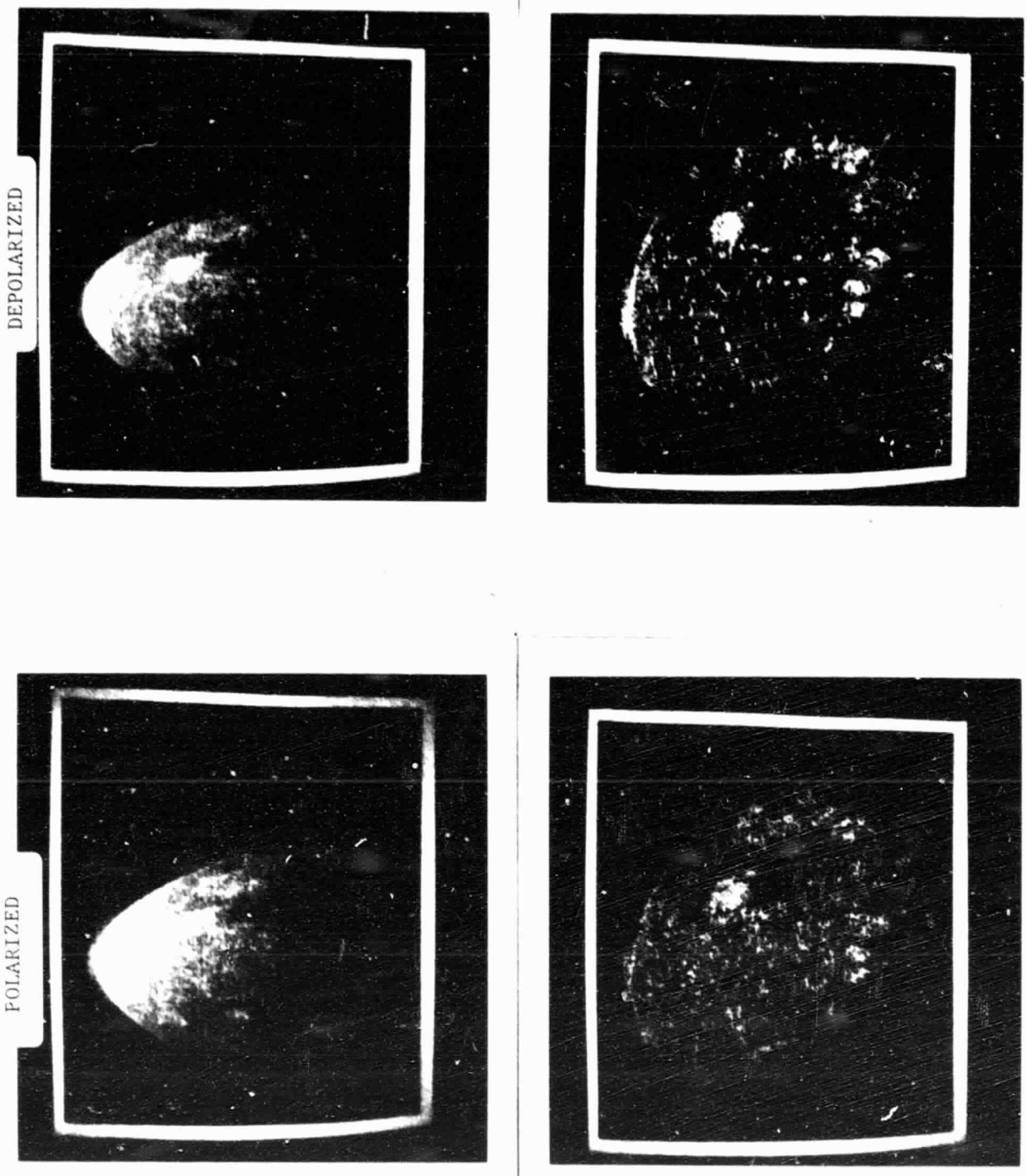

FIGURE 18: Raw and Normalized Delay-Doppler Radar Maps of Theophilus (CIP=5).

APPENDIX A

ORIGIN OF BRIGHT RING SHAPED CRATERS IN RADAR IMAGES OF VENUS

James A. Cutts

Thomas W. Thompson

Blake H. Lewis

Planetary Science Institute

Science Applications, Inc.

283 South Lake Avenue, Suite 218

Pasadena, California 91101

Submitted November 1980

Revised July 1981

Icarus

PSI Contribution #142

Proposed running head:

Origin of Venus Radar Craters

Direct editorial correspondence and proofs to:

James A. Cutts

Planetary Science Institute

283 South Lake Avenue, Suite 218

Pasadena, CA 91101

(213) 449-4955

ABSTRACT

The surface of Venus viewed in Arecibo radar images has a small population of bright ring shaped features. These features are interpreted as the rough or blocky deposits surrounding craters of impact of volcanic origin. Population densities of these bright ring features are small compared with visually identified impact craters on the surface of the Moon and volcanic craters on Io. However, they are comparable to the short-lived radar-bright haloes associated with ejecta deposits of young craters on the Moon. This suggests that bright radar signatures of the deposits around Venusian craters are obliterated by an erosional or sedimentary process.

We have evaluated the hypothesis that bright radar crater signatures were obliterated by a global mantle deposited after impacts of very large bolides. The mechanism accounts satisfactorily for the population of features with internal diameters greater than 64 km. The measured population of craters with internal diameters between 32 and 64 km is difficult to account for with the model but it may be underestimated because of poor radar resolution (5 to 20 km).

Other possible mechanisms for the removal of radar bright crater signatures include in situ chemical weathering of rocks and mantling by young volcanic deposits. All three alternatives may be consistent with existing radar roughness and cross section data and Venera 8, 9 and 10 data. However, imaging observations from a lander on the rolling plains or lowlands may verify or disprove the proposed global mantling. New high resolution ground based radar data can also contribute new information on the nature and origin of these radar bright ring features.

INTRODUCTION

Cratering by impacting meteoroidal bodies is an ubiquitous process on those solar system bodies with solid surfaces. Impact craters have been recognized on the Earth's surface and on the surfaces of Mercury, the Moon, Mars and the satellites of Jupiter and Saturn. Craters are formed by volcano-tectonic[1] processes also. Craters of unequivocal volcano-tectonic origin occur on the Earth and Mars and are extraordinarily abundant on the Jovian moon Io. In recent years the cloud-shrouded surface of Venus has been imaged with radar, revealing circular features on that planet. These features appear to be craters and whether they are primarily of impact or volcano-tectonic origin is now exciting considerable interest.

Radar images displaying different aspects of the slope and roughness characteristics of the Venusian surface have now been obtained with the Goldstone facility (Jurgens et al., 1980), Arecibo Observatory (Campbell and Burns, 1980), Pioneer Venus Orbiter side-looking mode (Masursky et al., 1980) and Pioneer Venus Orbiter vertical incidence mode (Pettengill et al., 1980). Elevation data have also been obtained for small areas from the Goldstone facility (Jurgens et al., 1980) and globally from the Pioneer Venus Orbiter (Pettengill et al., 1980).

---

[1] the term volcano-tectonic denotes some process of endogenic character that form craters and which probably is volcanic or tectonic in character.

The papers cited are the most recent. In them the interested reader can find a comprehensive description of earlier work.

A variety of large (250-1300 km diameter) quasi-circular diffuse radar-dark features have been seen in all four radar image data sets, although the appearances of these features may differ in the various data sets. Campbell and Burns (1980) describe twelve such features in the Arecibo images, most of which have single small bright spots in their interiors. They find little correlation between the relief of these features and the Pioneer Venus altimetry map. However, Masursky et al. (1980) consider these features to be lava filled impact basins and note that their size frequency distribution is consistent with that observed for impact basins on the Moon and Mars.

A number of smaller (20-250 km diameter) features have also been recognized in the radar imagery which display much crisper morphologic or topographic detail than the diffuse dark features. In images taken at near vertical radar incidence angles (1^{o} to 8^{o}) with the Goldstone 12.6 cm radar, slopes dictate the magnitude and character of the signal returns and near circular features with inward sloping margins have been recognized and interpreted as impact craters (Rumsey et al., 1974; Saunders and Malin, 1976). In images obtained over a much broader range of radar incidence angles (10^{o} to 70^{o}) at 12.5 cm by the Arecibo Observatory, a large number of bright ring-shaped features between 20 and 260 km in diameter have

been detected (e.g., Fig. 1a) and were tentatively identified as craters by Campbell and Burns (1980) but these workers drew no definite conclusions about their origin. Abundances of these bright ring-shaped features seen in the Arecibo images are lower than the photogeologically determined abundances of impact craters on many planetary surfaces of intermediate age such as the lunar maria and the martian plains. Campbell and Burns concluded that if all these features were impact craters then the average age of the one-quarter of the Venusian surface that they studied would be 600 million years. Since it seemed likely that at least some of these features were volcano-tectonic, the surface could have been even younger.

How does one reconcile a sparse population of smaller impact craters (the bright-ring features) with the dense population of basin-sized features (the dark features) described by Masursky et al. (1980)? There is not necessarily a conflict here. If the basins are lava filled as Masursky et al. believe, it is also possible that smaller impact craters on the adjoining terrains were obliterated using the basin-filling events. Such selective global obliteration events appear to have occurred on Mars in its early history (Chapman and Jones, 1977) and could have also occurred on Venus more recently. In this view, the bright ring-shaped features would be craters formed since the obliteration. Moreover, the observational evidence that the dark features are of impact origin is at present somewhat tenuous (Dunham and Spetzler, 1980) and it may be unnecessary to postulate exotic selective mechanisms to account for their existence.

More problematical is the data from Goldstone images showing craters in the same size range as the bright ring-shaped forms. The response of the Goldstone data to crater rim slopes is similar to that of visual images under low sun conditions. Craters are identified as pairs of mounds aligned radially to the illumination center. Saunders and Malin (1976) find a dense population of these features orders of magnitude larger than the populations of the bright rings in the Arecibo images which were obtained under radar illumination conditions analogous to high-sun photography. Although there is little overlap between the Goldstone and the Arecibo images that were used for recognizing craters and interpretive problems with both data sets, these conflicting observations are not easily reconciled.

Motivated by the puzzling aspects of the radar appearance of the lunar surface we have examined the properties and occurrence of bright ring-shaped features in the Arecibo images in the context of some recent investigations of the radar appearance of lunar craters (Thompson et al., 1980; Thompson et al., 1981). A rich collection of photogeological and thermal infrared observations were used to gain a reasonably detailed understanding of the formation and evolution of lunar crater radar signatures. The results provide some valuable insights into the mechanisms of formation and evolution of the Venusian features.

Our major thesis is that the bright ring-shaped features contain information about the rate at which Venus is being modified by depositional or erosional processes. We propose

that some of these bright ring features are the radar expression of the ejecta deposits of very young craters. We contend that older radar bright-ring features of whatever origin are now being obliterated from the radar map of Venus as rapidly as new ones are forming. Various processes capable of obliterating or masking surfaces with enhanced radar scattering properties may be responsible. We examine one such obliteration process -- mantling by large impact -- in some detail.

BACKGROUND -- RADAR CHARACTERISTICS OF LUNAR CRATERS

In their comparison of the bright ring features in the Arecibo images with the radar signatures of lunar craters, Campbell and Burns (1980) noted that the lack of adequate analysis of craters in the lunar radar data base seriously hindered useful comparisons. Here we briefly review our recent investigations of 3.8 cm and 70 cm radar and infrared signatures of lunar craters (Thompson et al., 1981). We use the term signature to refer to either the enhanced radar echo or the thermal contrast in infrared maps associated with a crater or parts of a crater.

We divided our studies of radar crater signatures into analyses of crater floor and interior properties (Thompson et al, 1980) and properties of the ejecta deposits (Thompson et al., 1981). No data yet exist for the Moon at 12.6 cm, the wavelength of the Arecibo radar observations. For this reason, we analyzed both the 3.8 cm and 70 cm radar observations which

bracket the 12.6 cm wavelength of the Venus data. We also considered thermal infrared data, which helped to distinguish between roughness and blockiness of the ejecta. These properties are not well discriminated by the radar data alone.

Lunar Crater Floors

The 3.8 cm and 70 cm radar and thermal infrared signatures of the floors of freshly formed lunar craters are found to be enhanced significantly relative to the average properties of either lunar mare or upland surfaces (Thompson et al., 1980). Studies of the lunar crater population indicate that with increasing exposure time on the lunar surface the radar and infrared signatures fade. The infrared signature is first to go; in small craters (diameter < 10 km) the 70 cm signatures follow and finally the 3.8 cm signatures disappear, but the order of disappearance is reversed in larger craters (Thompson et al., 1980). The lifetimes of the radar signatures of crater floors are found to be several billion years.

Lunar Crater Ejecta

Freshly formed lunar craters are surrounded by a broad halo of enhanced 3.8 cm radar brightness which can extend to between 10 and 20 crater radii from the crater rim (Thompson et al., 1981, Fig. 2). The initial size of the thermal infrared halo is not well defined by the existing data except for craters larger than about 10 km but appears to be slightly smaller than the 3.8 cm halo. The 70 cm halo is very much

smaller and extends to less than one crater diameter from the rim. The size and the brightness of each type of halo appears to change with exposure on the lunar surface. These changes are evidently most rapid for the IR ejecta signature, least so for the 70 cm ejecta signatures, and intermediate for the 3.8 cm ejecta signature. The 3.8 cm signatures disappear much more rapidly for the ejecta deposits (lifetimes 1.3 to 3.3 10^8 years, depending on crater size) than from crater floors (lifetimes > 10^9 years). Thompson et al. (1981) have interpreted these ejecta signatures in terms of an initial population of surface and subsurface rocks and surface roughness associated with the formation of an impact crater ejecta deposit and the subsequent modification of the ejecta deposit by lunar surface processes. The distribution of these features on the front side of the Moon is illustrated in Fig. 3(a).

BRIGHT RING FEATURES ON VENUS

Bright ring-shaped features have been identified in the Arecibo radar maps, which cover approximately 35% of the surface of Venus. Large portions of these maps were acquired at moderate to high radar incidence angles as were the lunar 70 cm and 3.8 cm maps.

Thirty-three of these features have been tentatively identified as "craters" (Campbell and Burns, 1980). The radar incidence angles at which these 33 features were observed range from 10° up to 66°. Their distribution on Venus is

illustrated in Fig. 3(b). Campbell and Burns define a "crater" as a relatively circular area of low backscatter cross section (dark) surrounded by a high contrast (bright) region of finite extent. At least four resolution cells were required for this identification and at the best resolution obtained, the smallest crater detectable was approximately 20 km in diameter. Some features conforming to the above description were not included in the list of 33 "craters." Among these is the "crater" in the Maxwell Montes at 66°N, 7°E, and the feature at 24°S, 324°W, now designated Hathor Mons. Measurements by Pioneer Venus radar altimeter indicate that these are probably raised volcanic features. Campbell and Burns variously entertain the possibility that anywhere between 0 and 100% of the remaining 33 features are of impact origin.

No data have been assembled on the number of bright spots which do not have the distinctive annular form of the features characterized above; inspection of moderate quality published maps suggests that such features are present but not abundant.

Morphological Comparisons with Radar Images of Lunar Craters

Let us compare the bright ring craters on Venus with the radar appearance of lunar craters. Observations of lunar craters at 3.8 cm show distinctive radar highlighting of crater rims. This kind of highlighting is not seen in the Arecibo Venus data but its absence is not unexpected; Goldstone radar observations at very low incidence angles indicate that the rim slopes of Venus craters (8°) are much smaller than those of

lunar craters (~25°). Unfortunately, no bright ring crater has yet been observed at low radar incidence angles, which might reveal a crater rim and show where that rim is located relative to the bright annulus.

The bright annular zone in the Venusian craters almost certainly corresponds to a local excess in surface roughness or blockiness. Bright annular radar features associated with craters are rare on the lunar surface. They are only seen in lunar craters whose floors have been embayed with mare materials. An example is shown in Fig. 1(b), the lunar crater, Plato, near 10°W, 53°N. Such lunar features exhibit radar bright central features, which also appear in some of the Venus images.

If the Venusian features formed in a similar way this would imply that almost all Venusian craters developed a fill of volcanic material soon after their formation. However, there are other interpretations for the dark interiors of the Venusian features. The distinctive form and evolution of most lunar crater signatures -- initially bright in floor and ejecta zone, shrinking comparatively rapidly to the crater rim, and gradually fading with further exposure -- is a consequence of the greater lifetime of the ejecta floor signature in comparison with the signature of the ejecta zone. If the floor materials in the Venusian craters either formed as a smooth surfaced deposit or if they evolved to this state more rapidly than the deposits around the crater (ejecta or

rough volcanic flows) then the radar signature would either initially be a bright annulus or would evolve rapidly to a bright annulus. It is also possible that crater interiors on Venus initially form with a cover of fine debris because the atmosphere prevents most of the ejecta from leaving the crater cavity (Settle, 1980).

Morphometric Comparisons with Lunar Radar Crater Haloes

In Fig. 4 we have compared the widths of the radar haloes around lunar impact craters with the widths of the bright annular zones of Venus craters. Our lunar measurements (Fig. 4a, b) at 3.8 cm and 70 cm wavelengths are referenced to the crater rim diameter as measured most accurately from photographs (see Thompson et al., 1981). At 3.8 cm wavelength, radar bright ejecta is up to 20 times the diameter of the crater around which it is formed, although for most craters the halo is smaller than this. At 70 cm wavelength the radar halo is more compact but the measurements still show considerable scatter.

The position of the crater rim relative to the bright halo in the Venus bright-ring features has not yet been observed. Consequently, in order to compare the Venusian and lunar features, we have to make assumptions about the position of the crater rim relative to the inner part of the bright annulus. In Fig. 4c we have assumed that the inner part of the bright annulus represents the rim-to-rim diameter of the crater. In Fig. 4d we have equated it to the width of the crater floor and estimated the crater rim width using a relationship developed by Pike (1977) for lunar craters.

Comparing the lunar and Venusian data on the width of radar bright deposits around craters present a number of difficulties. Resolution limits the Venus data to craters of large diameter (>20 km). Because the lifetime of the 3.8 cm radar signatures of lunar crater ejecta deposits is short on the Moon, few examples of large lunar craters with bright ejecta deposits appear in Fig. 4. Thus, only a few craters occur in the size range for which we have data on both bodies. Added to this is the uncertainty of the crater rim diameter in the Venus images and the fact that the Venus radar wavelength of 12.6 cm lies between the two wavelengths for which we have lunar observations. Thus, on the one hand, there is nothing in these data to preclude the possibility that the Venusian features are impact crater deposits formed under similar conditions to those in which lunar features formed. On the other hand, a broad range of other possibilities cannot be excluded. Let us review the various alternatives.

Campbell and Burns (1980) referred to the possibility that the Venus bright-ring features might be impact crater ejecta deposits ballistically emplaced early in the history of the Venus atmosphere when that atmosphere was so thin that it scarcely impeded the ballistic emplacement of ejecta. They examined the effect of increasing atmospheric densities on the range of a cubic projectile (100 m on a side) ejected at 0.5 km/sec and showed that its range was 30 km in the absence

of an atmosphere, 15 km in an earth-like atmosphere and only 10 km in the present Venus atmosphere. All of these ranges are far less than ejecta widths inferred in Fig. 4c and 4d.

Ballistic emplacement is probably irrelevant to the extent of ejecta deposits surrounding Venusian craters. On Mars, with far lower atmospheric pressures than Earth or Venus, the ejecta from many craters is deposited as flows (Carr et al., 1977), although the role of the atmosphere in forming these flows is not yet clear (Mouginis-Mark, 1981). When a dense fluid is loaded with a suspension of particulate material it is capable of traveling long distances on shallow slopes. Turbidity flows triggered by the excavation of impact craters at the base of the Venus atmosphere may resemble ocean density currents on the Earth's continental shelf (Florensky et al., 1977) and could transport material great distances.

Finally, the bright annular deposits may be volcanic deposits formed around volcano-tectonic depressions. Except for the most viscous lava flows, many lava flows are capable of flowing for these distances and it is possible, although not likely, that the long range flows on shallow slopes would develop rough radar scattering surfaces.

ANALYSIS OF POPULATIONS OF RADAR BRIGHT CRATERS ON MOON AND VENUS

In investigations of the populations of craters with radar bright crater floors and ejecta deposits Thompson et al. (1980, 1981) used data on photogeological crater abundances to establish lifetimes for floor and ejecta signatures. For Venus craters, the populations of craters with radar bright haloes have been measured (Campbell and Burns, 1980). Here we compare the populations of lunar and Venusian radar bright craters and attempt to define what type of crater population is being measured in the Arecibo radar images.

Impact crater populations on planetary surfaces lie somewhere between two extremes: production populations in which the number of craters continue to increase with time and is the total number formed since the surface was crated; and steady state populations in which a uniform erosional or depositional process or mutual obliteration destroys old craters as rapidly as new ones are formed. When different criteria are used for crater identification, the same surface may appear to have a production population using one method of crater identification and a steady state population according to another. There is nothing contradictory in this result, of course, and the resulting populations contain complementary information about different processes acting on planetary surfaces.

Volcanic crater populations on planetary surfaces are much less well understood. Investigations of terrestrial craters of explosive volcanic origin by Simpson (1966, 1967) indicated a non-uniform distribution of crater diameters with a surplus of small craters and a population curve similar to that observed for lunar and martian impact craters. Volcanic craters on Io have a similar population profile (Schaber 1980b) with an overall crater density somewhere between the impact crater population on the average lunar mare and that on heavily cratered lunar and planetary surfaces such as the lunar uplands. Our understanding of the mechanism of production of volcanic craters is presently poor and the concept of a production population analogous to that of impact craters is not too meaningful. However, on a mature volcanic surface such as Io the volcanic crater population may well be in a steady state established by crater obliteration mechanisms associated with the same basic processes that form craters. If the bright annular features on Io are a mixed population of volcanic and impact craters the factors influencing population density will be complex.

Lunar Crater Populations

Investigation of the surface of the lunar maria using image data suitable for revealing the topographic character of lunar impact craters -- circular depressions with raised rims -- indicates that the population of craters of diameter 1 km and larger occupies a small fraction of the surface. Craters of this size and larger

belong to a production population; at 100 m and below craters are more densely packed and mutual obliteration may have set up an equilibrium or steady state situation. On the lunar uplands, photogeological measurements reveal much denser populations at all sizes; whether these are nearer to steady state or production populations is still a subject of controversy (Woronow, 1978).

The 3.8 cm and 70 cm radar (and infrared signatures) of crater floors and ejecta deposits have finite lifetimes to exposure on the surface of the Moon. When the age of the surface exceeds that lifetime, so do some of the earlier formed craters on that surface and the population of craters with radar bright characteristics assumes the steady state form. The steady state population of craters with radar bright ejecta is compared with the crater population on Oceanus Procellarum in Fig. 5. Crater populations are expressed as relative densities (see Thompson et al., 1981).

Degradation by impacts of meteoritic particles which abrade and fracture rocks exposed at the surface, excavate other rocks from depth, and coat the regolith with mantles of fine ejecta appears to be a logical explanation for the aging of infrared and radar crater signatures. Precisely why crater floor deposits survive longer than ejecta deposits is unknown but a number of possible explanations have been advanced (Thompson et al., 1980).

In Fig. 6 the bright-ring crater population on Venus generated from a tabulation published by Campbell and Burns (1980) is compared with the number of impact craters predicted for 3.2

billion years exposure on the surface of Venus. In the diameter range of interest (>20 km) the Venus atmosphere has a negligible effect on the production of craters by impacting objects (Tauber and Kirk, 1976). For Fig. 6 we used a Venusian impact crater production rate developed by the Basaltic Volcanism Project (Hartmann et al., 1981). Inspection of Fig. 6 indicates that the observed Venus crater population is greatly deficient in small craters compared to the theoretical impact crater production population.

What could explain these deficiencies? Obviously if most of the Venusian craters are volcano-tectonic there is no reason to expect these populations to look alike, although Schaber (1980b) has reported some surprising similarities between impact crater production populations and volcanic crater populations. If the craters are primarily of impact origin then it is possible that resolution affects the observed population. Another explanation which we believe is worthy of consideration, based on the lunar experience, is that we are not seeing a production population of features but a steady state population. Such a situation could exist if the radar signatures of craters are being rapidly erased by a surface process. This effect which occurs on the Moon might affect both impact and volcanic crater signatures on a planet such as Venus.

billion years exposure on the surface of Venus. In the diameter range of interest (>20 km) the Venus atmosphere has a negligible effect on the production of craters by impacting objects (Tauber and Kirk, 1976). For Fig. 6 we used a Venusian impact crater production rate developed by the Planetary Basaltic Volcanism Project (1980). Inspection of Fig. 6 indicates that the observed Venus crater population is greatly deficient in small craters compared to the theoretical impact crater production population.

What could explain these deficiencies? Obviously if most of the Venusian craters are volcano-tectonic there is no reason to expect these populations to look alike, although Schaber (1980b) has reported some surprising similarities between impact crater production populations and volcanic crater populations. If the craters are primarily of impact origin then it is possible that resolution affects the observed population. However, in our view, the resolution effect would not be large enough to explain the differences. Another explanation which we believe is worthy of consideration, based on the lunar experience, is that we are not seeing a production population of features but a steady state population. Such a situation could exist if the radar signatures of craters are being rapidly erased by a surface process. This effect which occurs on the Moon might affect both impact and volcanic crater signatures on a planet such as Venus.

MECHANISM OF OBLITERATION OF CRATER RADAR SIGNATURES ON VENUS

What process could be responsible for the steady obliteration of radar crater signatures on Venus? Whereas meteoritic gardening is probably the major factor in degrading these signatures on the Moon, it is clearly ineffective on Venus where the thick atmosphere shields the surface from meteoritic bombardment. A continuing series of volcanic events or eolian processes cannot be ruled out. However, an interesting alternative possibility is that particles injected into the atmosphere by large cratering events precipitate from atmospheric suspension and progressively mask the blocky ejecta deposits that render Venus craters visible in the Arecibo radar image.

We have modeled the effects of this process on the Venus radar crater populations. We assumed in this exercise that all the bright ring craters were formed by impact, although the mechanism will work if only a fraction are impact related. Cratering events in the size range above 10 km were generated with a Monte Carlo simulation, modeling cratering as a Poisson process, with crater diameters determined by the cumulative distribution (Hartmann, 1977):

$$\text{Probability (Diameter} \geq D) = (D_{min}/D)^2 \qquad (1)$$

where D_{min} was taken to be 10 km. The material deposited

planetwide by each event was calculated and the crater diameter, time of formation of the crater and the thickness of deposition stored. After each cratering event, the thickness of the deposit on each crater already in the file was updated. The population of craters at the end of the experiment that was visible to radar was estimated using a variety of assumptions about the thickness of deposit needed to obscure a crater of a given diameter.

In Fig. 7 we illustrate the amount of deposition as a function of time for a single Monte Carlo model run. For each run the deposition history was calculated for two functional dependences between the volume of suspended material and crater diameter: D-squared scaling (Fig. 7a) and D-cubed scaling (Fig. 7b). In neither case is the deposition rate uniform, but for the D-cubed scaling the deviation is much more conspicuous because a few large events dominate the depositional history.

In Fig. 8 we contrast the observed population of radar craters on Venus with the total number of craters produced in each of three Monte Carlo runs ignoring any crater erasure process. The slopes of the observed populations and the Monte Carlo populations are evidently very different. This confirms our earlier conclusion that the bright ring crater population does not resemble an impact crater production population (Fig. 6).

In Fig. 9 we show the effects of erasure of the radar signature of craters by the global mantling process. The same three Monte Carlo simulations used to generate Fig. 8 formed the basis for the model results reproduced here. In Fig. 9a and 9b we have used D-squared scaling for the generation of suspended material; the simulations in Fig. 9a and 9b assume a low and high threshold thickness for obliterating craters respectively. In Fig. 9c and 9d we have used D-cubed scaling for the generation of suspended material; Figs. 9c and 9d assume low and high threshold thickness respectively. The low and high threshold thicknesses referred to here are illustrated in Fig. 10.

Examination of the simulation results in Fig. 9 indicates very clearly that a model with a threshold independent of diameter cannot match the observed population of bright-ring radar craters over the entire diameter range greater than 16 km. However, excluding craters smaller than 64 km from the comparison, which is reasonable given the limited resolution of the radar data (Campbell and Burns, 1980), the first of the three Monte Carlo simulations bears a fair resemblance to the observed data for low threshold thicknesses (Fig. 9a and 9c). (The other two Monte Carlo runs bear no such close resemblance -- a consequence of the statistics of very small numbers.) We conclude that the measured populations of bright ring features larger than 64 km is not inconsistent with a crater obliteration model in which the threshold is independent of diameter.

Let us now suppose that the observed crater distribution shown in Fig. 6, 8 and 9 were valid for crater diameters down to 32 km. None of the model results of Fig. 9 with a threshold independent of diameter gives an acceptable match in this case. What does this imply about the diameter dependence of the deposition threshold thickness? We have developed a model to find the answer. First, a power law was least squares fit to the relative crater densities of bright ring features including all bright ring features with "crater" diameters larger than 32 km.

Using the best fit power function, we have determined a deposition threshold relationship:

$$T_D/T = (D/400)^{1.67} \qquad (2)$$

where T_D = thickness of deposit to remove a crater diameter D, and T = total deposit thickness from all cratering events. For a crater production function conforming to the inverse diameter squared law and any crater sedimentation law, the steady state population computed with this threshold law is identical to the best fit curve. The derivation of equation (2) is described in the Appendix and T_D is plotted as a function of crater diameter in Fig. 10.

Using the three Monte Carlo crater populations of Fig. 8 we have generated simulated radar bright-ring feature populations using the diameter dependent deposition threshold relationship of equation (2) and Fig. 10. As expected, the

general shape of the simulated populations (Fig. 11) is similar to the observed data. However, there are considerable differences between two Monte Carlo runs conducted with the same statistical parameters and only two of the runs give a satisfactory visual match with the measured densities above 32 km diameter. Least squares analysis of these data also show that deviations from the linear relationship on the log-log plot far exceed the estimated errors in the individual observations. This is simply a consequence of the large deviations between the actual rate of deposition of crater ejecta material (Fig. 7) and the uniform rate which is assumed in the analytical solution given in the Appendix.

In summary, this analysis shows that if the measured population is only valid for crater diameters larger than 64 km then a global mantling mechanism with a fixed threshold deposition thickness independent of diameter can match the observations. If, on the other hand, the crater density data are good for diameters larger than 32 km, the fixed deposition threshold doesn't work. However, a diameter-dependent threshold deposition thickness can be chosen which provides a satisfactory match with the crater population larger than 32 km.

DISCUSSION

Among the issues raised by our hypothesis are: (1) Can large impacts raise enough material to obliterate radar signatures of craters? (2) Is it plausible for the deposition threshold thickness for radar crater obliteration to be diameter dependent? (3) What independent tests exist to choose between this and other hypothesis for the origin of Venusian bright ring features?

Are the ejecta deposits thick enough to mask radar signatures?

A basic issue in these calculations is whether an impact cratering event can inject enough material into suspension to mask the radar signatures of craters on Venus. This issue can be broken into two parts: what thickness of material is needed to mask the crater radar signature and what thickness could plausibly be generated by impact of a bolide?

The thickness of material needed to obliterate a crater-related radar signature is determined in part by the character of the block populations and roughness effects that give rise to that signature. Blocky materials around fresh lunar impact craters that produced bright 3.8 cm haloes are dominated by centimeter-sized blocks (Thompson et al., 1981). Blocks at the VL-2 landing site on Mars, which are believed to be primarily ejecta from Mie crater, are scarce in large cobbles (rocks > 128 mm in diameter) according to Garvin et al. (1981).

These block populations display some of the effects of either exposure to the lunar micrometeorite flux or weathering in the martian environment and so we cannot assume that they would be representative of the blocks around a freshly-formed Venusian crater. However, arguments have been made by Schultz and Mendell (1978) that fragments in the ejecta deposits of large craters are comminuted such that few very large fragments survive. If the Venusian ring-shaped craters are primarily volcanic then these surfaces may contain much larger blocks and convoluted roughness elements.

As a block deposit is progressively covered by dry non-conducting mantling materials the decrease in the scattered radar signal takes place in two distinct phases. In the first phase which extends up to the point where the blocks are covered by the mantle the scattered signal from the blocks is reduced by two effects: interception of radiation by the specular reflection at the mantle/atmosphere interface and reduction of the contrast in dielectric constant between the blocks and their environment. The denser the mantle materials then the larger the reduction in scattered radiation. As the mantle thickens further there is a second phase of signal reduction which depends on the amount of absorption in the mantle materials. For high absorption the scattering continues to decline rapidly; for low absorption the decline is much less pronounced.

Observations of the effect of mantling of rough terrestrial rock deposits (generally pahoehoe and aa lavas) by sand and loess suggest that only a thin veneer of sediment can obliterate the radar roughness signature (Elachi et al., 1979; Dellwig, 1969). In this case, small amounts of moisture in the mantle increase the dielectric constant and radar absorption and so these results are not directly applicable to Venus. However, Cannon (1979) reports that a 1.1 m thick cover of dry snow had little effect on the radar signature of a lava flow in Northern Alaska. We suspect that very significant attenuation of the 12.6 cm radar signal from a rough Venusian surface occurs with a few tens of centimeters of sedimentary cover. However, theoretical simulations would be desirable to confirm this.

At present there are no theoretical models to predict the thickness of the layer of material laid down by a large impact crater on Venus. Consequently, we must appeal to observational and theoretical data concerning the effects of large impact on the Earth's surface. The recent discovery of a 1 to 150 cm clay layer of global extent demarking the Cretaceous-Tertiary (C-T) boundary (65 Ma) on the Earth which is enriched in certain noble metals by factors of 5 to 100 relative to the Earth's crust (Alvarez et al., 1980) has some bearing on this issue. Alvarez et al. have proposed that

the impact of a 10 km diameter bolide lofted meteoritic material to great heights in the atmosphere from where it was dispersed around the globe. Up to 21% of the material in the clay layer appears to be of meteoritic origin.

At present it is not clear what fraction of the material in the C-T boundary clay layer is derived from excavation of the crater and what part is of local origin. O'Keefe and Ahrens (1981) have analyzed the impact mechanics of the hypothesized C-T extinction bolide. They find that in the ejecta thrown up to the greatest heights, meteoritic material is dominant. They also find that for a dense impacting body somewhere between 10 and 100 times the mass of the impacting bolide is lofting to altitudes of above 10 km where it implants 10-30% of the original impact energy in atmospheric heating. Upon deposition this material would form a layer between 2 and 20 cm thick.

In the Venus model we are considering even larger events than the C-T extinction bolide. Events producing craters as large as 300 km are implied because the age of this event is up to 20 times larger than the C-T extinction bolide. Depositional layer thicknesses would be correspondingly greater. However, a rigorous analysis of the effects of a large impact on Venus and the transport of ejecta into the Venus atmosphere is needed to verify these tentative conclusions.

Although global deposition appears adequate to account for the obliteration of crater radar signatures, the regional effects of sedimentation from large impacts may be important. Ejecta flows on Mars extending many crater diameters from large craters transported thick deposits of material in ground-hugging flows. On Mars and on Venus there may also have been extensive deposits of material dispersed as somewhat thinner layers over much broader areas perhaps in autosuspended form (Florenski et al., 1977) with sufficient thickness to obliterate the radar signatures of earlier formed crater ejecta deposits. The resulting steady-state radar crater population would reflect regional and global depositional processes.

Is a diameter dependent deposition threshold thickness plausible?

Our analysis of the observed population of radar bright ring-shaped features on Venus has yielded conclusions that are very sensitive to the assumed spatial resolution of the radar imagery. If we assume that only measurements of bright ring craters larger than 64 km are good then we can satisfactorily account for the observations with a deposition model in which threshold deposit thickness is independent of crater diameter. However, assuming that the data are good down to a diameter of 32 km the situation changes radically. In this case a threshold deposit thickness with a very dramatic diameter dependence is implied (Fig. 10).

This relationship of Fig. 10 is difficult to reconcile with the physical origin of these radar bright signature results. The deposition threshold thickness is primarily controlled by the character of surface roughness and blockiness in the vicinity of the crater. There is no obvious reason why the thickness of material needed to obscure the radar signature from blocks in the deposit around a large crater should be more than an order of magnitude larger than around a small crater. Blocks in the extended ejecta deposits around large impact craters are expected to be fragmented by the impact event (Schultz and Mendell, 1978) and similar in size to blocks around smaller craters. Surface roughness at the scale affecting the radar return would be equally affected by deposition for small and large impact craters. Similar arguments would apply for deposits around volcanic craters.

Clearly, improved measurements of radar bright ring features with interior diameters of a few tens of kilometers hold the key to resolving this problem. Improvements in the understanding of the resolution effects in the existing data could also help. Plans to acquire data at low radar incidence angles from the Goldstone facility (Jurgens, private communication, 1981) are also relevant here because they could provide definitive rim diameters from some bright ring shaped features and identify craters from features within radar bright spots which have not been resolved into bright rings.

If the population of bright ring craters falls as rapidly below 64 km diameter as the data presented here would suggest then we do not feel that the obliteration mechanism alone could account for this. It might imply that the bright-ring features are a form of impact or volcanic crater deposit unique to the crater size range greater than 64 km.

Are there other observational data which bear on alternative hypothesis?

Alternative interpretations of the Venusian bright ring craters as impact craters or volcano-tectonic craters have different implications for the lithology of the terrain surfaces on Venus. The impact cratering model discussed here implies that the rolling plains and lowland areas on which the vast majority of these craters formed are mantled with fine fragmental debris. The volcano-tectonic model suggests that these terrains may be formed of young lavas. Can Venera in situ data or the radar remote sensing data help us decide which type of surface is more likely?

Landed imaging observations have been made near the highland region of Beta Regio by Venera 9 ($290^{\circ}50'$, $31^{\circ}42'$) and Venera 10 (291°, $16^{\circ}02'$). Locations given are nominal landing locations and it is not clear by how much the actual landing sites differ from features seen in the radar images because of cartographic and targetting uncertainties (Masursky, private communication). Both Venera 9 and 10 show abundant slab-like boulders and rocky outcrops but little indication of sedimentary

cover. Of more relevance here are the observations from Venera 8 (327^{o}, -10^{o}) which landed on either rolling plains or lowlands. Unfortunately the observations made by Venera 8 are very incomplete. There are no imaging observations and the density measurements of 1.5 gm/cm^3 reported by Vinogradov et al. (1974) bear no error bounds. Although these measurements look favorable to the hypothesis presented here, the more recent attempts to measure density by Venera 9 and 10 with a gamma ray scatterometer provide cause for scepticism about the Venera 8 result (Surkov, 1977b). A very significant chemical difference between the surface at Venera 8 and the surfaces at Veneras 9 and 10 has been reported by Surkov et al. (1977b). Conceivably this could arise from a sedimentary deposit although other possibilities cannot be excluded.

The radar reflectivity of the Venus surface also contains information about dielectric constant and bulk density pertinent to surface properties of Venus. Jurgens and Dyce (1970) reported an average integrated radar cross section of 0.15 measured at 70 cm which may imply an average radar reflectivity of between 12-15% according to Jurgens (private communication, 1981). For comparison, data acquired by Dyce et al. (1967) at 70 cm wavelength for Mars have integrated cross sections varying from 0.03 to 0.13 times the geometrical cross section with an average value of 0.07. High cross sections and reflectivities like those of Venus generally imply high density material. Does this imply that the average density of the Venus surface is quite high and much more in line with a

compact rocky material than with a loosely consolidated sediment?

Not necessarily so. Jakosky and Muhleman (1981) in their recent investigation of radar reflectivity and thermal inertia properties of Mars conclude that rocks buried in a sedimentary type deposit can enhance the apparent reflectivity of a geological surface. Florensky et al. (1977) have also discussed the possibility that sediments could be lithified and even "surface metamorphosed" at the base of the Venusian atmosphere. Surkov et al. (1977b) do not believe that the radar data constrain surface densities very well and cite large uncertainties of 1 to 43 gm/cm^{-3} in the radar-derived measurement. Thus, it seems to us that given the present data, the thin debris mantle models and the pristine volcanic models of the Venusian rolling plains and lowlands are both permitted by the 70 cm cross section data. We await with interest the reduction of the 12.6 cm reflectivity data from the Pioneer Venus orbiter (Masursky et al., 1980) which might help to resolve the issue.

Another type of radar data pertinent to this problem is information about surface roughness. The average small scale roughness on Venus is only a third of what it is on the lunar maria (α = 0.05 vs. 0.15) according to Jurgens and Dyce (1970). They suggested that the average Venusian surface is free of blocks and possessed shallow slopes. Pioneer Venus maps of average slope (Hagfors C-factor) and the imaging data which responds to small scale roughness and blockiness, both indicate low values in the Venusian lowland and midland regions. Such a condition is certainly brought about by the deposition of a

debris mantle. However, volcanic plains surfaces formed in the Venusian environment may also be smooth and relatively block free. The roughness of the lunar maria is due in large part to cratering by smaller craters which would not be as significant on Venus because of atmospheric screening.

Radar observations of terrestrial volcanic deposits (Elachi et al., 1980) indicate smooth pahoehoe flows exhibit much less scattering at high radar illumination angles than do blocky aa flows. However, weathering and mantling flows with increasing exposure on the surface is the major factor reducing radar roughness. Deposits of volcanic ash may be important in some instances. Radar roughness data do not provide a definitive answer to the geology of the Venus lowlands.

We should not rule out the possibility that deposits around Venusian craters weather in situ. Although not directly applicable to conditions in the Venusian lowlands the imaging observations by Venera 9 and 10 on the margins of the Beta feature (Rhea Mons and Theia Mons) have some relevance here. Florensky et al. (1977) describe surfaces at these two sites consisting of slab-like boulders set in a fine grained dark matrix (Venera 9) and a plain composed of scattered slab-like outcrops separated by a fine grained dark matrix (Venera 10). They report evidence for down slope transport of slabs on the 20^{o} slope at the Venera 9 site and in situ rounding and smoothing of the large slab-like deposits at both sites. They attribute the in situ weathering to eolian ablation or chemical action.

One's impression from the Venera 9 and 10 images is that the in situ weathering process has not proceeded very far.

However, lacking information on the age of this surface (being close to Beta it may be very young), it is impossible to infer the degree of weathering around crater deposits on other terrains.

Comparisons with Mars

Our view of the role of sedimentary processes on Venus makes for some interesting comparisons with Mars. There are at least two differences between these planets which influences their sedimentary environments. Mars has much greater overall relief and a trimodal distribution of surface elevations whereas Venus elevations are unimodal. More significantly the surface atmospheric pressures on the two planets differ by a factor of 10^4.

The present view of Mars is that eolian sedimentation accounts for most of the superficial geological characteristics that are manifested in thermal inertia and radar properties (Schaber, 1980a). These properties are uncorrelated with the major global dichotomy of terrain type ancient cratered terrain vs. younger plains, have no simple relationship to latitude, and are not controlled in any simple fashion by elevation or slope.

The situation of Venus may be much simpler. There appears to be a correlation between elevation and surface roughness (Pettengill et al., 1981) which would be interpreted as the preferential sedimentary mantling of basins relative to high-standing terrains. Lakshmi Planum, which is a plateau

of low reflectivity, appears to be an exception. Possibly, slope is the more critical factor controlling radar roughness on Venus. Steep slopes may be radar rough for a number of reasons: they do not retain sediment effectively, they generate talus, and they may be an expression of the blocky deposits associated with central volcanic features. The interpretations of conditions at the Venera 9 and 10 sites by Florensky et al. (1977) provide support for all three possibilities.

Implications for future Venus missions

Given the major uncertainties about the nature of bright ring features and craters on Venus in general, new radar data from Earth-based and spacecraft missions are needed. In order to identify the topographic expression of the very shallow craters that may be associated with the bright ring features, imagery at very low radar illumination angles is highly desirable. This is impossible to acquire from the Earth except for a very few features close to the Venus equator. It may also be impractical to provide such data with the projected Venus Orbiting Imaging Radar (VOIR) mission. Radar observation at low illumination angles in terrain of moderate relief can be difficult to interpret and in some areas of high relief contain layover artifacts. Accordingly, the nominal incidence angle of $\sim 50^{\circ}$ has been selected for the VOIR mission (Saunders et al., 1980). Recent research by Blom and Elachi (1981) has shown that it is not possible to identify sand dunes with this

illumination geometry in L-band imagery whereas the SEASAT incidence angles of approximately 20° provides excellent discrimination and imaging of eolian features. We consider that the slopes of the shallow rims of Venusian craters may also be unrecognizable in VOIR images unless these slopes have very different scattering properties than their surrounds (Thompson, 1981).

This work also has implications for future Venus landers. Imaging observations from a lander on the rolling plains or lowlands could determine whether the mechanism of crater obliteration proposed here is invalid. Future Soviet landers may be targetted for the Venusian lowlands (Masursky, private communication, 1981). Discovery of a surface of fine sedimentary material at those sites would strongly support the thesis developed in this paper.

CONCLUDING REMARKS

The bright ring-shaped features seen in Arecibo radar images appear to be radar rough areas around craters of impact or volcanic origin. The lifetime of these radar bright signatures on the surface of Venus will be limited by mantling by sedimentary material globally deposited after very large impact events. This may explain why the population of these features is small and possibly deficient in small craters when compared to the populations of impact and volcanic craters identified visually on other planetary surfaces.

A model of obliteration of the radar signatures of a population of impact craters by this process yields somewhat different predictions depending upon the assumed minimum crater diameter for reliable recognition of bright ring features. If we assume only ring features with interior diameters larger than 64 km are reliably detected, we can account for the observed population with a mantling process in which the thickness of material needed to obliterate crater radar signatures is independent of crater diameter. However, if the population measurement for craters down to 32 km are considered valid then the radar signatures of smaller craters must be removed much more rapidly than those of larger craters. This appears to be unreasonable for the mechanism considered here.

There are other explanations for the observations discussed here. The bright ejecta craters may be a unique population of volcanic or impact craters which are initially deficient in craters of sizes smaller than 64 km. However, we cannot exclude the possibility that the ejecta blankets formed around smaller impact craters on Venus are initially deficient in blocks and surface roughness, that blocks rapidly weather in the Venus environment, or that resurfacing by recent volcanic activity in the Venus lowlands obliterates crater radar signature. Some of these possibilities could be better constrained by lander imaging observations in the Venusian lowlands.

Further study of bright ring features on Venus requires much improved definition of their topographic relief. This can be obtained with radar imaging at low radar incidence angles. However, Earth-based observations under these conditions are limited to low Venus latitudes and spacecraft radar imaging observations with the projected VOIR mission will only be acquired at comparatively high incidence angles (~50^{o}). Topographic mapping using ground-based interferometry techniques and radar altimetry from VOIR may provide an alternative approach to defining the relief across these features.

APPENDIX -- DERIVATION OF THRESHOLD DEPOSITION THICKNESS RELATION

Suppose N_o craters to have formed in an area A according to a $1/D^2$ cumulative distribution relationship:

$$\Pr\{\text{diameter} \geq D\} = (D_{min}/D)^2 \quad (D \geq D_{min}) \qquad A(1)$$

If all these craters are visible and are grouped into diameter bins whose boundaries are successive powers of some number ρ, e.g., 2, then the expected number (N(D)) of craters in a bin of mean diameter D is:

$$N(D) = N_o\,((\rho^2 - 1)/\rho)\,(D_{min}/D)^2 \qquad A(2)$$

In this case, the expected value of the relative crater density R (defined as

$$R = (\rho^{\frac{1}{2}}\, N(D)\, D^2)/((\rho - 1)A) \qquad A(3)$$

is independent of diameter:

$$R_o = N_o \quad (\rho + 1)\, \rho^{-\frac{1}{2}}\, D^2_{min}/A \qquad A(4)$$

We wish to find a function t(D), where t(D) is the minimum thickness of material which must be deposited to obscure a crater of diameter D, such that the observed relationship between R and D is

$$\log R = \alpha \log D + \beta \qquad A(5)$$

At some large diameter (D_{max}) no craters are obliterated and $R(D_{max})$ must equal R_o from Equation (A4). Choosing β in Eqn. A5 accordihgly, we may express R as

$$R = R_o (D/D_{max})^{\alpha} \qquad A(6)$$

This expression can be equated to the relationship for the relative density (Equation (A3)in order to determine the number of craters (N'(D)) in a bin of average diameter D in the observed population.

$$R_o(D/D_{max})^{\alpha} = (\rho^{\frac{1}{2}} N'(D) D^2)/((\rho - 1)A) \qquad A(7)$$

which yields

$$N'(D) = (\rho - 1)\rho^{-\frac{1}{2}} A \cdot R_o \cdot D^{\alpha-1}/D^{\alpha}_{max} \qquad A(8)$$

f the rate of deposition on the surface has been uniform then

$$N'(D) = N(D) \cdot t(D)/T \qquad A(9)$$

where T is the total thickness of material deposited during the cratering history of the area. Combining expressions A(8) and (9)' we get

$$t(D) = T(D/D_{max})^{\alpha} \qquad A(10)$$

For the features with diameter greater than 32km used in this study, a least squares fit yielded $\alpha = 1.67 \pm .43$. D_{max} was taken to be 400km, since the fitted curve attains the estimated value of R_o at this diameter. Thus, the threshold relation becomes

$$t(D) = T(D/400)^{1.67} \qquad A(11)$$

ACKNOWLEDGEMENTS

We would like to thank Dr. Stan Zisk for permission to use the 3.8 cm radar data and Dr. Donald Campbell for providing original prints of some of the Arecibo images reproduced here. Professor Tom Ahrens and Dr. Ray Jurgens also provided helpful information on the dynamics of large impacts and the radar properties of the Venus surface respectively. We also acknowledge the assistance of three anonymous reviewers for their constructive comments. This work was supported by the Solar Exploration Division of the National Aeronautics and Space Administration, Planetary Division under contract NASW 3383.

REFERENCES

Alvarez, L.W., W. Alvarez, F. Asaro, and H.V. Michel (1980). Extraterrestrial cause for the Cretaceous-Tertiary Extinction. Science 208, 1095-1108.

Blom, R., and C. Elachi (1981). Spaceborne and Airborne Imaging Radar Observations of Sand Dunes. J. Geophys. Res. 84, 3061-3073.

Campbell, P.J. (1979). Applications of radar imagery to Arctic and Subarctic Problems. Radar Geology: An Assessment Report of the Radar Geology Workshop, Snowmass, Colorado, JPL Publication 80-61, 265-274.

Carr, M.H., L.S. Crumpler, J.A. Cutts, R. Greeley, J.E. Guest, and H. Masursky (1977). Martian Impact Craters and Emplacement of Ejecta Surface Flow. J. Geophys. Res. 82, 4055-4066.

Chapman, C.R., and K.L. Jones (1977). Cratering and Obliteration History of Mars. Ann. Rev. Earth Planet. Sci. 3, 515-540.

Dellwig, L.F. (1969). An Evaluation of Multifrequency Radar Imagery of the Pisgah Crater Area. California Modern Geology 1, 65-73.

Dunham, D., and H.A. Spetzler (1980). Reconciling Venusian Topography and the Ar^{40} Anomaly. Lunar and Planetary Science Conference XI (abstracts), 244-246.

Dyce, R.B., G.H. Pettengill, and A.D. Sanchez (1967). Radar Observations of Mars and Jupiter at 70cm. Astron. J. 72, 771-777.

Elachi, C., R. Blom- M. Daily, T. Farr, and R.S. Saunders (1980). Radar Imaging of Volcanic Fields and Sand Dune Fields: Implications for VOIR. Radar Geology: An Assessment Report of the Radar Geology Workshop, Snowmass, Colorado, JPL Publication 80-61, 114-150.

Florensky, C.P., L.B. Ronca, A.T. Basilevsky, G.A. Burba, O.V. Nikolaeva, A.A. Pronn, A.M. Trakhtman, V.P. Volkov, and V.V. Zazetsky (1977). The Surface of Venus as Revealed by Soviet Venera 9 and 10. Geol. Soc. Am. Bull. 88, 1537-1545.

Garvin, J.B., P.J. Mouginis-Mark, and J.W. Head (1981). Characterization of Rock Populations on Planetary Surfaces: Techniques and a preliminary analysis of Mars and Venus. The Moon and the Planets 24, 355-369.

Hartmann, W.K. (1977). Relative Crater Production Rates on Planets. Icarus 31, 260-276.

Hartmann, W.K., et al. (1981). Basaltic Volcanism on the Terrestrial Planets. Pergamon Press, New York (in press).

Jakosky, B.M., and D.O. Muhleman (1981). A Comparison of the Thermal and Radar Characteristics of Mars. Icarus 45, 25-38.

Jurgens, R.F., and R.B. Dyce (1970). Radar Backscattering Properties of Venus at 70cm Wavelength. Astron. J. 75, 297-314.

Jurgens, R.F., R.M. Goldstein, H.R. Rumsey, and R.R. Green (1980). Images of Venus by Three-Station Radar Interferometry--1977 Results. J. Geophys. Res. 85, 8282-8294.

Masursky, H., E. Eliason, P.G. Ford, G.E. McGill, G.H. Pettengill, G.G. Schaber, and G. Schubert (1980). Pioneer Venus Radar Results: Geology from Images and Altimetry. J. Geophys. Res. 85, 8232-8260.

Mouginis-Mark, P. (1981). Ejecta Emplacement and Modes of Formation of Martian Fluidized Ejecta Craters. Icarus 45, 60-76.

O'Keefe, J.D., and T.J. Ahrens (1981). Impact Mechanics of the Cretaceous-Tertiary Extinction Bolide. Lunar Plan. Sci. Conf. XII (abstracts), 785-787.

Pettengill, G.H., D.B. Campbell, and H. Masursky (1980a). The Surface of Venus. Scientific American 243, 54-65.

Pettengill, G.H., E. Eliason, P.G. Ford, G.B. Loriot, H. Masursky, and G.E. McGill (1980b). Pioneer Venus Radar Results: Altimetry and Surface Properties. J. Geophys. Res. 85, 8261-8270.

Phillips, R.J., W.M. Kaula, G.E. McGill, and M.C. Malin (1981). Tectonics and Evolution of Venus. Science 212, 879-887.

Pike, R.J. (1977). Size-Dependence in the Shape of Fresh Impact Craters on the Moon. In Impact and Explosion Cratering (D.J. Roddy, R.O. Pepin, and R.B. Merrill, Eds.) pp. 489-509. Pergamon Press, New York.

Rumsey, H.C., G.A. Morris, R.B. Green, and R.M. Goldstein (1974). A Radar Brightness and Altitude Profile of a Portion of Venus. Icarus 23, 1-7.

Saunders, R.S., and M.C. Malin (1976). Venus Geological Analysis of Radar Images. Geol. Romana 15, 507-515.

Saunders, R.S., J.C. Holtzman, and C. Elachi (1980). Simulation of Orbital Radar Images. Radar Geology: An Assessment Report of the Radar Geology Workshop, Snowmass, Colorado, JPL Publication 80-61, 45-63.

Schaber, G.G. (1980a). Radar, Visual and Thermal Characteristics of Mars: Rough Planar Surfaces. Icarus 47, 159-184.

Schaber, G.G. (1980b). The Surface of Io: Geologic Units, Morphology and Tectonics. Icarus 43, 302-333.

Schultz, P.H., and W. Mendell (1978). Orbital Infrared Observations of Lunar Craters and Possible Implications for Impact Ejecta Emplacement. Proc. Lunar Sci. Conf. 9th, 2857-2883.

Settle, M. (1980). The Role of Fallback Ejecta in the Modification of Impact Craters. Icarus 42, 1-19.

Simpson, J.F. (1966). Additional Evidence for the Volcanic Origin of Lunar and Martian Craters. Earth Plan. Sci. Lett. 1, 132-134.

Simpson, J.F. (1967). The Frequency Distribution of Volcanic Crater Diameters. Bull. Volcanologique 30, 335-336.

Surkov, Y.A., F.F. Kirnozov, V.N. Glazov, and G.Z. Fedoseyev (1977a). Investigations of Venusian Gamma-Radiation by Venera 9 and Venera 10. COSPAR Space Res. 17, 659-662.

Surkov, Y.A., F.F. Kirnozov, V.K. Khristianov, B.N. Glazov, F. Ivano, and B.N. Korchuganov (1977b). Investigations of the Density of the Venusian Surface Rocks by Venera 10. COSPAR Space Res. 17, 651-657.

Tauber, M.E., and D.B. Kirk (1976). Impact Craters on Venus. Icarus 28, 351-357.

Thompson, T.W. (1981). Observations of Craters and Other Features with Shallow Slopes on Venus. (Manuscript in preparation.)

Thompson, T.W., J.A. Cutts, R.W. Shorthill, and S.H. Zisk (1980). Infrared and Radar Signatures of Lunar Craters: Implications about Crater Evolution. Proc. Conf. Lunar Highlands Crust, 483-499.

Thompson, T.W., S.H. Zisk, R.W. Shorthill, P.H. Schultz, and J.A. Cutts (1981). Lunar Craters with Radar Bright Ejecta. Icarus 41 (in press).

Vinogradov, A.P., Y.A. Surkov, and F.F. Kirnozov (1973). The Content of Uranium, Thorium and Potassium in the Rocks of Venus as Measured by Venera 8. Icarus 20, 253-259.

Woronow, A. (1978). A General Cratering-History Model and its Implications for the Lunar Highlands. Icarus 34, 76-88.

FIGURE CAPTIONS

Figure 1 (a) Arecibo 12.5 cm radar image of three Venusian ring-shaped features located near longitude 340° and latitude -27°. The largest and smallest features have interior diameters of about 100 km and 60 km, respectively.

(b) 70 cm depolarized radar map of lunar crater Plato (100.0 km diam.) and its environs. Plato's floor has been flooded by mare. Compare this feature with the Venusian features seen in 1(a).

Figure 2 (a) Lunar craters with 3.8 cm radar bright ejecta deposits: Mare Serenitatis, Mare Tranquillitatis, and adjoining terra.

(b) Low sun photograph of the same area. Craters with large radar bright haloes are identified with circles with the diameter of the halo.

Figure 3 (a) Distribution of craters with 3.8 cm radar bright ejecta on the moon.

(b) Distribution of features with radar bright annular features and dark circular features on Venus.

Figure 4 Scatter diagrams of radar halo diameters versus crater diameters for Lunar and Venusian craters. Lunar craters (a and b) were observed at 3.8 cm and 70 cm wavelengths. Only craters with 3.8 cm haloes plotting near or above the solid line

(Figure 4 - cont'd.)

(diameter greater than 20 km or twice crater diameter) were included in the compilation for reasons discussed by Thompson et al. (1980). This emphasized young craters with diameters between 1 and 10 kilometers, where 70 cm haloes are smaller than the 3.8 cm haloes (see Thompson et al. 1981). Venus crater diameters in (d) are published values, while (c) shows modified crater diameters assuming the dark central areas in the Venus radar images corresponds to a floor width similar to those observed in lunar craters (Pike 1977).

Figure 5 Comparison of population of 3.8 cm radar bright craters on the moon with the visual crater population for Oceanus Procellarum (for more details see Thompson et al., 1981). The relative crater density is defined as: $R=(\bar{D})^3 N/A(D_{max}-D_{min})$, where $\bar{D}$ is the geometric mean of crater diameters, N is the number of craters, A is the area, and D_{max} and D_{min} are the maximum and minimum crater diameters in a size bin. A crater population which has a cumulative distribution proportional to (crater diameter)$^{-2}$ and a differential distribution proportional to (crater diameter)$^{-3}$ plots as a horizontal line in a log(R) versus log(D) plot. Similarly, a crater population proportional to (crater diameter)$^{-3}$ and a differential population proportional to (crater diameter)$^{-4}$ has a

(Figure 5 - cont'd.)

slope of (-1) in a log(R) and log(D) plot.

Figure 6 Actual population of bright annular features on Venus compared with the predicted crater density for a 3.2 billion year old surface (range of possible values according to Hartmann et al., 1981). The crater age based on the population of the largest features here (diam. > 100 km) would be about 1.5 By (cf. Phillips et al., 1981, who obtain 1.7±1.0 billion years also using the crater production rates of Hartmann et al., 1981). The age of 600 million years reported by Campbell and Burns (1980) is based on the same crater densities but uses the crater production rates of Hartmann (1977).

Figure 7 Deposition of material as a function of time for material thrown into suspension by large impact events calculated with a Monte Carlo model. The crater population responsible for both models is reproduced in Fig. 8. The horizontal scale is linear with time from the start to the end of the Monte Carlo experiment. The vertical scale is arbitrary and depends upon the precise choice of constants as described in the text.

Figure 8 Comparison of the population of bright ring features on Venus with the crater population generated in three Monte Carlo simulations. In none of these cases does the slope of the theoretical population resemble the slope of the observed population and there is an enormous excess of small craters in the theoretical curves. The first of the three theoretical curves was used to generate the deposition-time plots appearing in Fig. 7.

Figure 9 Comparison of the population of bright ring features on Venus with the results of Monte Carlo model simulating the obliteration of radar signatures by global deposition from large cratering events. In each of the four examples illustrated here the observed data appears in the top curve and the results of applying the three Monte Carlo-generated populations of Fig. 8 appear below. In all cases the threshold simulated with thickness for obliterating crater signatures is taken to be independent of crater diameter. In (a) and (b) we assume sedimentation is proportional to crater diameter squared; in (c) and (d) to crater diameter cubed. In (a) and (c) we assume that one unit thickness of material (see Fig. 7) is sufficient to obliterate the radar signature from a crater; in (b) and (d) we assume that seven units are necessary. In none of the four cases do we duplicate the high slope

(Figure 9 - cont'd.)

of the observed population of bright ring features over the entire range of crater diameters. However, the first of the Monte Carlo simulations in (a) and (c) does match the observed data for diameters greater than 64 km.

Figure 10 Comparison of the low (1 unit) and high (7 unit) threshold thicknesses used in the Monte Carlo simulations of Fig. 9 with a variable threshold thickness optimized to match the diameter frequency distributions of bright ring shaped features on Venus in the diameter range larger than 32 km.

Figure 11 Comparison of the observed population of bright ring shaped features on Venus with a Monte Carlo simulation of the obliteration of radar signatures by global deposition. In contrast with Fig. 9 we have used the variable threshold of Fig. 10 instead of fixed thresholds. In (a) we assume sedimentation is proportional to crater diameter squared; in (c) to crater diameter cubed. The three theoretical curves bottom correspond to the same three Monte Carlo populations used in Fig. 9 and reproduced in Fig. 6. Only one or two of the Monte Carlo distributions actually fit the observed data satisfactorily for the diameter range larger than 32 km. This is because the acutal deposition rate due to random impacts is only uniform in the statistical limit (see Fig. 7).

(a)

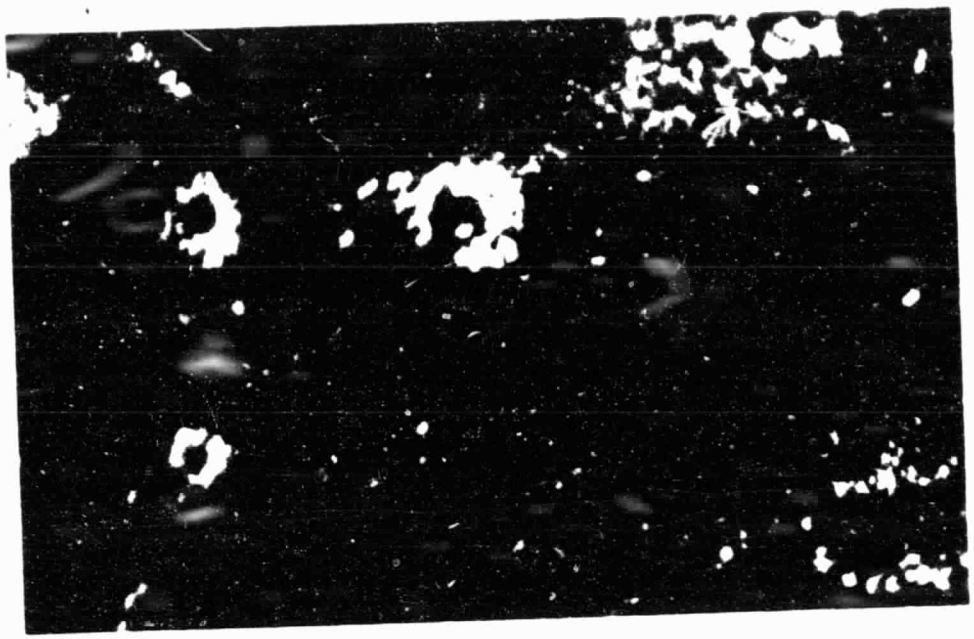

(b)

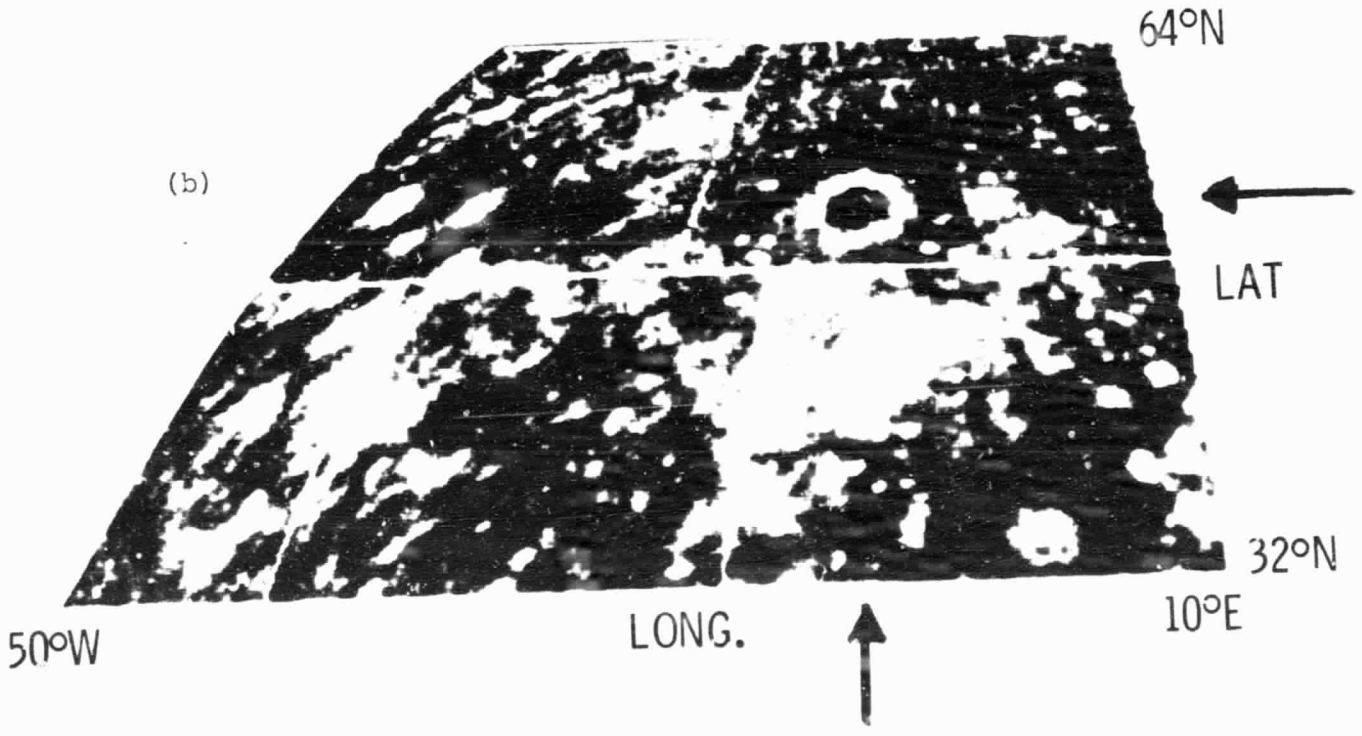

FIGURE 1

(a)

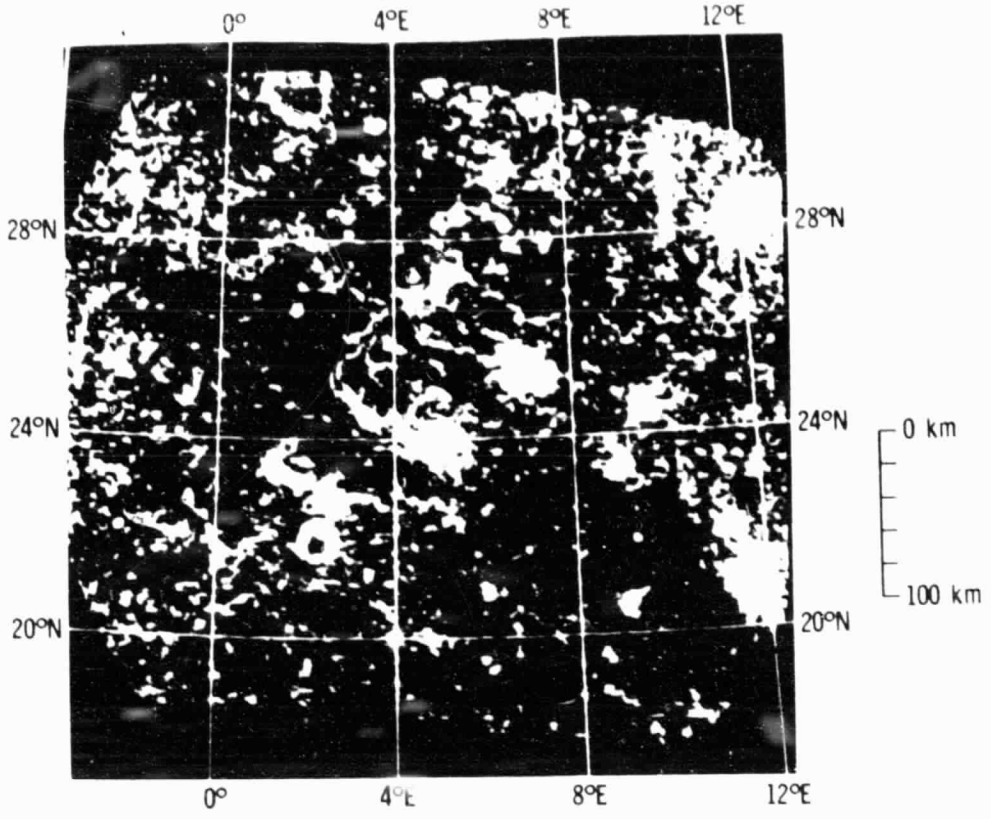

(b)

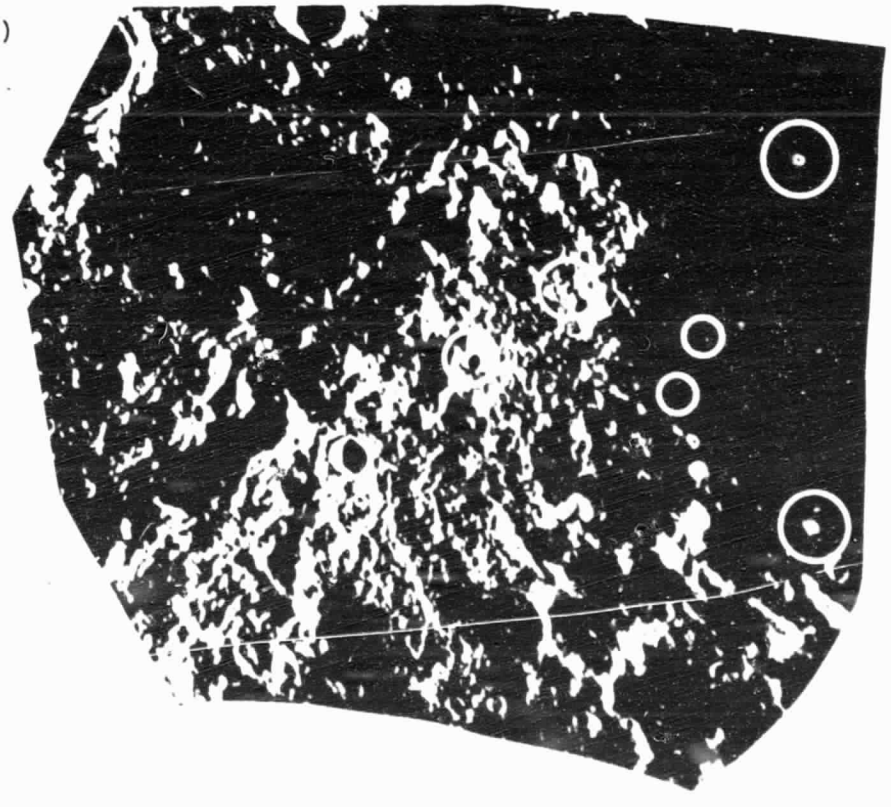

FIGURE 2

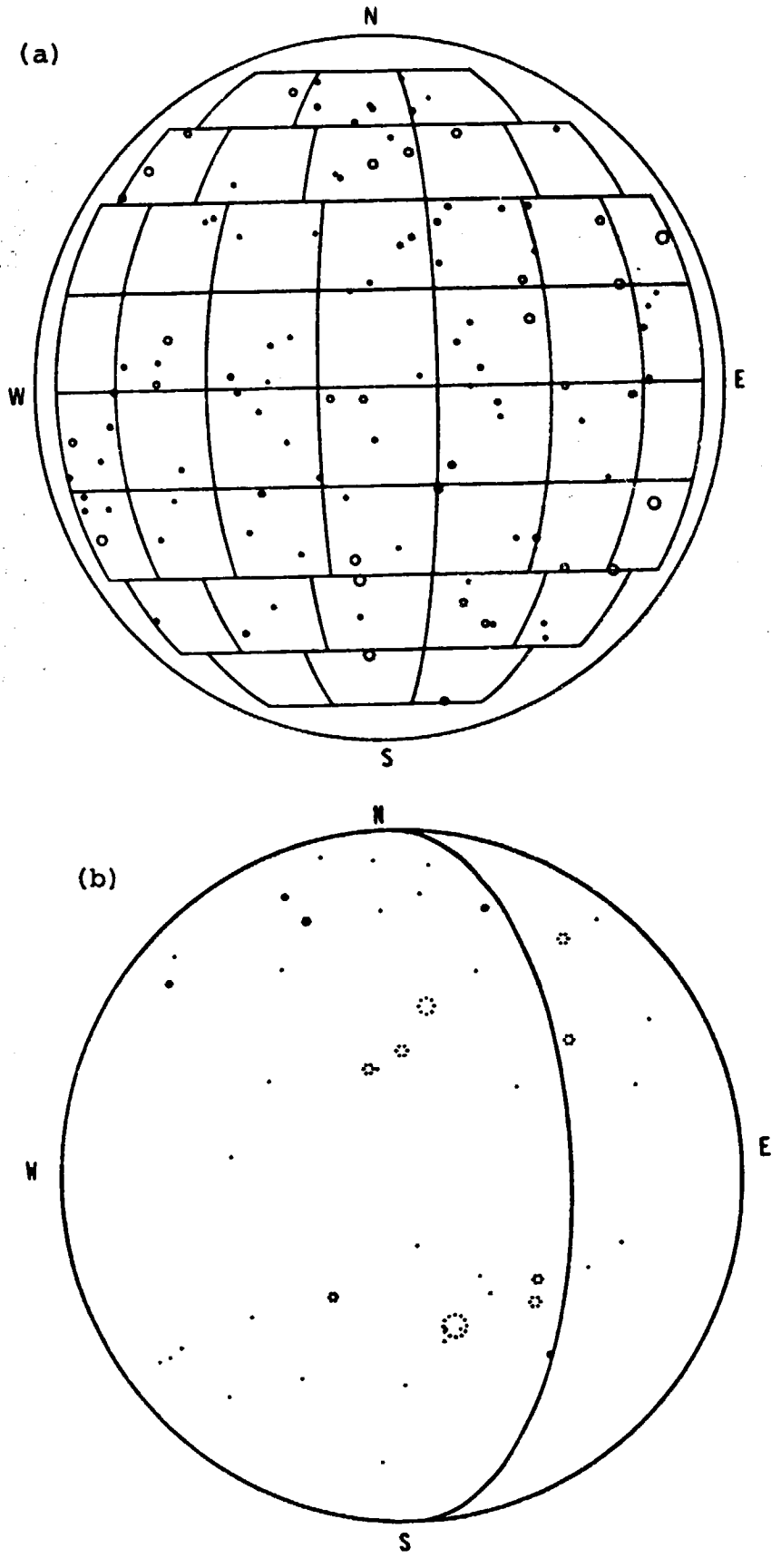

FIGURE 3

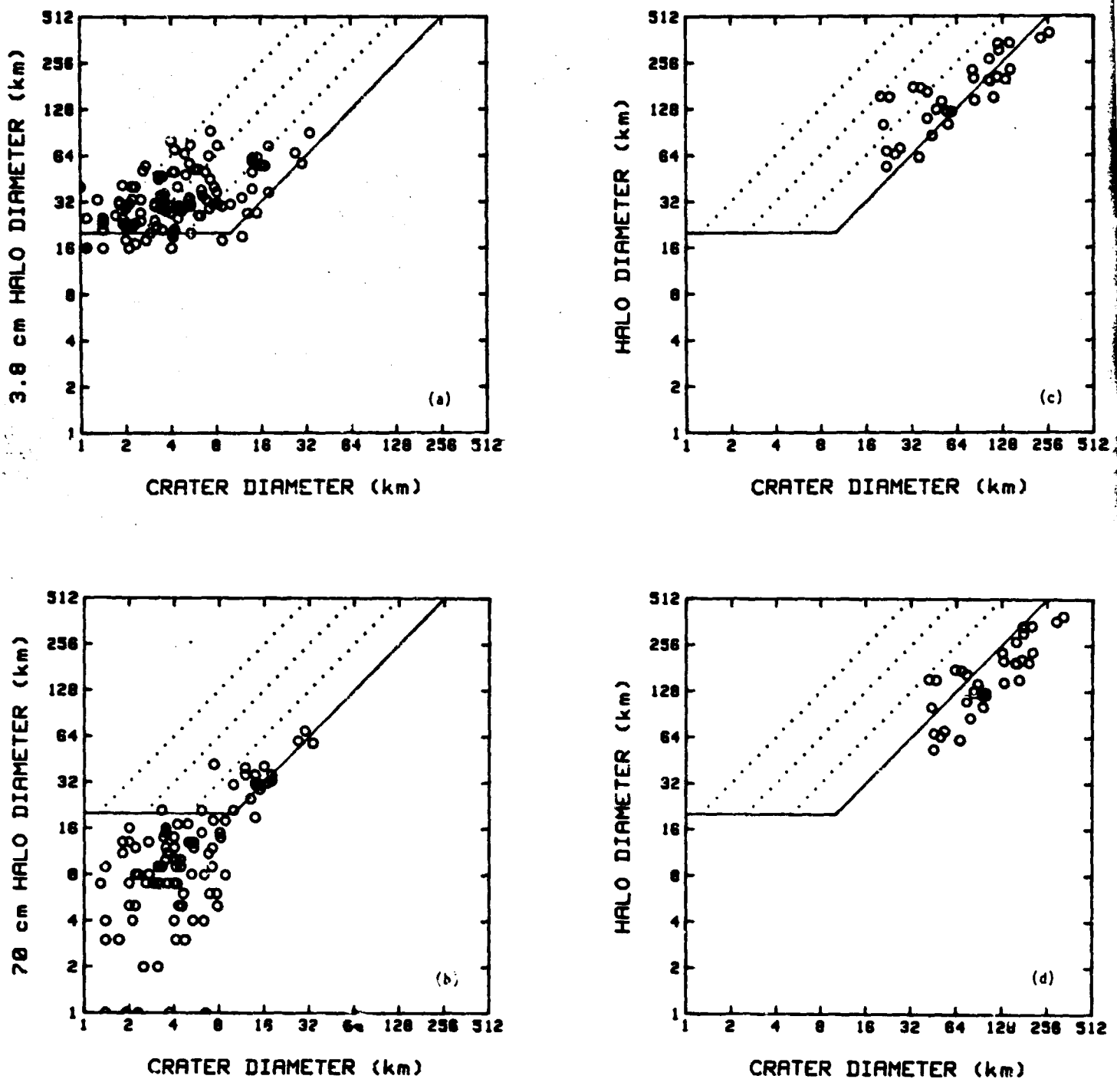
3.8 cm HALO DIAMETER (km)
HALO DIAMETER (km)
70 cm HALO DIAMETER (km)
HALO DIAMETER (km)
CRATER DIAMETER (km)
(a)
(b)
(c)
(d)
1
2
4
8
16
32
64
128
256
512

FIGURE 4

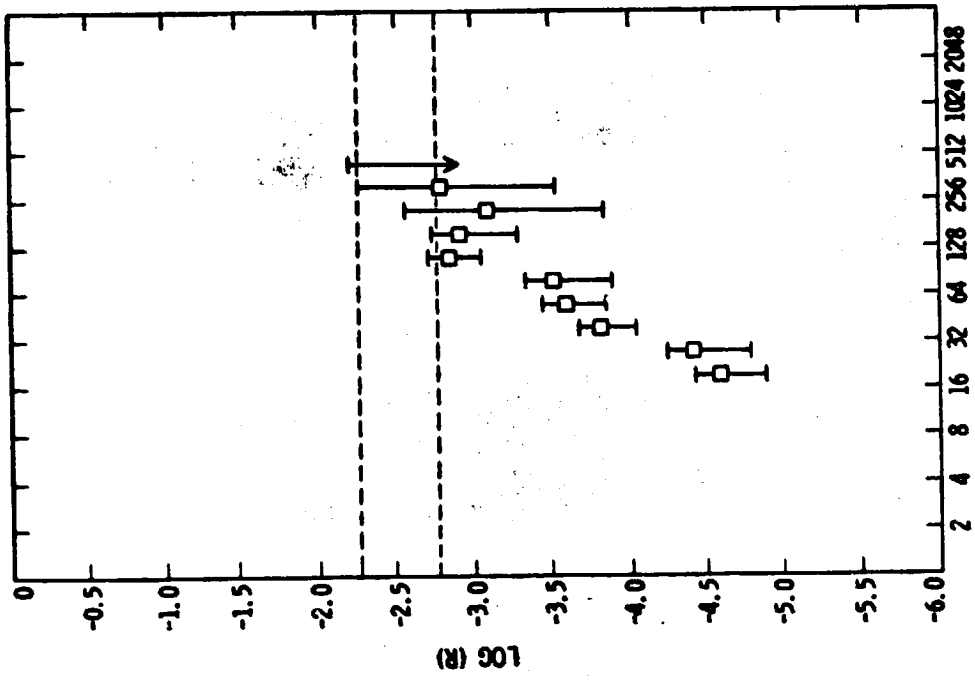

FIGURE 6

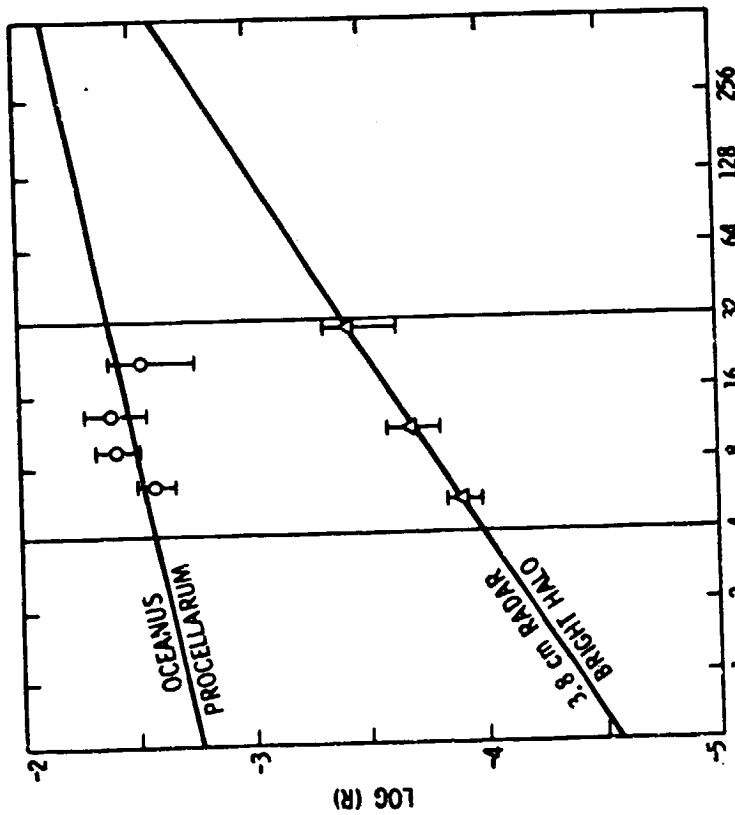

OCEANUS PROCELLARUM (67 CRATERS, 1.4 x 10^6 km^2)

3.8 cm RADAR BRIGHT HALO CRATERS (59 CRATERS, 12.0 x 10^6 km^2)

FIGURE 5

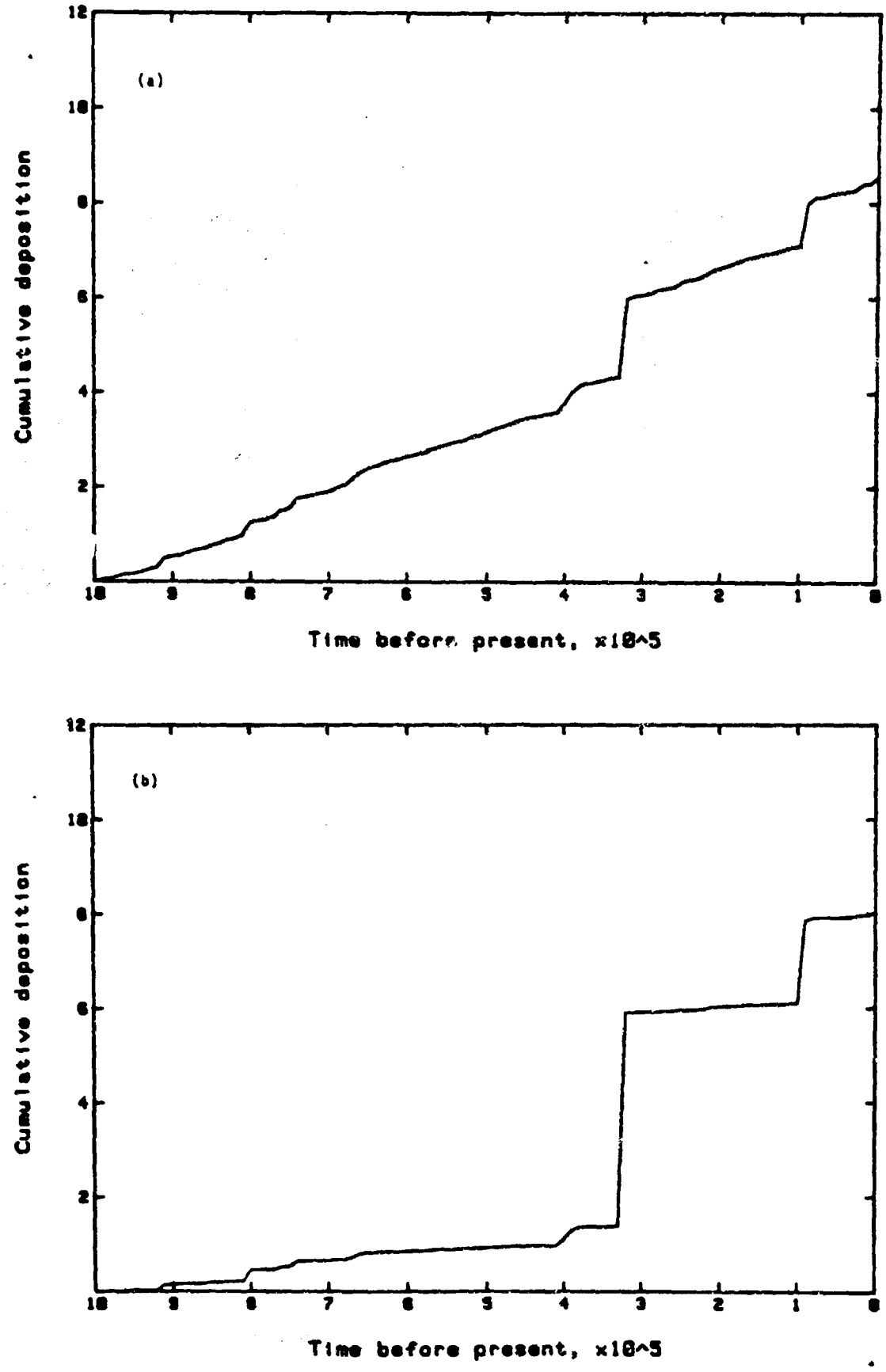
(a)
Cumulative deposition
12
10
8
6
4
2
10
9
8
7
6
5
4
3
2
1
0
Time before present, x10^5
(b)
Cumulative deposition
12
10
8
6
4
2
10
9
8
7
6
5
4
3
2
1
0
Time before present, x10^5

FIGURE 7

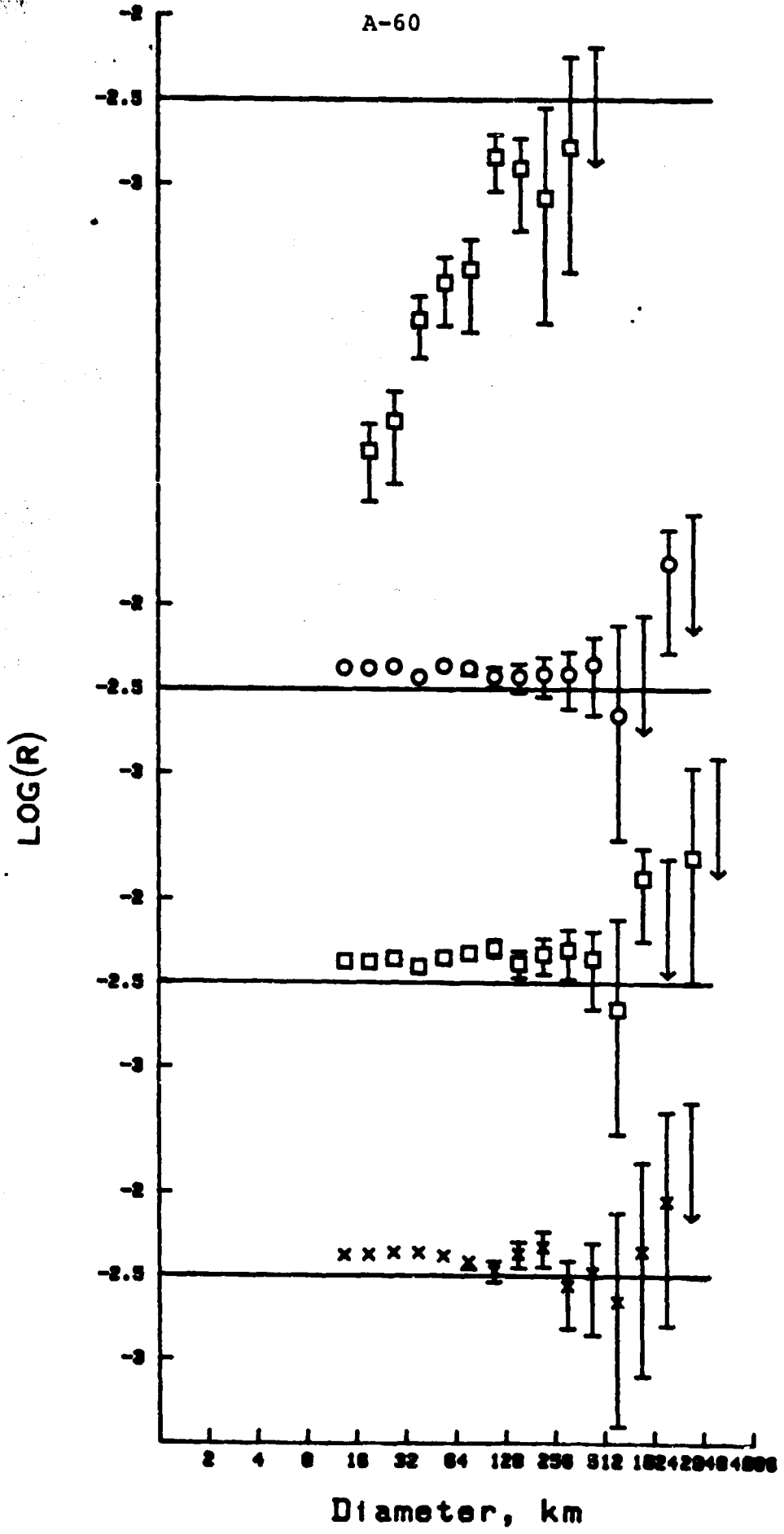
A-60
-2
-2.5
-3
-2
-2.5
-3
-2
-2.5
-3
-2
-2.5
-3
LOG(R)
2
4
8
16
32
64
128
256
512
Diameter, km

FIGURE 8

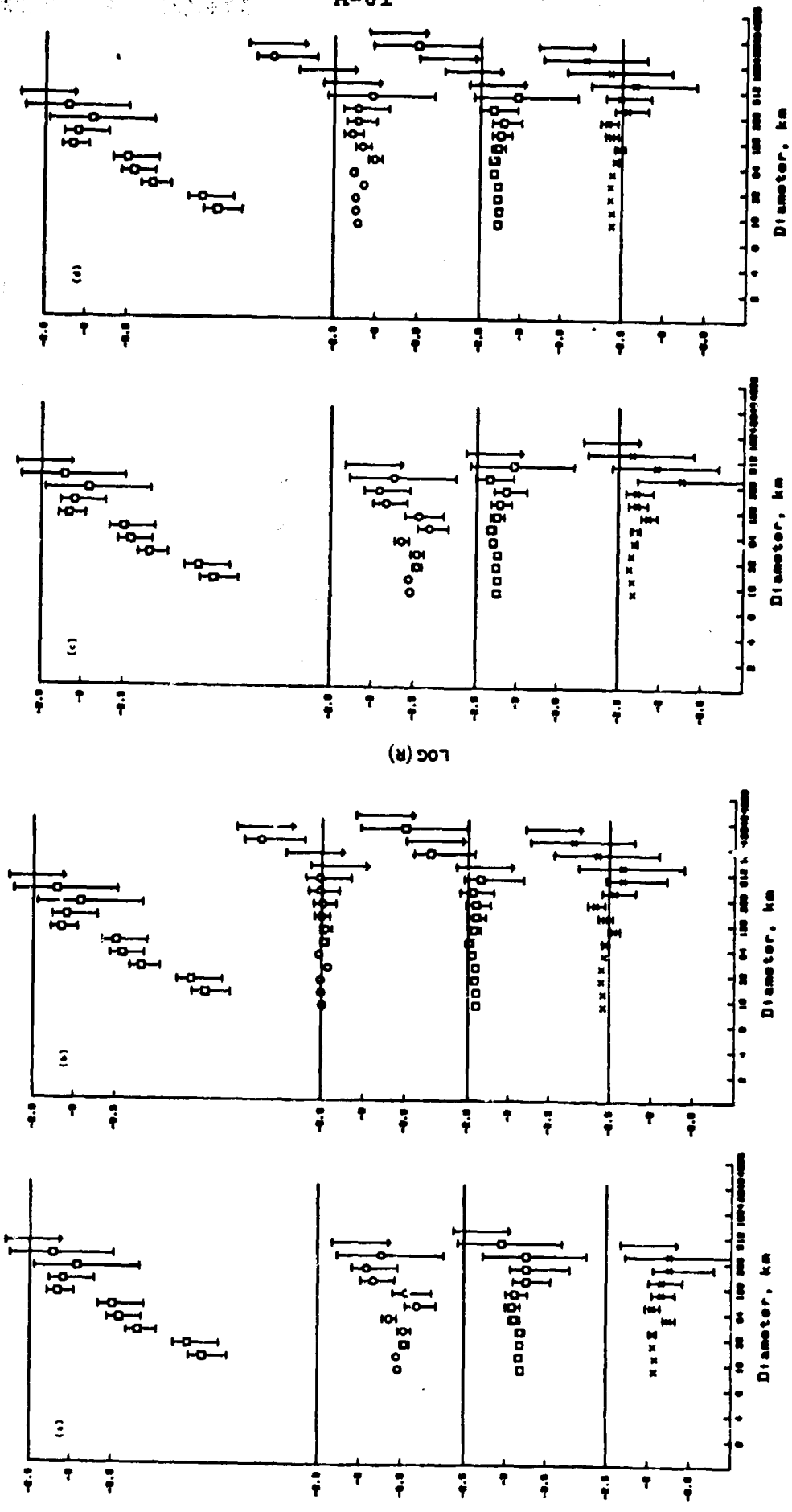

FIGURE 9

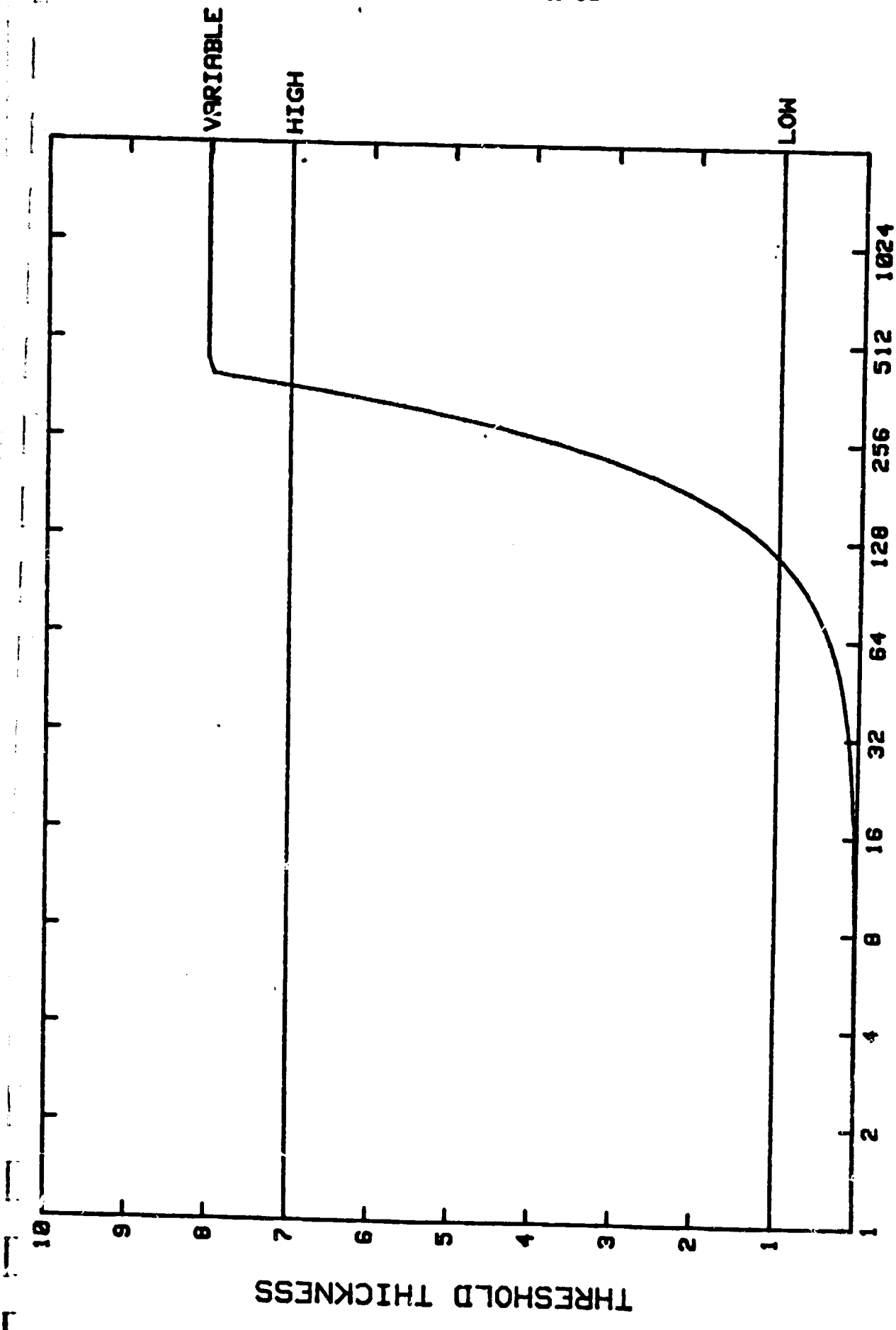
VARIABLE
HIGH
LOW
THRESHOLD THICKNESS
10
9
8
7
6
5
4
3
2
1
DIAMETER (km)
1
2
4
8
16
32
64
128
256
512
1024

FIGURE 10

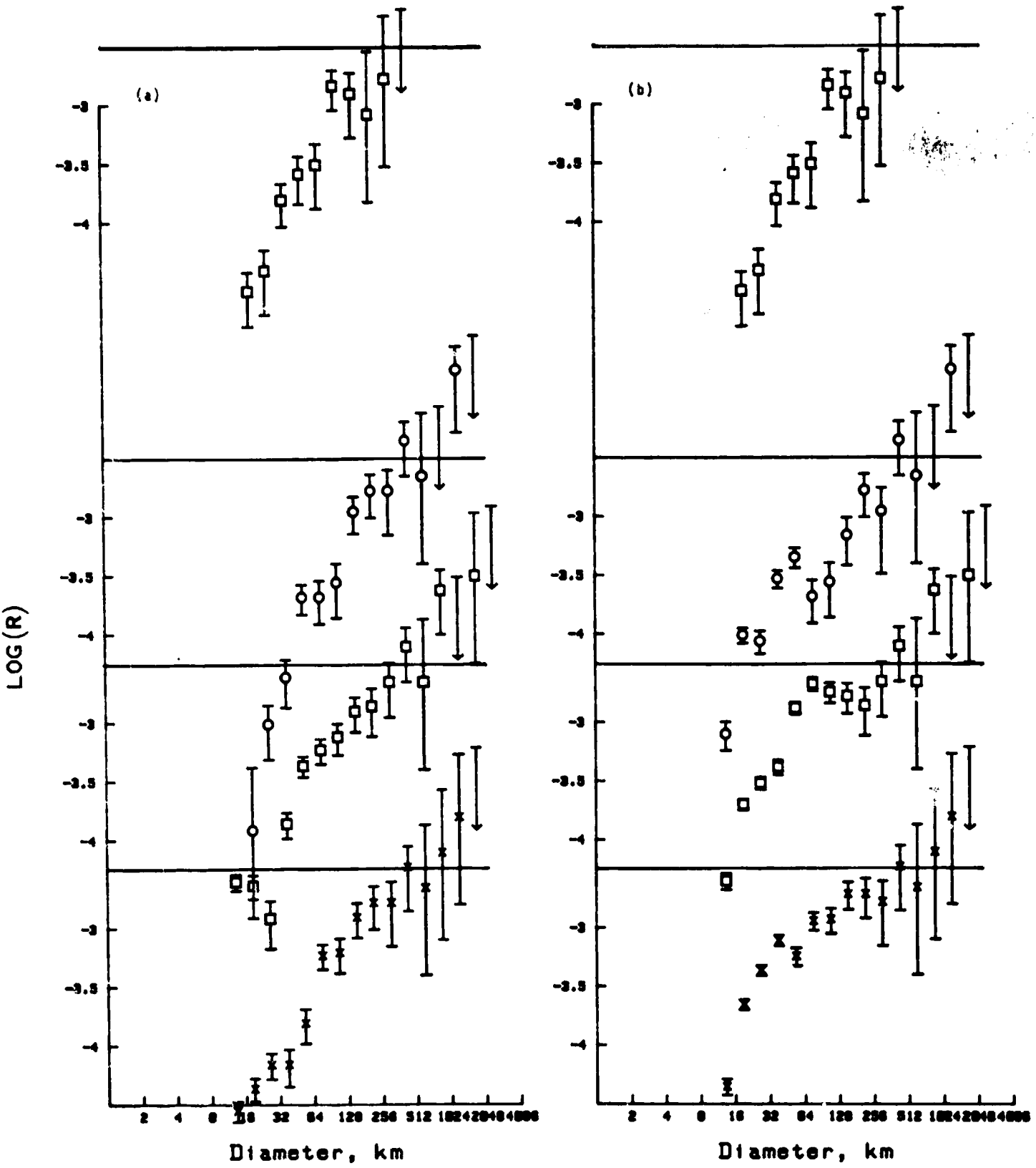

FIGURE 11

ICARUS 41, 000–000 (1981)

APPENDIX B

Lunar Craters with Radar Bright Ejecta

T. W. THOMPSON,*,[1] S. H. ZISK,† R. W. SHORTHILL,‡,[1] P. H. SCHULTZ,§ AND J. A. CUTTS*

*Planetary Science Institute, Science Applications Inc., Pasadena, California 91101; †NEROC Haystack Observatory, Westford, Massachusetts 01886; ‡University of Utah Research Institute, Salt Lake City, Utah 84108; and §Lunar and Planetary Institute, Houston, Texas 77058

Received December 29, 1980, revised March 19, 1981

A small fraction of the lunar impact craters with diameters of 1 km and greater have extensive enhanced 3.8-cm radar echoes associated with their ejecta deposits. The physical properties of these ejecta deposits and the ages of the central craters have been characterized via various infrared, radar, and optical signatures. Most of these ejecta deposits are radar bright at the 3.8-cm wavelength but are not radar bright at the 70-cm wavelength. Some ejecta have large infrared signatures, others do not. Although most of these ejecta have bright albedos in full-moon photographs, a significant fraction of the bright albedo markings do not extend beyond the crater. This mix of remote-sensing signatures indicates that craters with 3.8-cm radar bright halos are young and have ejecta deposits containing an excess of surface or near-surface rocks relative to the surrounding terrain. Abundant centimeter-sized rocks are inferred from the high 3.8-cm radar and infrared signatures. The low 70-cm radar signatures indicate that larger blocks are much less numerous. The population of craters with 3.8-cm radar bright craters on the Moon is much smaller than the population of craters in a similar size range on a young mare (Oceanus Procellarum) and has a different slope. This population is interpreted as a steady-state population reflecting a balance between the production of fresh craters and the destruction of the high infrared and radar signatures by small-scale cratering. The slope of difference between visual and radar craters is attributed to more rapid destruction of the radar signatures in smaller craters.

Relative densities of 3.8-cm radar bright craters and mare craters are estimated to be $0.04^{+0.01}_{-0.01}$ at a 4-km diameter and $0.100^{+0.02}_{-0.04}$ at a 32-km diameter. Assigning ages on the basis of these relative densities raises the question of whether the 4- to 32-km-diameter visual crater population is truly representative of a 3.3-by age. If it is, and if crater rates between 3.3 by and the present have been uniform, then the 3.8-cm radar crater lifetimes are estimated to be $0.13^{+0.05}_{-0.04}$ by and $0.03^{+0.01}_{-0.01}$ by at diameters of 4 and 32 km, respectively. Similarly, lifetimes of the infrared signatures of 4-km-diameter craters may be as short as 10^7 years. However, some data suggest that these estimates may be in error by a factor of 5 too small. Comminution of blocky ejecta material and the smoothing of slopes by lunar surface processes could account for the elimination of radar signatures on these time scales and the development of a steady-state crater population. An alternative interpretation, which we do not favor, is that the 3.8-cm radar bright crater population is formed by a subpopulation of primary bodies or by secondary cratering.

I. INTRODUCTION

A remarkable feature of the 3.8-cm radar maps of the Moon obtained during the late 1960s (Lincoln Laboratory, 1968) is the bright halos centered on impact craters and having 10 or even 20 times the diameters of the central craters. In this paper, we attempt the first systematic compilation of these features and we assemble supporting 70-cm radar, thermal infrared, and photogeologic data to assist in their interpretation. Our primary motivation for this investigation was to develop a better understanding of the physical properties of the ejecta deposits around impact craters that give rise to bright halos and to study the rate and manner in which these physical properties changed with prolonged exposure on the lunar surface. In addition we were interested in developing further con-

[1] Visiting Scientist, Lunar and Planetary Institute, Houston.

0019-1035/81/040000-00$02.00/0

001

straints on the mechanism of ejecta emplacement and in searching for changes in ejecta deposition due to substrate materials and geologic structure.

II. BACKGROUND

The first high-resolution radar maps of the Moon were obtained in the late 1960s using the Haystack 3.8-cm radar (Lincoln Laboratory, 1968). These first maps showed a number of areas that had strong echoes and were several tens of kilometers in diameter centered upon smaller (1 to 10 km in diameter) craters. Eighteen of these features were studied in detail by Thompson *et al.* (1974), who showed that they had little or no 70-cm radar enhancement but in some cases had infrared enhancements in Earth-based eclipse observations. Thompson *et al.* (1974) inferred that these bright features in the 3.8-cm radar images originated from strewn fields of centimeter-sized rubble.

An outstanding example of these features is the 4.9-km-diameter crater Piton B, shown in Fig. 1. Figure 1 (top) shows a 3.8-cm radar map (ZAC 4.11) of Piton B and its environs. Piton B has a bright halo with echoes four to eight times stronger than those of nearby areas that extend 10 crater radii from the center. A faint halo with echoes one to two times stronger than the background extends 20 crater radii from the center. We examined the 70-cm and infrared eclipse temperature maps of Piton B (see Thompson, 1974; Shorthill, 1973). The 70-cm radar echo power is four to eight times that of nearby areas and is localized to the crater. The infrared eclipse-temperature enhancement is 28°K and appears to extend 3 crater radii from the crater. Earth-based and Lunar Orbiter IV photographs of Piton B (Fig. 1, middle and bottom) show no unusual morphology. In the full-moon photograph, the bright spot associated with Piton B is localized to the crater itself and the bright ray pattern usually associated with pristine craters is essentially absent. A feature similar to that of Piton B occurs in the north rim of Cassini where an 18-km-diameter spot in the 3.8-cm radar image is centered on a 3-km crater.

Other examples of these features are shown in Fig. 2, which shows six prominent 3.8-cm radar bright halos for the lunar area encompassing western Mare Serenitatis and northern Montes Appeninus. Note that the 3.8-cm halos extend beyond the craters by many crater radii, and are larger than the full-moon ray patterns in the Earth-based photograph.

A goal of this study was to extend our knowledge of these craters by cataloging their occurrence and their infrared, radar, and optical properties. Some 120 of these craters were cataloged for the 1.2×10^7 km^2 of the lunar surface which is covered by the LAC maps. The infrared and radar signatures of these special lunar craters provide insights into the physical properties of fresh crater ejecta. Our use of Earth-based infrared and radar signatures to estimate crater ejecta characteristics is similar to a recent study of Aristarchus and small western mare craters by Schultz and Mendell (1978). They used high-resolution, Apollo 17 orbital infrared data (Mendell and Low, 1975), which observed night-time (predawn) lunar surface temperatures which are controlled by surface rocks larger than 30-cm. Here we use the Earth-based infrared eclipse and short (3.8 cm)- and long (70 cm)-wavelength radar data to investig. the physical properties (surface roughness and block populations) of crater ejecta deposits.

III. CATALOG AND STATISTICS OF CRATERS WITH RADAR-ENHANCED EJECTA

As described above, previous studies of the craters with 3.8-cm radar bright ejecta considered only 18 craters. Thus, a major question is how many of these craters exist and what are their visual, infrared, and radar characteristics? To answer this question, craters from the 3.8-cm radar maps were selected and their characteristics cata-

002

PITON B
3.8 cm RADAR MAP - ZAC 4.11 DEPOLARIZED

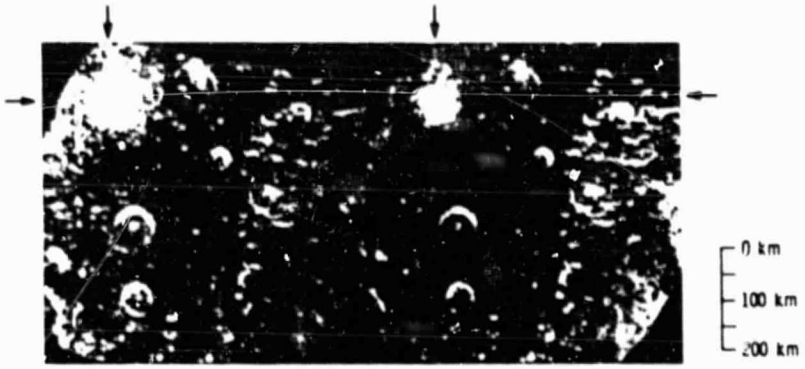

FULL MOON AND LOW SUN PHOTOS

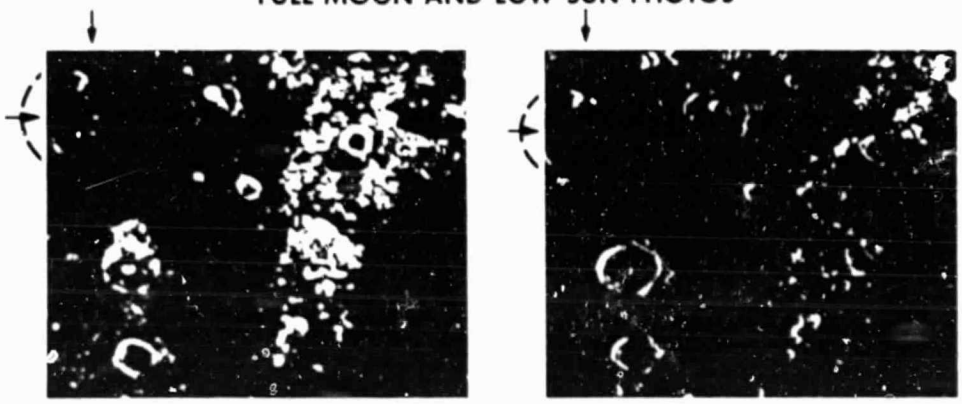

LUNAR ORBITER IV PHOTO

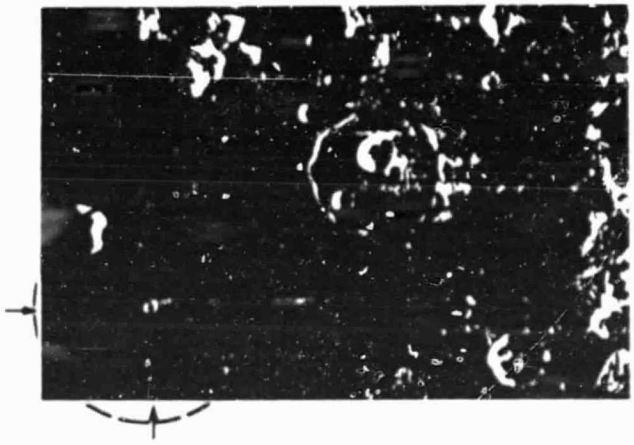

Fig. 1. 3.8-cm depolarized radar image, Earth-based and Lunar Orbiter photographs of Piton B and its environs. Piton B (0.1°W, 39.3°N, 4.9-km diam) is denoted by the arrows. Circles in the photographs have diameters of 50 and 100 km centered on Piton B. Other prominent craters are Cassini (4.5°E, 42.6°N, 56.5-km diam), Aristillus (1.2°E, 33.8°N, 55.3-km diam), and Autolycus (1.4°E, 30.6°N, 39.2-km diam). The 3.8-cm radar image on the right has increments which vary as multiples of 2. Thus, a single change in tone implies twice as much backscattered power.

003

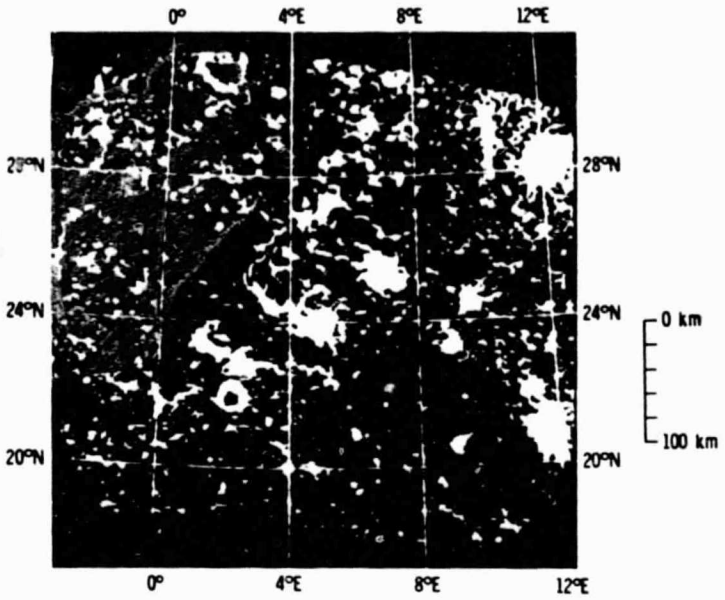

3.8 cm RADAR MAP - ZAC 3.01 DEPOLARIZED

FULL MOON PHOTOGRAPH
PLATE C-III CON. LUNAR ATLAS

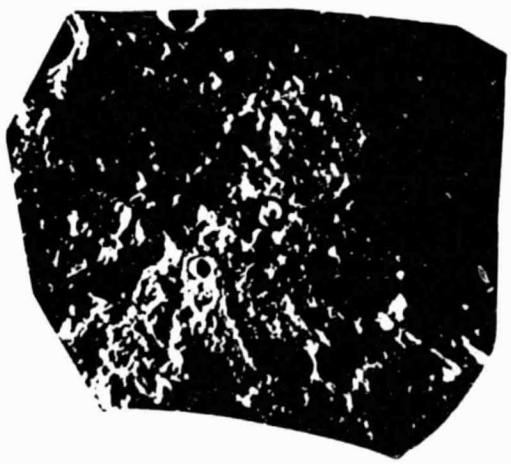

LOW SUN PHOTOGRAPH
PLATE C-9 CON. LUNAR ATLAS

FIG. 2. 3.8-cm depolarized and Earth-based photographs of Montes Appeninus and Western Mare Serenitatis. Circles in the Earth-based photographs denote sizes of the bright areas in the 3.8-cm radar image. Craters with large 3.8-cm radar halos include Linne (11.7°E, 27.7°N, 2.1-km diam), Hadley A (6.5°E, 25.0°N, 12.2-km diam), Aratus (4.5°E, 23.5°N, 10.6-km diam), and three unnamed craters in Western Mare Serenitatis with diameters between 1 and 2 km.

C-2

004

loged. The primary data source is the Earth-based 3.8-cm radar images obtained at the NEROC Haystack Observatory (Zisk *et al.*, 1974). The 3.8-cm radar data are complemented by earth-based 70-cm radar images obtained at the Arecibo Observatory (Thompson, 1974) and the Earth-based infrared eclipse temperatures (Shorthill, 1973). The optical properties of these features were obtained from Lunar Orbiter IV photography (Bowker and Hughes, 1971), full-moon photographs of the Consolidated Lunar Atlas (Kuiper *et al.*, 1967), and Apollo orbital photography where available. Also, observations by the Apollo Infrared Scanner (Mendell and Low, 1975) provide information about the physical properties of the ejecta of these craters.

These data have a range of resolutions. Resolution for the optical data is about 0.05 km and that for the Lunar Orbiter IV and Consolidated Lunar Atlas photographs, 0.5 km. Resolutions for the 3.8- and 70-cm radar data are 2.0 and 7.5 km, respectively. Resolution for the Earth-based infrared data varies between about 15 km at the disk center to about 30 km toward the limb; resolution of the Apollo Infrared Scanner was 7.0 km. (The infrared and radar resolutions are the projected surface size of a point target and are about one-half of a line-pair resolution.) The 70-cm radar and infrared resolutions are considerably poorer than the 3.8-cm radar resolution; some of the consequences of these coarser resolutions are discussed in Appendix A.

The selection of craters was based solely on 3.8-cm radar image size and crater diameter. Only craters with a 3.8-cm radar image size greater than 20 km and more than twice the crater diameter were included. The lower limit of 20 km for 3.8-cm radar halo size was chosen such that the smallest halo would be covered by at least one infrared resolution element and a few 70-cm radar cells. Similarly, limiting the halo size to twice the crater diameter was used to exclude large craters with narrow radar bright halos. This focused our attention on craters with sizes up to about 10 km, although a few larger craters with very broad radar bright ejecta deposits were included. The selection criteria are illustrated in Fig. 3. We cataloged some 120 craters as shown in Fig. 4 for the 1.2×10 km^2 of lunar surface covered by the LAC charts. Limb areas beyond the LAC chart were not cataloged because there are no 70-cm radar maps of these areas. The catalog area covers some 63% of the earth visible hemisphere.

The diameters of the radar halos associated with these craters in the 3.8- and 70-cm images were measured from both continuous tone and incremented displays of the data similar to those shown in Figs. 1 and 2. Depolarized radar data were used to reduce possible confusion between slopes and roughness (Thompson and Zisk, 1972). Infrared halo diameters were measured on a contour map which was quantized to 4°K, about twice the noise level in the original data. Measured infrared and 70-cm diameters were reduced by the resolution size to account for resolution smearing effects. Sizes of the photometrically bright areas associated with these craters were taken from the full-moon plates of the Consoli-

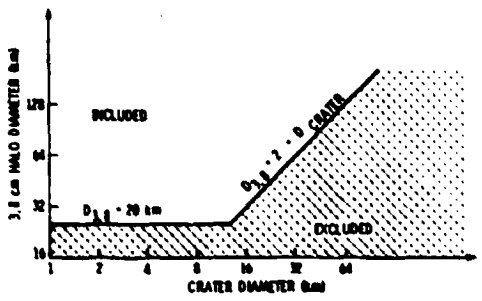

FIG. 3. Range of 3.8-cm radar halo sizes included in the 120-crater catalog. The criterion of being greater than 20 km for the smaller crater was selected so that 3.8-cm radar bright areas were covered by at least one earth-based infrarred resolution element and several 70-cm radar resolution elements. The criterion that radar bright areas be twice the crater diameter for the larger craters was selected so that only a few larger craters were selected. Thus, this study emphasizes craters with diameters between 1 and 10 km.

005

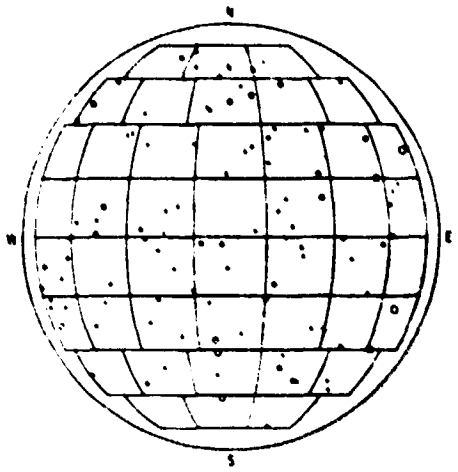

FIG. 4. Positions of the 120 craters with large 3.8-cm radar halos. Circle size corresponds to 3.8-cm halo size. Background grid shows available LAC charts. No craters in the limb areas were examined.

dated Lunar Atlas (Kuiper *et al.*, 1967). Sizes of optically bright halos associated with these craters in Lunar Orbiter photographs were measured where they occurred. Crater diameters were taken from the LPL Catalog (Arthur *et al.*, 1963, 1964, 1965, and 1966) or from the Lunar Orbiter IV photographs (Bowker and Hughes, 1971). Crater settings were identified as either mare or terra.

The peak intensity (strength) of the radar and infrared signal from the halo was also measured from the data described above. Where the halo was resolved by several resolution elements (most 3.8-cm measurements) this strength measurement is dominated by the signal returned from the crater floor and rim. Where the halo was not resolved, the floor, wall, rim zone, and ejecta of the crater all contribute to the measured value. In these cases the strength measurements provide a constraint on halo sizes as described in Appendix A. Radar strengths are in terms of enhancements relative to a background while infrared strengths are in terms of temperatures (in °K) relative to terra areas at the same angle of incidence.

IV. 3.8-cm RADAR BRIGHT EJECTA CRATER CHARACTERISTICS

The infrared, radar, and visual signatures of these craters can be interpreted in terms of surface characteristics. However, these interpretations may not be unique. The coarse resolution of some data means that the detailed size, shape, and intensity of the corresponding signature are not well defined for smaller craters. Even where size, shape, and intensity can be exactly specified, the implications for surface properties can be ambiguous. These limitations are not fatal, and in practice, the combination of several signatures provides a clearer picture of surface conditions than just one signature by itself.

The cataloging effort mentioned above provides a large data base for describing the surface properties of fresh crater ejecta. Whereas Thompson *et al.* (1974) studied only 18 craters, this report is based upon 120 craters. To show the signatures of these 120 craters in a meaningful way, the data are plotted as scatter diagrams of the strengths and halo sizes versus crater diameter in Figs. 5, 6, and 7, and as crater size–frequency distributions using the relative size–frequency distribution plots proposed by the Crater Analysis Techniques Working Group (1979) as shown in Figs. 8 and 9.

Radar and Infrared Halo Diameters

The size of the measured 3.8-cm ejecta halos ranged from 2 to 35 times the diameter of the central crater (Fig. 5a). The lower limit in the scatter plot was set by the criteria used to select the crater data set (Fig. 3). Radar bright halos at 70-cm wavelength are much less extensive than the 3.8-cm radar bright halos except for craters larger than 30-km where the 70- and 3.8-cm halos are approximately equal. The infrared images show a spectrum of behavior. Some craters have large infrared halos with sizes up to 20 crater diameters while other craters have no infrared halos at all.

006

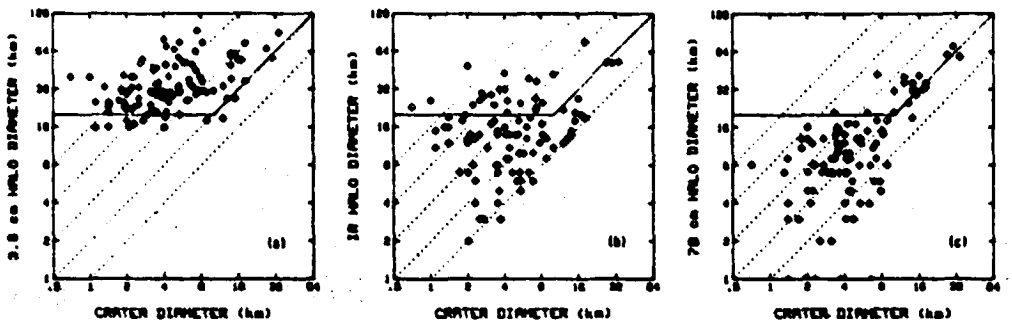

FIG. 5. Scatter diagrams of infrared and radar halo diameters versus crater diameter. Solid line indicates 3.8-cm halo diameter selection criterion (see Fig. 3). Dashed lines show halo diameter/crater diameter ratios of 1, 2, 4, 8, and 16, respectively. Measured infrared and 70-cm halo diameters have been reduced by one resolution cell size to account for resolution smearing (see Appendix A).

There are two kinds of problems with the diameter measurements presented in Fig. 5a which are imposed by the intensity and spatial resolution of the data. The limited intensity resolution of all data sets restricted our ability to determine exactly the diameter of the crater halos. The enhanced signature does not cut off abruptly at some distance from the crater; it fades away gradually. Clearly, the point at which the signature drops below the threshold of recognizability depends on the signal-to-noise of the observation. The spatial resolution limitations of the ir and 70-cm data compounds this problem for all but the very largest craters. These limitations must be understood before attempting to interpret the data presented in Fig. 5. In particular, there are large uncertainties in all ir halo diameters below 40 km and in 70-cm radar diameters below 20 km. However, strength measurements help constrain the size of small crater halos which appear as only an unresolved bright spot in the ir and 70-cm maps (see Appendix A).

Radar and Infrared Crater Strengths

The strength as used here is the peak signal from the crater feature relative to background. The strengths for the 3.8-cm radar return (Fig. 6a) vary between 4 and 8. For most of the data points this value refers to the center of a resolved halo and is dominated by a signal returned from the

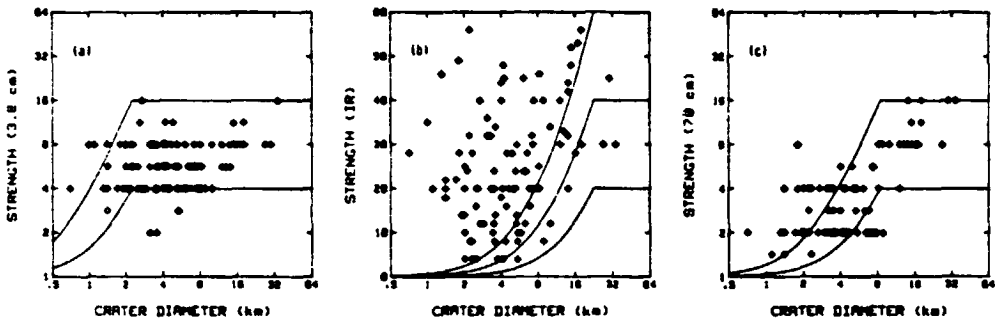

FIG. 6. Scatter diagrams of infrared and radar strengths versus crater diameter. Radar strengths are ratios of peak crater signal to background and are quantized to nearest power of root 2. Infrared strengths are temperature differences in °K with respect to terra at the same angle of incidence. Solid lines show signal dimunition for signals which arise solely from the crater and are observed with resolutions of 22.0, 2.0, and 7.5 km at infrared, 3.8-cm, and 70-cm wavelengths (see Appendix A).

007

crater floor, wall, and near-rim regions. There appears to be no systematic dependence of this strength index on crater diameter.

In contrast with this behavior, the ir strength signatures (Fig. 6b) have a large scatter, which arises from a number of sources. In the largest craters which are resolved by the ir data, (say larger than 16 km), the variation of 30 to 45°K in the strength index may indicate real variability in the properties of crater floor and rim materials. In contrast, the radar enhancements of these larger craters vary little. For smaller craters, the resolution loss contributes to variation in the strength index, and observed temperature difference range from 5 to 55°K. The theoretical curves in the ir strength index plot indicate the strength indices that would be observed from a crater of given diameter if the enhancement of 20, 50, or 60°K were confined to the crater interior. As noted, large crater interiors are not enhanced by more than about 45°K relative to their surrounds and it is difficult to conceive of physical properties of floor material which would give an enhancement of the crater interior exceeding 60°K. Evidently, most of these craters must have infrared enhancements extending well outside the crater and a number of them must have enhancements extending to a few tens of kilometers (see Appendix A). Unfortunately, we cannot uniquely determine the ir halo diameters from strength measurements for the craters smaller than 16 km. There are indications from the measurements on larger craters that there are variabilities in the properties of floor and ejecta materials and this probably occurs with the smaller craters as well.

A different pattern of variation of the strength index with diameter appears in the 70-cm radar data (Fig. 6c). In the larger craters which are resolved by the 70-cm data ($D > 8$ km) there is a fairly narrow variation in strength from 8 to 16 times background. For these resolved craters, the strength index refers to the properties of rim and floor materials; the small variability in these properties at 70 cm resembles behavior at 3.8 cm and contrasts with higher variability in the Earth-based infrared data. For smaller craters, resolution affects the observed strength. To facilitate the interpretation of the resolution-affected strength value, we have plotted predicted degraded strengths for craters with enhancements confined to the crater interior of 4 and 16 times the background. Most smaller ($D < 8$ km) craters have enhancements less than that predicted, suggesting that these craters have little, if any, halo. However, a few of these smaller craters have enhancement larger than that predicted by our model, suggesting that these craters have 70-cm radar halos. Most of these enhancements are 2 or 4, which would be expected for halos which extend beyond the central crater by only a few kilometers. Thus, the 70-cm halos appear to be much smaller than the 3.8-cm halos for these smaller craters. Again, ambiguities in the interpretation preclude a unique determination of the 70-cm halo diameter from the 70-cm signal strength.

Properties of Specific Craters

An appreciation of the effect of resolution on the signatures can be sharpened by a discussion of the properties of two craters.

The smallest crater in the present catalog (~0.7 km in diameter) is located at −50.4°, 0.2° and known informally as "Tiny Tim." The halo diameter of 40 km at 3.8 cm is well resolved by the radar data. The 3.8-cm strength index is four times the background. The infrared halo is just resolved despite the small size of the central crater but the estimated diameter of 22 km has a large uncertainty. The strength is at the low side of resolved craters although there are very few with which to compare in this size range. The crater is not spatially resolved in the 70-cm data, but a two times signature is identified with the crater. Comparison with

the theoretical curves indicates that at 70 cm the halo radius is probably a few crater diameters in size (see Appendix A).

Linné, the crater pictured in Fig. 2, is a 2.1-km diameter crater located in Mare Serenitatis. The halo diameter of 40 km at 3.8 cm is well resolved. The 3.8-cm strength index is four times the background. Thus, Linné appears similar to Tiny Tim in the 3.8-cm maps. Linné is only marginally resolved in the ir data; however, the strength indices indicate an ir signature extending several crater diameters beyond the rim. Linné is not spatially resolved at 70 cm but the high strength index suggests a 70-cm halo of a few crater diameters.

Summary

Our data on infrared, 3.8-cm, and 70-cm radar lunar crater halos provide some important constraints on the properties of these features despite degradation by resolution and selection effects. The 3.8-cm halos range up to 30 times the size of the craters itself. Although the strength of the 3.8-cm signal returned from the crater and rim lies in a narrow range, for this population of craters, the infrared data indicate that the strength of the ir signature for the crater and rim area in large craters is much more variable than that for the comparable 3.8-cm signatures. In larger craters, the ir bright halo extends to between 2 and 4 times the crater diameter. However, for some smaller craters, analysis of the strength data indicates that the ir halos are generally smaller than the 3.8-cm halos. In general, the larger ir halos are about one-half as large as the 3.8-cm halos. The 70-cm radar halos are quite narrow and confined to no more than a few times the crater diameter.

Optical, Photogeologic, and Population Characteristics

In addition to the infrared and radar signatures, other rater characteristics such as optical appearance, photogeologic interpretations, and crater populations are helpful in understanding the surface properties associated with craters with 3.8-cm radar bright halos.

Optical properties of 3.8-cm radar bright ejecta craters were characterized by the size of the photometrically bright spots associated with these craters in the Lunar Orbiter IV photographs (Bowker and Hughes, 1971) and in the full-moon plates of the Consolidated Lunar Atlas (Kuiper *et al.*, 1967). These data are shown in Fig. 7. Comparing these data with the 3.8-cm radar halo sizes in Fig. 5a (the 3.8-cm selection limits are shown in Fig. 7 to facilitate this), it is evident that a substantial number of craters with large 3.8-cm radar bright halos have very much smaller visible bright al-

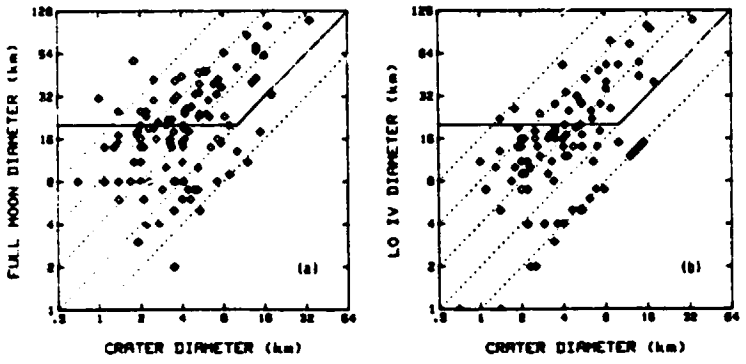

FIG. 7. Sizes of bright albedo areas in full-moon and Lunar Orbiter IV photographs plotted versus crater diameter. Plots use the same convention as the plots in Fig. 5. Note that the full-moon bright albedo areas for a few craters are no larger than the crater itself.

009

bedo features. Furthermore, there are a few craters with radar bright ejecta for which the full-moon albedo does not extend beyond the crater (like Piton B shown in Fig. 1). On the other hand, many of these features have photometrically bright ejecta in the low-sun Lunar Orbiter photographs; an expected signature for pristine lunar craters. Also a few of the craters, like Möltke, Copernicus H, and Dionysius, have 3.8-cm radar bright halos and optically dark ejecta in full-moon photographs. In view of the results of Figs. 5 and 7, it appears that a 3.8-cm radar bright halo is a more reliable criterion for identifying fresh craters than is enhanced visual albedo.

Apollo panoramic photography was used to test the correlation between 3.8-cm halos and fresh impact craters. A survey of Apollo 15, 16, and 17 photography identified pristine impact craters down to 0.5 km in size. Without exception, impact craters with well-preserved ejecta facies (hummocky continuous deposits, ray streaks, and ray patches) could be associated with a broad 3.8-cm enhancement. Most of the bright-rayed craters smaller than 1 km in diameter with 3.8-cm enhancements were not included in the general survey since their 3.8-cm halo sizes were smaller than 20 km.

Both Apollo and Lunar Orbiter IV photography suggests that the 3.8-cm radar bright halo craters are primary impacts. They have deep and symmetrical shapes while secondary craters tend to be shallow and asymmeterical. Size considerations also suggest that the radar bright halo craters are primary since secondary craters with diameters greater than 1 km require primary craters with diameters of 50 km or greater. Also, orbital infrared observations suggest that secondary craters are not blocky (Schultz and Mendell, 1978).

The general population properties of the 3.8-cm bright craters have been examined using relative size–frequency distribution plots proposed by the Crater Analysis Technique Working Group (1979). We plot $R = (\bar{D})^3 N/A\,(D_{max} - D_{min})$, where $\bar{D}$ is the geometric mean of crater diameters, N is the number of craters, A is the area, and D_{max} and D_{min} are the maximum and minimum crater diameters in a size bin. A crater population which has a cumulative distribution proportional to (crater diameter)$^{-2}$ and a differential distribution proportional to (crater diameter)$^{-3}$ plots as a horizontal line in a log(R) versus log(D) plot. Similarly, a crater population which has a cumulative distribution proportional to (crater diameter)$^{-3}$ and a differential population proportional to (crater diameter)$^{-4}$ has a slope of (-1) in a log(R) and log(D) plot.

Figure 8 shows the relative crater frequencies for the radar bright halo craters. Craters with infrared bright ejecta deposits form a subset of craters with 3.8-cm radar bright ejecta deposits and consequently their relative crater density is smaller (Fig. 8a). Densities of mare craters with 3.8-cm bright ejecta are indistinguishable from those on the terra (Fig. 8b). This is consistent with the notion that these craters have formed all over the Moon at the same rate and that their occurrence is not strongly affected by peculiarities in the local geologic materials. Finally, the population density of 3.8-cm radar bright craters (Fig. 9) is compared with the total population of photogeologically observed craters on one of the youngest lunar surfaces. It is seen to be substantially smaller (see also the plot in Fig. 4) and has a different slope; implications of this are explored in a later section.

V. ORIGIN OF ENHANCED SIGNATURES AND POSSIBLE IMPLICATIONS OF CRATER EJECTA EMPLACEMENT

The various crater halo signatures have implications for the physical nature and emplacement dynamics of crater ejecta materials. Our analysis of the Apollo photography indicated that all craters in our catalog with 3.8-cm ejecta enhancements for which good imaging data exist are also photogeologically fresh. Consequently, we

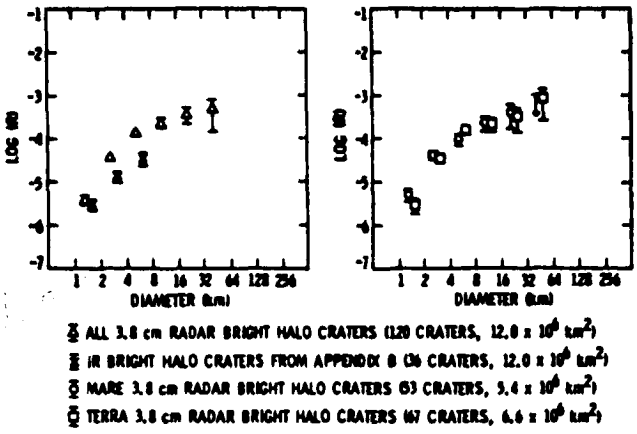

FIG. 8. Diameter–frequency distributions for craters with 3.8-cm radar bright halos (ejecta deposits). The left plot compares the population of all 3.8-cm bright halo craters with the subpopulation of radar bright halos that are also ir bright. The right plot compares mare and terra populations. Plotted diameters are offset slightly to promote readability of these similar distributions.

can draw on previous studies of young craters to assist us with our interpretations.

One of the key issues in the interpretation is relating 3.8-cm radar brightness to surface conditions. Thompson *et al.* (1974) suggested that excess surface and subsurface rocks 1 to 40 cm in size are the prime cause for enhanced 3.8-cm radar echoes. However, Moore and Zisk (1973) showed that 3.8-cm radar brightness did not correlate well with surface rock distributions in the vicinity of the Apollo 17 landing site at Taurus Littrow. Zisk *et al.* (1977) suggested changes in surface chemistry as a cause for radar echo modulation, but that appears unlikely here. However, surface roughness at the space–regolith interface with scales of 1 to 40 cm could cause the observed brightness in the 3.8-cm radar images. A mound or cavity at the space–regolith interface is about as effective as a rock with the same size and shape in generating radar backscatter. Thus, the extremely broad 3.8-cm halos associated with crater ejecta may reflect a combination of both surface roughness and excess ejecta fragments with sizes of 1 to 40 cm.

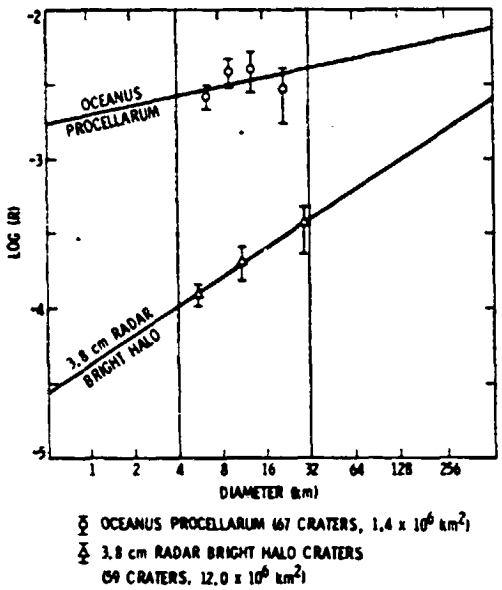

FIG. 9. Least-squares fit to crater distributions for Oceanus Procellarum (67 craters, 1.4×10^6 km^2) and 3.8-cm radar bright halo craters with diameters greater than 4.0 (59 craters, 12.0×10^6 km^2). Results of least-squares fit given in Tables II and III.

Studies of the High-Resolution Apollo Orbital Data

Apollo photography and data from the infrared scanning radiometer (ISR) on Apollo 17 are pertinent to consideration of these alternative models. Orbital photogra-

011

phy suggests a transition in fresh crater morphology at about 1 or 2 km in diameter (see Schultz, 1976). Small craters with diameters less than 1 km exhibit broad, block-strewn ejecta fields where ejecta deposits have coarse, meter-sized fragments up to several crater radii from the rim. Craters larger than 2 km exhibit a different morphology where meter-sized ejecta blocks are restricted to within a crater radius of the rim and a hummocky dune field of finer scale ejecta deposits extends to two to three crater radii beyond the rim (Taole I).

TABLE I

SUMMARY OF DATA ON BLOCK POPULATIONS AND SMALL-SCALE ROUGHNESS IN CRATER EJECTA DEPOSITS AND SYNTHESIS

	Previous data	These data	Synthesis
Small craters (less than 1 to 2 km)	*Apollo Imagery* (Schultz, 1976) indicate: • broad block-strewn ejecta fields containing meter-sized fragments extending several crater radii from the rim • no direct information about centimeter-sized blocks • dune field *ISR data* (schultz and Mendell, 1978) indicate: • no information for craters in this size range	*3.8-cm data* • Enhanced halo extending up to 15 or 30 crater radii indicating: + enhanced centimeter-sized blocks on surface or buried + rough dune features + clods of fine ejecta *IR data* • Some halos to 10 or 20 crater radii/others with smaller halos *70-cm data* o Must be smaller than a few radii	*Near rim and inner zone out to 5 crater radii* • Blocks 30 cm and larger enhanced relative to surrounds • Possibly centimeter- to meter-sized roughness also enhanced *Outer zone beyond 5 crater radii* • 10- to 40-cm-sized roughness or • 10- to 40-cm-sized blocks • No meter-sized blocks • No meter-sized roughness
Medium craters (larger than 1 to 2 km up to 10 km)	*Apollo imagery* (Schultz, 1976) indicate: • meter-sized blocks restricted to within a crater radius of the rim • hummocky dune field of fine scale ejecta extending to 2 to 3 crater radii from the rim *ISR data* (Schultz and Mendell, 1978) indicate: • Information about blocks larger than about 30 cm in size (decimeter) • crater interiors and rim areas have abundant decimeter-sized blocks • population of decimeter-sized blocks is typical of background beyond 0.5 crater radii	*3.8-cm data* • Enhanced halo extending up to 10 to 20 crater radii indicating + enhanced centimeter-sized blocks on surface or buried + rough dune features + clods of fine ejecta *IR data* • Some halos of enhanced ir emission inferred from strength data extending to at least 5 crater radii + enhanced population of rocks 10 cm in size and larger *70-cm data* • Narrow halo of enhanced 70-cm emission + narrow halo of surface or buried rocks 40 cm to 4 m in size	*Near rim <0.5R ejecta* • Centimeter to meter-sized blocks enhanced relative to surrounds • Centimeter to meter-sized roughness also enhanced *Inner zone 0.5R to 5 crater radii* • 10- to 40-cm-sized blocks • 10- to 40-cm-sized surface roughness • *No* meter-sized blocks or surface roughness *Outer zone beyond 5 crater radii* • 1 to 40-cm-sized roughness • 1 to 40-cm-sized buried blocks • *No* meter-sized blocks on

Orbital Photography is complemented by the infrared scanning radiometer data on Apollo 17 which observed predawn, nighttime temperatures which in turn are controlled by surface rocks larger than about 30 cm in size. Studies of these data (Table I) indicate that the bright rayed impact craters larger than about 1 km display a blocky crater interior and near-rim (within $0.3R$ of the rim) environment, but a relatively nonblocky ejecta facies beyond $0.5R$ of the rim (Schultz and Mendell, 1978). Thus, for craters larger than 1 to 2 km, submeter- to meter-sized blocks are confined to within a crater radius and possibly half a crater radius of the rim and an ejecta blanket of unknown physical properties extends several crater radii beyond the rim.

The 70-cm data are consistent with the orbital infrared and photographic data which suggest that meter-sized blocks are confined to within about a crater radius of the rim. However, the 3.8-cm data indicate blockiness or roughness in the size range of a few centimeters and larger extending to 10 or 20 crater diameters in some cases. The ir eclipse data which are specific to surface rocks 10 cm in diameter and larger indicate that, for some of the 3.8-cm radar bright ejecta craters, there is a blocky deposit extending to 10 crater radii or less for most craters larger than 2 km. Craters smaller than 2 km appear to exhibit blockier ejecta deposits out to greater relative ranges. These ir and radar observations suggest an idealized sequence for craters larger than 2 km. The near-rim (within $0.5R$) ejecta are composed of centimeter- to meter-sized blocks (70 cm, ir, 3.8-cm signatures) surrounded by ejecta deposits dominated by material 10 cm (lower limit for ir and no 70-cm signature) to 40 cm (upper limit for 3.8 cm and no 70-cm signature) in size out to about 5–6 crater radii. The outermost zone out to 20 crater radii is characterized by a relatively narrow range of material or surface roughness (range 1–40 cm for 3.8-cm signature).

Our observations are consistent with the observations of Schultz and Mendell (1978) and provide further information about the scale sizes of ejecta for craters larger than 2 km in diameter. The Apollo infrared data indicated little meter-sized debris beyond $0.5R$ from the rim, but the Earth-based ir and 3.8-cm radar data here suggest that smaller 10- to 40-cm debris or surface roughness occurs beyond this zone, undetectable in the response of the Apollo infrared instrument. Thus, craters smaller than 1 km display a broad field of meter and submeter-sized debris in the Apollo infrared data, in orbital photography, and in the new results here.

The 3.8-cm radar enhancement associated with crater ejecta may have contributions from three possible sources. First, it may express small size ejecta (<50 cm) that survived impact into the regolith and were scattered across the surface in the upper regolith. This mode of emplacement has been reproduced in the laboratory by clustered impacts (Schultz *et al.*, 1980). Second, the halo may reflect extensive surface scouring and secondary cratering in the regolith by small-sized (<10 cm) ejecta. Third, it may indicate impact fragmentation of larger ejecta that are then scattered downrange from the point of impact (Schultz and Mendell, 1978). The relative contributions of these processes to the origin of the 3.8-cm halo require further study including comparisons with experimental and theoretical models of ejecta emplacement.

An interpretation of Earth-based and radar signatures based upon surface and subsurface rock populations and the hypotheses originally proposed by Thompson *et al.* (1974, 1980) is given in Appendix B. This suggests that the youngest craters have large infrared strengths and sizes emanating from strewn fields of surface rocks which extend beyond the craters. Older versions of these craters have infrared enhancements which are confined to the crater interior and rim areas, but still have large 3.8-cm radar bright halos which arise

013

from excess populations of buried centimeter-sized rocks in the regolith.

The analysis of the various remote-sensing signatures have been synthesized into models of the distribution of blocks and surface roughness in various ejecta zones for two size ranges of fresh craters (Table I). The ejecta characteristics of craters larger than 10 km are similar to those between 2 and 10 km, but the number of fresh craters in this size range included in this study is quite small. The principle conclusion is that blocks and other forms of roughness are enhanced in the ejecta and that the furthest ejecta has the smallest sizes. This is expected since the ejecta at these larger ballistic ranges has experienced larger mechanical comminution and larger peak shock histories than ejecta closer to the crater (Schultz and Mendell, 1978).

VI. AGE RELATIONSHIPS AND IMPLICATIONS FOR LUNAR SURFACE PROCESSES

The data described above indicate that the craters with bright 3.8-cm radar halos are young and they occur relatively infrequently. This suggests that the 3.8-cm bright halos are rapidly degraded by lunar surface process. We now examine the age of these radar bright craters and its implications about lunar processes.

Age Relationships

Figure 9 shows the population of craters with 3.8-cm bright ejecta as compared with the population of all craters on Oceanus Procellarum (Planetary Basaltic Volcanism Working Group, 1980). Power curves, which plot here as straight lines, have been least-squares fit to the data (Table II). For the 3.8-cm data, craters smaller than 4 km have been excluded for reasons of both resolution loss and the selection effects that reduce the observed population below this diameter (Fig. 5). The least-squares fit showed that the radar bright halo craters with diameters 4 and 32 km occur 0.04 and 0.10 as frequently as all craters in Oceanus Procellarum with those sizes (Table III).

Guinness and Arvidson (1977) have compared small crater densities (0.83–1.843 km) at the Apollo 12 site in Oceanus Procellarum (Table II) with crater densities of two other younger sites for which plausible radiometric ages exist. They concluded that the cratering rate has been uniform between 3.3 by years (the data of the most recent flows at the Apollo 12 site) and the present. If we adopt this result and also assume that the visual crater population between 4 and 64 km in Tables II and III is representative of the 3.3-by age we infer that lifetimes for the 3.8-cm radar bright ejecta signatures are $0.13^{+0.08}_{-0.04}$ and $0.33^{+0.33}_{-0.13}$ by for craters of diameter 4 and 32 km, respectively. Errors cited are formal statistical errors for the crater counts. Applying the same methods to the population with strong infrared signatures is difficult because this population is small and the larger crater sizes are affected by resolution loss at smaller crater sizes. However, assuming that the population at 4 km is fairly complete (Fig. 8a), we infer that the lifetime of these 4-km ir bright halos is 3×10^7 years.

One problem with this analysis is that the reference population of craters in Oceanus Procellarum 4–32 km in diameter probably includes a number of older craters that were only modified and not obliterated by the 3.3-by flows. The fractional representation of older craters can be large because they could include craters formed in a period before 3.3 by when impacting rates were very much higher. Reinforcement for this view is provided by a comparison (Table II) of the Guinness and Arvidson estimates of crater density at 1 km (we have converted our log R to their log A values) with extrapolations of the 4- to 32-km crater counts of the Planetary Basaltic Working Group (1980). Assignment of reliable ages to these radar bright craters will require further improvements in our understanding of rates of production of 4- to 32-km-diameter craters between 3.3 by and the present.

014

TABLE II

COMPARISON OF RELATIVE DENSITIES OF RADAR BRIGHT CRATERS AND VISUALLY IDENTIFIED LUNAR MARE CRATERS

Type of data	Number of craters in sample	Crater diameter range	Crater density Estimate for area of 10^6 km^2 referred to 1-km diameter[a]					
			Relative density		Incremental frequency		Cumulative number	
			Log R	Slope (m)	Log A	Slope (γ)	N	Slope (ϕ)
1. Craters with 3.8-cm radar bright ejecta (this paper)	59	4–64	−4.36 ±0.19	0.64 ±0.22	−4.36 ±0.22	−2.36 ±0.22	26.6	−1.36 ±0.22
2. Visually[b] identified craters in Oceanus Procellarum (planetary Basaltic Working Group, 1980)	67	4–64	−2.70 ±0.28	0.20 ±0.28	−2.70 ±0.28	−2.80 ±0.28	1085	−1.80 ±0.28
3. Visually identified craters at Apollo 12 site	407	0.083–1.843	Not available		−1.77 ±0.02	−3.78 ±0.03	Not available	
Oceanus Procellarum (Guinness & Arvidson, 1977)[c]	156	0.354–1.843	−1.84 ±0.05	−1.05 ±0.3	−1.84 ±0.05	−4.05 ±0.3	5576	−3.05 ±0.3

[a] Several different schemes of expressing crater densities have been used in the literature. We have used the relative size-frequency distribution recommended by the Crater Analysis Techniques Working Group (1979) for our data. However, since we wished to compare these results with those of other workers we have computed equivalent incremental frequencies and cumulative numbers.

[b] The 4- to 6-km population used here was based on published data in the Planetary Basaltic Working Group report (1980). We obtained the raw data from W. K. Hartmann. The counts were actually made by R. G. Strom and C. C. Allen.

[c] The incremental crater density estimates for 407 craters are those presented by Guinness and Arvidson (1977). They did not estimate either the relative or the cumulative density. These are based on data from two lunar orbiter frames: a medium-resolution frame and a high-resolution frame. The crater density estimates for 156 craters were made by using tables of raw data provided us by Ed Guinness and Ray Arvidson and only use data from the medium-resolution frame and therefore have a more limited diameter range. However, the estimated crater density and slope lie within the statistical error bars. Values of estimated crater density at 1 km for data set 2 are about a factor of 10 larger than the estimate based on the small crater population (data set 2). This suggests that many of the larger >1-km craters in data set 2 are older than 3.3 by. A more detailed analysis of these age relationships is needed.

The Guinness and Arvidson values are a factor of 5 lower.

Shoemaker (1977) gives an estimate of the impact rate of Apollo–Amor objects in recent lunar history. His impact rate for our study area and ages of 3×10^7 to 3×10^8 years gives estimated total numbers of craters which agree with the numbers of radar bright halo craters. We should point out that Apollo–Amor objects are only a subpopulation of all objects that impact the Moon and the relative proportions of these to cometary objects is very uncertain (Wetherill, 1979a and b).

Implications for Lunar Surface Processes

Let us consider whether the observed occurrence and lifetimes of 3.8-cm bright radar craters are consistent with what we known about crater formation and lunar surface processes. The signature from 3.8-cm bright halo craters is influenced by two major factors: the state of ejecta when it is originally emplaced and its subsequent gardening by meteoroidic bombardment.

From analysis of the ir and radar signature of crater halos we conclude that the process of ejecta deposition results in some combination of excess blockiness and roughness compared to the mature regolith adjoining the ejecta blanket. One can plausibly argue that with exposure to meteoroidal bombardment at the lunar surface, rough ejecta surfaces are leveled by

015

TABLE III

ESTIMATES OF AGE RELATIONSHIPS FROM CRATER DENSITIES

	Relative crater density, log (R)	
	4-km-diameter craters	32-km-diameter craters
Radar craters[a]	-3.98 ± 0.08	-3.40 ± 0.16
Visual craters[b]	-2.58 ± 0.13	-2.40 ± 0.17
Δ Log R	1.40 ± 0.15	1.00 ± 0.23
$\frac{R \text{ radar craters}}{R \text{ visual craters}}$	$0.040^{+0.018}_{-0.011}$	$0.100^{+0.07}_{-0.04}$
Age of radar craters (by)	$0.132^{+0.06}_{-0.04}$	$0.33^{+0.23}_{-0.13}$

[a] Data presented in this paper (see data set 1 of Table 2).

[b] Data from the Planetary Basaltic Working Group (data set 2 of Table 2).

the rain spattering effect (Soderblom, 1970) and excess populations of surface and subsurface rocks disappear by impact fragmentation (Hörz *et al.*, 1975; Gault *et al.*, 1974). A reasonable scenario attributes the enhanced ir and radar signatures to rocks, that the ir signature disappears first as surface rocks are broken down and the 3.8-cm signature disappears later as the buried rocks are exhumed and ruptured. This would explain why the ir bright ejecta deposits are only a subset of the craters with 3.8-cm bright ejecta. Buried centimeter-sized rubble is the most probable source of the halos with the 3.8-cm radar enhancements and no infrared enhancement.

If this scenario is correct, then rock comminution rates provide another method of estimating the lifetimes of the 3.8-cm radar and ir signatures of ejecta deposits. In particular, the lifetimes of the infrared and radar signatures of these features depend upon the rate at which surface rocks are catastrophically ruptured, as well as the rate at which lunar regolith is turned over. The former has been modeled by Hörz *et al.* (1975), who showed that a centimeter-sized rock will survive 10^8 years. This model suggests that the radar bright halo craters with large ir signals and size have ages of 10^7 to 10^8 years. After 10^7 to 10^8 years, the radar enchancements associated with the ejecta will be controlled by gardening of the regolith. The models of Gault *et al.* (1974) provide an estimate for the lifetimes of these older (but still radar enhanced) ejecta, since they show that the first meter of the lunar surface is turned over once every 10^9 years. This model suggests that the older radar bright ejecta will have ages less than 10^9 years. Thus, these model data are consistent with the inferred lifetime of $\sim 10^7$ years for the infrared halo which is associated with surface rocks and with the inferred lifetime of 1.3 to 3.3×10^8 years for the 3.8-cm halo which can be associated with both surface rocks and subsurface rocks. However, detailed modeling of the evolution of an ejecta layer under meteoroidal processes and rigorous computations of the signatures from a terrain with a population of surface and buried rocks are needed to demonstrate quantitative agreement. Also, differences in the lifeyimes of enhancements around large and small craters may arise from differences in thickness and initial size distributions of ejecta.

Another important point is that the evolution of the infrared and radar signatures for the halos is possibly size dependent. Smaller craters will probably lose their radar and infrared bright halos faster than larger craters. Although the size-frequency distributions of these craters with bright halos will depart from the classical photogeological "production" and "steady-state" distribution, they may still represent a steady-state population. This occurs for the infrared and radar signatures of crater interiors (Thompson *et al.*, 1980) and appears to occur for crater ejecta also (Fig. 9). However, the sampling criterion for radar craters changes at 10 km in the existing data set and a more careful analysis of this on the population slope should be performed.

In summary, various arguments suggest that infrared and radar bright ejecta have lifetimes which depend upon crater size.

016

Larger craters have longer lifetimes than smaller craters. A least-squares fit of the crater size–frequency data suggests lifetimes of 1.3 to 3.3 × 10^8 years, which is consistent with the Apollo–Amor impact predictions of Shoemaker (1977) as well as a rock comminution processes model of Hörz *et al.* (1975) and the regolith gardening models at Gault *et al.* (1974).

VII. CONCLUDING REMARKS

The data and analyses presented above suggest that lunar craters with large, bright radar, and infrared halos are the younger features on the Moon and probably no older than 10^7 to 10^8 years (depending upon both size and their infrared and radar signatures). The enhanced radar and infrared signatures from the ejecta deposits of fresh craters are produced by various combinations of enhanced blockiness and roughness. With exposure to lunar surface processes, roughness and blockiness are restored to the value typical of the surrounds and the remote-sensing enhancement disappears.

There are a number of future studies which would shed even more light on these features. (1) Our small size limit of 20 km should be decreased to about 10 km and our large size limit of (two times crater diameter) should be eliminated entirely. (2) New 70-cm radar and infrared images with resolutions on the order of 3 km would yield better estimates of halo size and strengths. (3) Models for crater ejecta emplacement need to be improved to understand how much ejecta is emplaced and also to understand what ejecta rock-size distributions are. (4) Models for regolith generation need to be improved to understand how rock populations in crater ejecta blankets evolve with time. And, (5) electromagnetic scattering theory needs to be improved to better understand how radar enhancements relate to surface and subsurface rock populations. [Items 2, 4, and 5 are also needed to further our knowledge about the evolution of the radar signatures of crater interiors described by Thompson *et al.* (1980)].

APPENDIX A

Resolution Effects and Interpretation of Infrared and Radar Sizes and Strengths

The crater halo features discussed in this paper range in size from features 30 times the spatial resolution of the data to features with sizes that are believed to be some fraction of the resolution of the data. Resources did not permit a sophisticated image restoration for features near the resolution limit. Instead, we used some first-order estimation methods to correct for the effects of resolution and to test hypotheses about the sources of signals.

A basic resolution correction applied to all the data and reflected in the halo diameter plots of Fig. 5 was to subtract the nominal resolution of the instrument from the apparent size of the crater halo. This unsophisticated correction allows us to demarcate those features which are essentially unresolved by the instrument and those which are resolved. Obviously, the "corrected" diameters of features originally near the resolution limit are still highly uncertain and the apparent sizes may depend on the areal intensity of the signal.

For the ir and 70-cm radar signatures the resolution is only adequate to clearly define the diameters of halos of a few tens of kilometers (Fig. 5). However, information on the strength (intensity) of an unresolved halo can be used to place constraints on the size of that halo using plausible assumptions about the distribution of the signature enhancement in the crater and crater surroundings.

The method of using signal strengths to define halo size can be illustrated with the Earth-based infrared data.. Assume that a small crater has an enhanced ir response which is significantly smaller than the instrument resolution. A simple model for the observed strength assumes that the infrared

017

signal arises from a circular area of uniform temperature embedded in a circular resolution element. Then

$$(T_b + \Delta T_o)^4 = T_b^4[1 - (D^2/R^2)] + (T_b + \Delta T_c)^4(D^2/R^2), \quad (A.1)$$

where

T_b = Temperature of the background = 250°K

ΔT_o = Observed temperature difference

ΔT_c = True temperature difference of the central area

D = Central area diameter, and

R = Resolution = 22.5 km

Equation (A.1) was used to compute the dimunition of ir strength with crater size shown as the solid lines in Fig. 6b.

The term D in Eq. (A.1) is the central area diameter and does not have to equal the crater diameter. Instead, it may include a substantial part of a broader ejecta deposit. Thus, the problem here is now to constrain this diameter D based upon observed temperature differences. Solution of Eq. (A.1) for the true temperature difference of the central area (ΔT_c) yields

$$(T_b + \Delta T_c)^4 = T_b^4 - (R^2/D^2)[(T_b + \Delta T_o)^4 - T_b^4]. \quad (A.2)$$

The infrared data shown in Fig. 6b indicates that ΔT_o, the observed temperature differences for many craters, range from 10 to 50°K. In Fig. A.1, central area temperatures are shown as a function of observed temperatures and central area size. Note that these predicted central area temperatures increase sharply for the smaller central area sizes.

Observations of large craters where the central area is resolved show no temperature differences larger than 55°K. These larger craters are older and the infrared enhancement may have weakened from our original, higher value. Here, we will arbitrarily assume that the central areas cannot have temperatures greater than 350°K (only 50°K colder than the preeclipse background). The data shown in Fig. A.1 indicate that the central infrared bright areas must be 5 km in diameter or larger if the observed temperature differences is greater than 10°K and if the central temperature differences do not exceed 100°K. If the observed temperature differences are near 50°K, then the central area must be 16 km or greater.

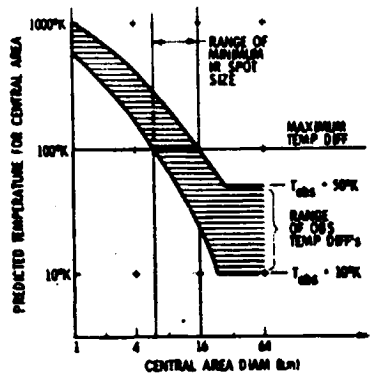

FIG. A.1 Predicted temperatures for circular central areas with diameters between 1 and 64 km and observed temperature enhancements of 10 to 50°K. If these central areas have maximum temperatures of 100°K, then central area sizes must be 6 to 16 km or greater. This indicates agreement between the infrared sizes and strengths plotted in Figs. 5 and 6.

This assumed a simple case where the infrared bright area is confined to a central area. It is more likely that the bright areas gradually fade out for ejecta areas further from the crater. However, the simple model does illustrate that it is likely that the craters with observed temperatures of 10°K or more greater than their environs have central enhanced areas with sizes determined from the contour plots of the infrared data (Fig. 5b).

These arguments which were just applied to the Earth-based infrared data can be applied to the 70-cm radar data as well. For the 70-cm data there are few craters with enhancements greater than that predicted, assuming that the enhanced region is confined to the crater itself. However, there are enough exceptions to this that the

minimum sizes should be computed for this wavelength also.

For the 70-cm radar case we assume that the radar enhancement arises from a central circular area embedded in a square resolution element. Here,

$$\beta_{obs} = 1 + [(\alpha_c - 1)(\pi/4)(D^2/R^2)]. \quad (A.3)$$

where

β_{obs} = observed enhancement
α_c = the enhancement of the central area
D = central area diameter
R = resolution = 7.5 km

Equation (A.3) was used to compute the dimunition of radar intensities for resolution effects shown as the solid lines in Figs. 6a and c.

Once again, the diameter D is for the radar bright area which may be larger than the crater. The enhancement for the central area, α_c, is given by

$$\alpha_c = 1 + [(\beta_{obs} - 1)(4/\pi)(R^2/D^2)]. \quad (A.4)$$

The observed 70-cm radar enhancements vary between two and eight times, yielding the predicted enhancements shown in Fig. A.2. Once again the predicted enhancements have a strong dependence upon central area diameter.

The curves plotted in Fig. A.2 in turn yield estimates of central area sizes. Here we assume that central area enhancements cannot exceed 32, a reasonable value based on observations of larger, resolved craters. Note that Fig. 6c shows 6 craters with diameters between 0.7 and 2.0 km which have observed enhancements of 2.0 times the background. The 70-cm radar bright areas associated with these craters must come from areas at least 1.5 km in diameter based upon the curves in Fig. A.2 associated with the observed enhancement of 2. Similarly, Fig. 6c shows about 10 craters with diameters between 2 and 4 km and observed enhancements between 4 and 8 times the background. The 70-cm radar bright areas associated with these 10 craters must be 3.0 km and greater based upon the curves for the observed enhancements of 4 to 8 in Fig. A.2.

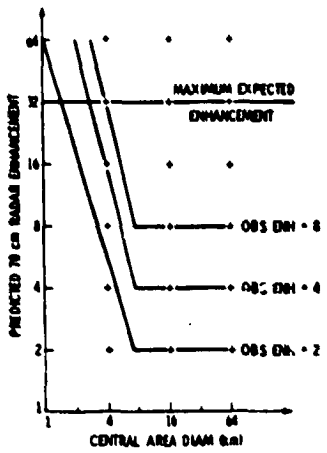

FIG. A.2. Predicted 70-cm enhancements for central areas between 1 and 64 km, observed enhancements of 2, 4, and 8 and a resolution of 7.5 km. Note that minimum central areas must be 1.7 to 4.0 km or larger for an assumed maximum central area enhancement of 32. This is consistent with the 70-cm radar sizes and strengths plotted in Figs. 5 and 6.

Thus, the 70-cm strength values are consistent with a simple, first-order model where the high-reflectivity areas are confined to the crater interior and its near-rim region. This is, of course, one extreme in a spectrum of models. At the other extreme, one permits high-reflecting areas to be as large as those plotted in Fig. 5c, where about 10 craters with diameters between 2 and 4 km have measured 70-cm halos on the order of 15 km. These are somewhat larger than that observed with the Apollo infrared scanner.

In summary, it appears that the peak signal strength coupled with a simple first-order model yields consistent results between observed peak signal strengths and halo diameters. The smaller craters which are 10 to 50°K warmer than environs have infrared halos which are a few tens of kilometers in size. On the other hand, the smaller craters probably have 70-cm radar enhancements which are confined to the crater interior and nearby areas.

019

APPENDIX B

Interpretation of the Infrared and Radar Signatures of Crater Ejecta in Terms of Surface Rocks

In Section IV of this report, the possible identification of surface conditions associated with the 3.8-cm radar bright halos are presented. In this appendix one of these possible identifications is examined in detail. This is based primarily upon the hypothesis developed by Thompson *et al.* (1974, 1980). Thompson *et al.* (1980) discussed how the infrared and radar signatures of lunar craters evolve with time in response to lunar surface processes such as meteoroidic bombardment. In addition, Thompson *et al.* (1974) described how the infrared and radar signatures can be related to surface and subsurface rock distributions. A question here is whether the infrared and radar signatures of radar bright ejecta have an analogous evolution.

A background for this discussion is provided by the relations of the infrared and radar signatures to subsurface and surface rock distributions originally proposed by Thompson *et al.* (1974). Briefly, infrared and radar signatures are characterized as either bright (stronger than nearby areas) or faint (equal to nearby areas). Bright radar signatures imply enhanced populations of surface and/or subsurface rocks with sizes between 0.25 and 10 radar wavelengths, buried no deeper than 50 radar wavelengths. Similarly, bright infrared signatures imply enhanced populations of surface rocks greater than 10 cm in size. This, for the most part, ignores 3.8-cm radar brightness roughness at the space–regolith interface.

Various combinations of these infrared and radar signatures in turn imply various types of surface and subsurface rock populations in the ejecta. The ejecta are 3.8-cm radar bright by definition. However, the data in Fig. 5 suggest that the ejecta have little or no 70-cm radar enhancements. This implies that centimeter-sized rocks occur more frequently in and on the ejecta, while meter-sized rock populations are not enhanced relative to nearby areas. Infrared signatures permit one to assign the excess centimeter-sized rocks to the surface or subsurface. A bright infrared signal from the ejecta implies excess surface rocks while a faint infrared signature with a bright 3.8-cm radar signature implies excess centimeter-sized rocks within the first 2 m of the subsurface. In contrast, the strength data in Fig. 6 are consistent with a model where the crater interior and outer wall are bright at all three wavelengths, implying that these areas have excess surface rocks of centimeter and meter sizes.

The infrared and radar signatures of crater interiors evolve with time such that the younger craters have both infrared and radar enhancements while older craters are only radar bright (Thompson *et al.*, 1980). Perhaps crater ejecta evolves in a similar manner. A model of crater evolution based on these considerations is shown in Fig. B.1. The youngest features would have a large infrared and 3.8-cm radar halos emanating from large ejecta fields of surface centimeter-sized rubble. A feature with an intermediate age would retain a large 3.8-cm radar halo emanating from buried centimeter-sized rubble accompanied by a small infrared halo confined to crater interior. The evolution from the youngest to the intermediate age assumes that surface centimeter-sized rubble will be catastrophically ruptured by meteoroidic bombardment while buried centimeter-sized rubble will be protected (see Hörz *et al.*, 1975; Thompson *et al.*, 1974, 1980). The evolution from intermediate age to the oldest of these features is characterized by a loss of the 3.8-cm radar halo. The craters of our model retain an infrared and radar bright interior, whose evolution to even older forms is described by Thompson *et al.* (1980).

This model for the evolution of radar bright halos is consistent with the data, particularly the range of infrared signa-

020

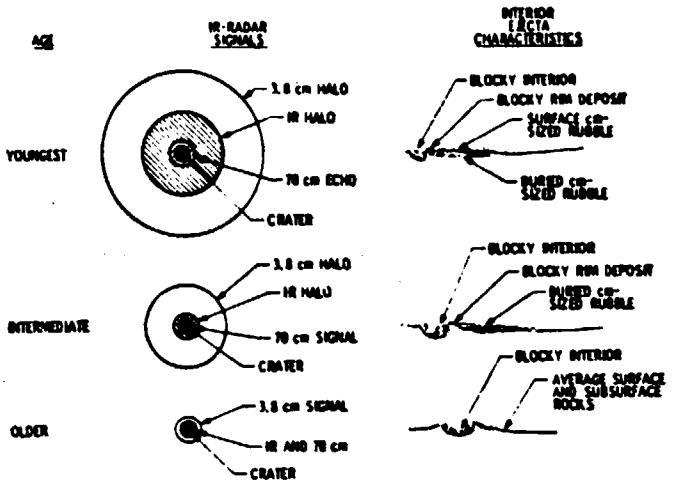

FIG. B.1. A possible model of crater ejecta evolution assuming infrared and radar signals arise solely from surface and subsurface rocks. Only the youngest and intermediate age craters of this model are in the 120-crater catalog described in the main body of this paper. Evolution of the older age crater to still older forms is described by Thompson *et al.* (1980).

tures. Our catalog of 120 covers only the youngest and intermediate features [the older craters with infrared and radar bright interiors and their distributions on the lunar surface are discussed by Thompson *et al.* (1980)]. We selected some 38 candidates for the youngest features based upon their infrared halo size and infrared strength relative to other craters with the same sizes. (Craters with diameters greater than 8 km were arbitrarily dismissed since all of these larger craters had similar 3.8-cm, 70-cm, and infrared characteristics.) These craters are given in Table B.I and their size–frequency distribution is shown in Fig. 8a.

All of our candidates for the youngest craters in this evolution model have large infrared strength and halo diameters. The infrared strengths are well above that expected if the infrared signal were confined to the crater interior. In general, the infrared halos for these craters are about one-half the size of the 3.8-cm halo. The furthest portions of the ejecta are only 3.8 cm radar bright. In addition, some of these candidates for the youngest craters have relatively strong 70-cm signals and halo sizes which would be expected for the youngest craters of any size.

The crater statistics of these candidates for the youngest lunar craters are compared with the overall statistics of craters with radar bright ejecta in Fig. 7. For smaller craters with diameters between 1 and 4 km only the youngest craters have 3.8-cm radar haloes with diameters of 20 km or more. Older craters in this size range probably have smaller 3.8-cm haloes which were arbitrarily dismissed by our selection criterion. On the other hand, craters with diameters between 4 and 8 km show a range of behaviors between the youngest and middle-aged members of the proposed evolution shown in Fig. B.1.

This model of crater evolution depends solely upon the association of infrared and radar signatures with surface and subsurface rocks given in Table B.I. An alternative explanation for high radar echoes invokes surface roughness at the space–regolith interface. Both cavities or mounds at this interface with centimeter scale would create radar backscatter com-

021

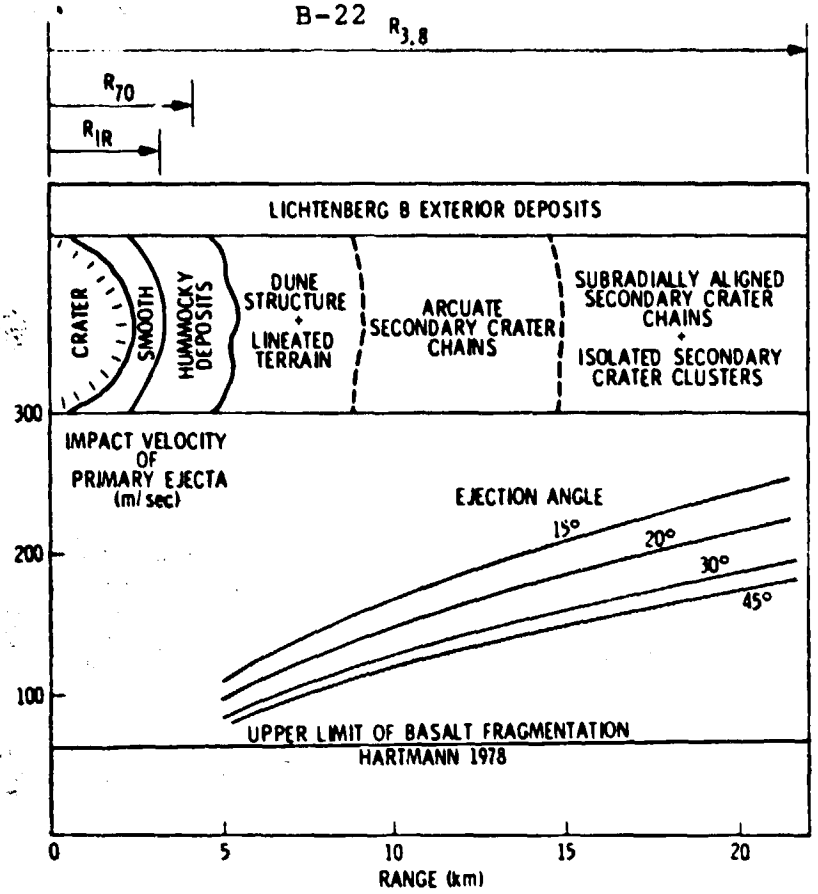

FIG. B.2. Extent of the Earth-based infrared and radar signals from Lichtenberg B, a 0.5-AE-old crater described by Settle *et al.* (1979). This represents an intermediate in the evolution model shown in Fig. B.1 since the 3.8-cm radar echo extends well beyond the crater rim while the infrared and 70-cm radar bright areas are confined to the crater interior and the closed in ejecta deposits.

parable to that of rocks of the same sizes. It is possible that some of the high radar echoes associated with the ejecta may be coming from this type of surface structure as described in Section IV of this paper.

An example of an intermediate-age feature is Lichtenberg B shown in Fig. B.2. The 3.8-cm radar halo has a diameter of 40 km and extends to the furthest surface features associated with ejecta emplacement. However, the infrared and 70-cm radar halo are 8 and 10 km, respectively, and extend no further than the raised rim of the crater. If this evolution model is correct, then Lichtenberg B originally had an infrared halo which was a few tens of kilometers in diameter and encompassed all of the surface expressions of the ejecta emplacement. This would have emanated surface rocks with centimeter sizes. These surface rocks were exposed to meteoritic bombardment and were catastrophically ruptured (Hörz *et al.*, 1975) leaving smaller fragments which do not create enhancements during an eclipse. Today, this crater has a large 3.8-cm halo presumably arising from excess centimeter-sized rocks buried in the ejecta. Also, the infrared and 70-cm radar enhancements are confined to the crater and near-rim deposits, indicating that these areas have excess numbers of surface meter-sized blocks.

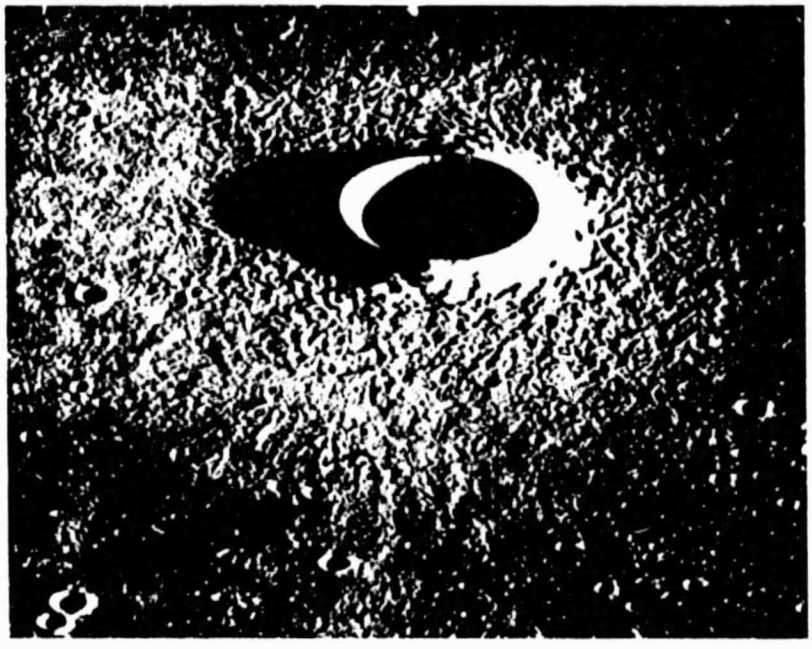

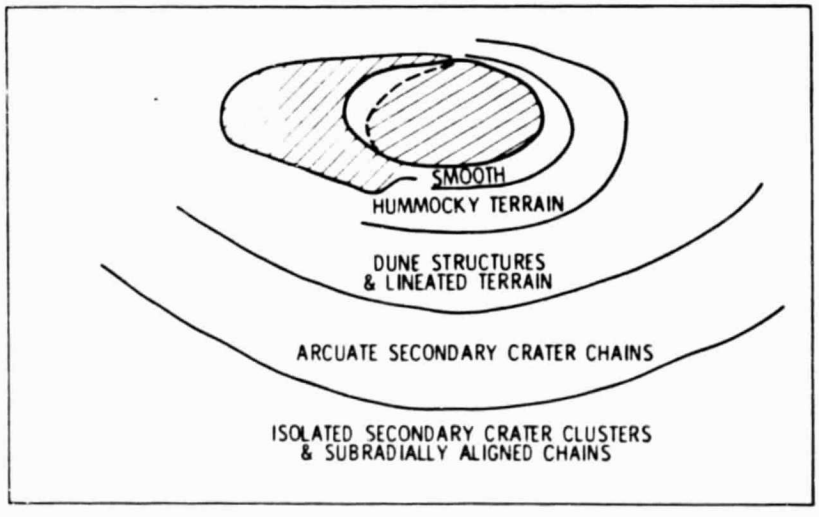

FIG. B.2[9]—*Continued.*

TABLE B.I

SMALL CRATERS WITH STRONG INFRARED SIGNATURES

Name	Long.	Lat.	Diam.	Back.	$D_{3.8\ cm}$	D_{ir}	ΔT_{obs}
"Tiny Tim"	−50.4	−0.2	0.7	M	40	23	28
Near Suess	−47.9	3.9	0.9	M	33	16	46
Near Copernicus C	−14.8	8.2	1.1	M	24	19	21
Near Kies C	−26.0	−25.7	1.1	T	20	20	14
Near Goodacre P	17.3	−33.7	1.2	T	20	12	20
In Mare Vaporum	3.6	14.9	1.2	M	20	11	20
Between Detisle and Diophantus	−34.2	28.4	1.2	M	22	13	32
Floor of Mee	−33.6	−43.6	1.3	T	40	26	35
Near Fra Mauro B	−20.4	− 3.7	1.3	M	22	15	18
Near Wilhelm	−25.6	−42.7	1.3	T	20	16	18
Werner D	3.2	−27.2	1.5	T	20	14	18
Lassel D	−10.5	−14.5	1.7	M	31	14	24
North of S. Gallus[a]	11.3	20.4	1.8	M	31	18	47
Near La Croix F	−60.3	−40.5	2.0	T	30	24	56
Linne[a]	11.7	27.7	2.1	M	40	13	28
Between Capella C and Capella CA	36.0	− 6.0	2.2	T	32	20	16
Near Atlas A	50.1	46.5	2.4	T	30	18	28
Near Grimaldi G	−64.6	− 8.0	2.4	T	45	30	20
Posidonius γ	27.9	30.0	3.0	M	30	49	22
Near Fontenelle G	−18.6	60.4	3.0	M	31	29	36
Abulfeda Q	12.3	−12.8	3.2	T	45	24	20
Herigonius K	−36.4	−12.8	3.2	M	30	17	32
Hesiodus E	−15.3	−27.8	3.3	M	29	15	24
Flamsteed HA	−52.1	− 5.6	3.4	M	36	32	33
Liebig FA	−45.0	−24.8	3.4	M	30	32	38
Encke X	−40.2	0.9	3.5	M	42	18	32
Censorinus	32.7	− 0.4	3.8	T	50	26	45
La Condamine S	−25.0	57.2	3.9	M	55	28	40
Regionoontanus CA	− 5.0	−29.1	4.4	T	80	21	46
Hell QA	− 4.4	−33.9	4.4	T	90	43	44
Piton B[b]	− 0.1	39.3	4.9	M	66	14	28
Floor of Maginus	− 3.7	49.3	5.1	T	95	25	30
Rim of Rocca A	−69.0	−13.8	6.0	T	38	39	24
Möltke	24.2	− 0.6	6.5	M	45	19	28
Rümker E	−56.9	38.5	6.7	M	64	27	32
Louville D	−51.9	46.8	6.7	M	45	23	30
Bush B	17.0	−37.9	6.8	T	52	16	45
Elmmart A	65.4	24.1	7.1	T	90	37	40

[a] See Fig. 2.
[b] See Fig. 1.

ACKNOWLEDGMENTS

Crater population data for the lunar maria was provided to us by W. K. Hartmann who also guided us on suitable lunar crater data sets. We are also indebted to Mr. Steven Schlipf, Pasadena City College, for his careful reviews of our data, and to Mr. Blake Lewis of the Planetary Science Institute for the computer software which produced many of the figures in this report. This study made ample use of photographic displays of the infrared and radar data originally produced at IPL (Image Processing Laboratory) at the Jet Propulsion Laboratory, Pasadena, California, by Apollo Experiment S-217. This study also made use of the infrared/radar crater catalog originally compiled by T. W. Thompson and W. J. Roberts of the Planetary Science Institute.

024

A portion of the research for this paper was done while two of us (R. W. Shorthill and T. W. Thompson) were Visiting Scientists at the Lunar and Planetary Institute, which is operated by Universities Space Research Association under Contract NSR-09-051-001 with the National Aeronautics and Space Administration. Two of us (T. W. Thompson and J. A. Cutts) were funded in part by NASA Grant NASW 3383.

This paper is Lunar and Planetary Institute Contribution 426 and Planetary Science Institute Contribution 144.

REFERENCES

ARTHUR, D. W. G., AGNIERAY, A. P., HORVATH, R. A. WOOD, C. A., AND CHAPMAN, C. R. (1963). The system of lunar craters, quadrant I. *Commun. Lunar Planet. Lab.*, Contrib. 30.

ARTHUR, D. W. G., AGNIERAY, A. P., HORVATH, R. A., WOOD, C. A., AND CHAPMAN, C. R. (1964). The system of lunar craters, quadrant II. *Commun. Lunar Planet. Lab.*, Contrib. 40.

ARTHUR, D. W. G., AGNIERAY, A. P., PELLICORI, R. H., WOOD, C. A., AND WELLER, T. (1965). The system of lunar craters, quadrant III. *Commun. Lunar Planet. Lab.*, Contrib. 50.

ARTHUR, D. W. G., PELLICORI, R. H., AND WOOD, C. A. (1966). The system of lunar craters, quadrant IV. *Commun. Lunar Planet. Lab.*, Contrib. 70.

BOWKER, D. E., AND HUGHES, J. K. (1971). *Lunar Orbiter Photographic Atlas of the Moon* (NASA SP-206). U.S. Govt. Printing Office, Washington, D.C.

Crater Analysis Techniques Working Group (1979). Standard techniques for presentation and analysis of crater size-frequency data. *Icarus* 37, 467–474.

GAULT, D. E., HÖRZ, F., BROWNLEE, D. E., AND HARTUNG, J. B. (1974). Mixing of the lunar regolith. *Proc. Lunar Sci. Conf.* 5th, 2365–2385.

GUINNESS, E. A., AND ARVIDSON, R. E. (1977). On the constancy of the lunar cratering flux over the past 3.3 × 109 yrs. *Proc. Lunar Sci. Conf.* 8th.

HÖRZ, F., SCHNEIDER, E., GAULT, D. E., HARTUNG, J. B., AND BROWNLEE, D. E. (1975). Catastrophic rupture of lunar rocks: A Monte Carlo simulation. *Moon* 13, 235–258.

KUIPER, G. P., WHITAKER, E. A., STROM, R. G., FOUNTAIN, J. W., AND LARSON, S. M. (1967). *Consolidated Lunar Atlas*. Lunar and Planetary Laboratory, University of Arizona, Tucson.

Lincoln Laboratory (1968). *Radar Studies of the Moon*, Final Report, Vol. 2. MIT, Lexington, Mass.

MENDELL, W. W., AND LOW, F. J. (1975). Infrared orbital mapping of lunar features. *Proc. Lunar Sci. Conf.* 6th, 2711–2719.

MOORE, H. J., AND ZISK, S. H. (1973). Calibration of radar data from Apollo 17 and other mission data. *Apollo 17 Preliminary Science Report* (NASA SP-300), pp. 10–17.

Planetary Basaltic Volcanism Working Group (1980). Chronology of planetary volcanism by comparative studies of planetary cratering. *Basaltic Volcanism Study Project* (draft).

SCHULTZ, P. H. (1976). *Moon Morphology*. Univ. of Texas Press, Austin/London.

SCHULTZ, P. H., AND MENDELL, W. (1978). Orbital infrared observations of lunar craters and possible implications for impact ejecta emplacement. *Proc. Lunar Sci. Conf.* 9th, 2857–2883.

SCHULTZ, P. H., GAULT, D. E., AND MENDELHALL, M. (1980). Multiple-body impacts: implications for secondary impact processes. In *Abstracts, XI Lunar and Planetary Science Conference*, XI, 1006–1008.

SETTLE, M., CINTALA, M. J., AND HEAD, J. W. (1979). Emplacement of Fahrenheit crater ejecta at the Luna-24 site. *Moon & Planets* 20, 281–300.

SHOEMAKER, E. M. (1977). Astronomically observable crater-forming projectiles. In *Impact and Explosion Cratering* (D. J. Roddy, R. O. Pepin, and R. B. Merrill, Eds.), pp. 617–628. Pergamon, New York.

SHORTHILL, R. W. (1973). Infrared atlas charts of the eclipsed moon. *Moon* 7, 22–45.

SÖDERBLOM, L. A. (1970). A model for small-impact erosion applied to the lunar surface. *J. Geophys. Res.* 75, 2655–2661.

THOMPSON, T. W. (1974). Atlas for lunar radar maps at 70cm wavelength. *Moon* 10, 51–85.

THOMPSON, T. W., AND ZISK, S. H. (1972). Radar mapping of lunar surface roughness. In *Thermal Characteristics of the Moon* (J. W. Luncas, Ed.), pp. 83–117. MIT Press, Cambridge, Mass./London.

THOMPSON, T. W., MASURSKY, H., SHORTHILL, R. W., TYLER, G. L., AND ZISK, S. H. (1974). A comparison of infrared radar and geologic mapping of lunar craters. *Moon* 10, 87–117.

THOMPSON, T. W., CUTTS, J. A., SHORTHILL, R. W., AND ZISK, S. H. (1980). Infrared and radar signatures of lunar craters: Implications about crater evolution. *Proc. Lunar Highlands Crust Conf.*, 175–177.

WETHERILL, G. W. (1979a). Steady state populations of Apollo-Amor objects. *Icarus* 37, 96–112.

WETHERILL, G. W. (1979b). Apollo objects. *Sci. Amer.* 240, 54–65.

ZISK, S. H., PETTENGILL, G. H., AND CATUNA, G. W. (1974). High-resolution radar maps of the lunar surface at 3.8cm wavelength. *Moon* 10, 17–50.

ZISK, S. H., HODGES, C. A., MOORE, H. J., SHORTHILL, R. W., THOMPSON, T. W., WHITAKER, E. A., AND WILHELMS, D. E. (1977). The Aristarchus-Harbinger region of the moon: Surface geology and history from recent remote-sensing observation. *Moon* 17, 59–99.

025

APPENDIX C

LUNAR CRATER CATALOGS ON SAI'S DEC-10 COMPUTER

Study of the infrared and radar behaviors of lunar craters is facilitated by computerized crater catalogs on SAI's DEC-10 computer in La Jolla. These catalogs can be querried via a telephone modem located in our Pasadena office.

There are two crater catalogs - one catalog of 120 craters was generated via the LPI Visiting Scientist Study. This catalog was carefully checked against the original data sets before it was committed to a computer disk data set. The other catalog of 1310 craters was originally generated as a computer deck via the Megaregolith Study. This catalog was improved by adding a basin index describing whether mare craters were in a basin or in an irregular mare (i.e. in deep or thin mare). Also, the Lunar Orbiter IV photographs for these 1310 craters were computed in order to provide rapid searches for photographs of these craters.

Both catalogs have a common goal of having selenographic, radar-infrared and photogeological descriptors for the lunar craters, as shown in Table C-1. These descriptors can be divided into three classes: (1) general selenographic information, (2) IR and radar characteristics, and (3) photogeologic indices. Each of these classes are described below.

The general selenographic information for a lunar crater includes LPL catalog number, name, position and diameter. Position is given in either latitude and longitude or the direction-cosines Xs, Ys, Zs (XS = sin (lon) cos (lat), Ys = sin (lat), Zs = cos (lon) cos (lat)). These direction cosines are useful for deriving a number of supplementary items. For example, angle of incidence for earth-based observations is approximately arccos (Zs).

The IR and radar signatures of lunar craters provides a second class of information. The most important data is the IR and radar strengths for the crater interiors. In addition to strengths, other IR/radar specific data includes ZAC (3.8cm radar) map numbers, LAC (70cm) map numbers and angle of incidence.

Various photogeological indices provides a third class of information. These include ages derived either from the LPL catalog or the USGS maps, as well as various information about photography (either Apollo, Lunar Orbiter or full-moon plates from the Consolidated Lunar Atlas).

Specific implementations of these general goals is given in Tables C-2 and Table C-3. The lunar basin index in the 1310 crater catalog was computed using the parameters shown in Table C-4.

TABLE C-1: OVERVIEW OF LUNAR IR/RADAR CRATER DATA BASES

I. General Selenographic Information

LPL Number

Crater Name

Crater Position (latitude and longitude)

Cration Position (direction cosines, Xs, Ys, Zs)

II. IR/Radar Data

Strengths (IR, 3.8cm, 70cm)

Sizes (IR, 3.8cm, 70cm)

Map Information (LAC number, ZAC number)

Bright Ejecta Index = Fuzzy Index

Angle of Incidence

IR Resolution

III. Photogeologic Indices

Ages (LPL and USGS)

Background = Mare/Terra Index

= Basin Index

LPL Class

Full-Moon Appearance

Fractured-Floor Index

Depth-to-Diameter Ratio

Detailed Study Index

LO IV Photo Information (plate/position)

Apollo Photo Index

Consolidated Lunar Atlas Information (for full-moon photos)

TABLE C-2: FORMAT FOR FCAT. DATA

LINE	VARIABLE	FORMAT	DESCRIPTION
1	LPLN	I6	LPL catalog number
	CNAME(16)	3X,30A1	Crater name
	DLON	3X,F6.2	Longitude (In DEG.)
	DLAT	F6.2	Latitude (In DEG.)
	DIAM	F6.2	Diameter (In KMS)
	XS	F6.3	Dir. cosine XS=cos(β) sin(λ)
	YS	F6.3	Dir. cosine YS=sin(β)
	ZS	F6.3	Dir. cosine ZS=cos(β) cos(λ)
2	LPLN	I6	LPL number
	IDIR	I6	IR Diam. (kms)
	ID38	I6	3.8cm Diam. (kms)
	ID70	I6	70cm Diam. (kms)
	ISIR	I6	IR strength
	IS38	I6	3.8cm strength
	IS70	I6	70cm strength
	HSTAR	1X, 4S	IR bright index
	LACN	I6	LAC chart number
	NUMZAC	I6	Number of ZAC charts
	ZACN(4)	4F6.2	ZAC chart numbers
3	LPLN	I6	LPL number
	NUMLO4	I6	Number of Lunar Orbiter-IV prints
	LO4PP(20)	5(I4,1HH, I1, I4, A1, I2, 5X)	Lunar Orbiter-IV photo info LO4PP(1,6,etc.)=Frame # LO4PP(2,7,etc.)=1,2, or 3 LO4PP(3,8,etc.)=Atlas Page # LO4PP(4,9,etc.)=A→ M | Location LO4PP(5,10,etc.)=1→ 16 | Index

TABLE C-2 (Cont'd)

LINE	VARIABLE	FORMAT	DESCRIPTION
4	LPLN	I6	LPL number
	LAGE	I6	LPL catalog age
	LCLASS	A6	LPL catalog description
	HBACK	A6	Crater background (' mare' or 'terra')
	HMT	A6	Mare/Terra Index (M or T)
	NMAP	I6	Number of Apollo missions
	MAP(3)	3I6	Apollo missions
	IDFM		Size in full moon
	IDLO4		Lunar Orbiter-IV ray size
5	LPLN	I6	LPL number
	IOUT	I6	Catalog entry numbers
	COM(30)	3X,30A1	Comments
	NUMCAT	3X, I6	Number of consolidated Lunar Atlas plates
	IPCAP(8)	4(3X,A1,I2)	Consolidataed Lunar Atlas Plate numbers IPCAP(1,3,etc.)=A thru H IPCAP(2,4,etc.)=1 thru 6

Notes: (1) Formats are Modulo-6

(2) FCAT. DAT has 120 entries

TABLE C-3: PIRC3.TWT FORMAT

LINE	VARIABLE	FORMAT	DESCRIPTION
1	LPLN	I6	LPL Number (NUMERIC)
	LPLA	A1	LPL Number (ALPHA)
	CNAME(16)	1X,16A1	Crater Name
	DLON	F6.1	Crater Longitude (DEG.)
	DLAT	F6.1	Crater Latitude (DEG.)
	DIAM	F6.2	Crater Diameter (KMS)
	XS	F6.3	Dir. cosine XS = cos(β)sin(λ)
	YS	F6.3	Dir. cosine YS = sin(β)
	ZS	F6.3	Dir. cosine ZS = cos(β)cos(λ)
	ICC	I6	Catalog Entry Number
2	LPLN	I6	LPL Number
	INIR	I6	IR Strength Index
	IN38	I6	3.8cm Radar Strength Index
	IN70	I6	70cm Radar Strength Index
	H1,H2,H3	3X,3A1	IR/Radar Index (FFF→BBB)
	S	F6.2	Normalized Strength
	LACN	I6	LAC Chart Number
	ZACN	F6.2	ZAC Chart Number
	ANGINC	F6.1	Angle of Incidence
	HF	5X,A1	Fuzzy Index (F = FUZZY)

TABLE C-3 (Continued)

LINE	VARIABLE	FORMAT	DESCRIPTION
3	LPLN	I6	LPL Number
	LAGE	I6	LPL Age Class
	HMT	5X,A1	Mare/Terra Index (M or T)
	HBASIN(2)	2A6	Basin Indices
	DDRAT	F6.3	Depth/Diam. Ratio
	FFIND	A6	Fractured Floor Index
	FMIND	A6	Full-Moon Index
	DSIND	A6	Detailed Study Index
4	LPLN	I6	LPL Number
	NLOPIC	I6	Number of Lunar Orbiter IV Photos
	4(PIC ID's)	4(3X,I3, 1HH,I1, 1H,A1,I2)	Frame Number, subframe number (1, 2 or 3) Atlas Page Number Atlas Position Index (A-G) Atlas Position Index (1-12)

NOTES: (1) Most variables have formats MODULO 6.
(2) Variable HF is unreliable (does not correspond to fuzzy catalog).
(3) The following variables are currently undefined:

DDRAT & FFIND &
FMIND & DSIND

(4) Variables HBASIN is either 'TMARE' or 'TERRA' if outside all basins.
(5) PIRC3.TWT has 1310 entries.

TABLE C-4: BASIN CHARACTERISTICS

BASIN	RADIUS (km)	LONG. CENTER	LAT. CENTER	COMPUTER NAME	COMPUTER INDEX
Orientale	195 310	-95 0	-20.0	ORIEN	1
Imbrium	335 485	-19.0	+37.0	IMBRM	2
Crisium	225 335	+59.0	+17.0	CRISM	3
Humorum	210 280	-39.0	-24.0	HUMOR	4
Nectarus	200 300	+34.0	-16.0	NECTR	5
Serenitatis	155 340	+19.0	+26.0	SEREN	6
Fecunditatis	120 120	+51.0	- 3.0	FECUN	7
Tranquillitatis (West)	140 140	27.0	9.0	TWEST	8
Tranquillitatis (East)	120 120	38.0	11.0	TEAST	9
Nubium	180 180	-17.0	-19.0	NUBUM	10